SANDIA REPORT
SAND2000-3124
Unlimited Release
Printed December 2000

Final Report of LDRD Project: An Electromagnetic Imaging System for Environmental Site Reconnaissance

Gary J. Denison, Guillermo M. Loubriel, Malcolm T. Buttram, Larry F. Rinehart, Wesley Helgeson, Darwin Brown, Martin W. O'Malley, Fred J Zutavern, John Aurand, and Larry Carin

Prepared by
Sandia National Laboratories
Albuquerque, New Mexico 87185 and Livermore, California 94550

Sandia is a multiprogram laboratory operated by Sandia Corporation,
a Lockheed Martin Company, for the United States Department of
Energy under Contract DE-AC04-94AL85000.

Sandia National Laboratories

Issued by Sandia National Laboratories, operated for the United States
Department of Energy by Sandia Corporation.

Available to DOE and DOE contractors from
Office of Scientific and Technical Information
P.O. Box 62
Oak Ridge, TN 37831

Prices available from (703) 605-6000
Web site: http://www.ntis.gov/ordering.htm

Available to the public from
National Technical Information Service
U.S. Department of Commerce
5285 Port Royal Rd
Springfield, VA 22161

NTIS price codes
Printed copy: A04
Microfiche copy: A01

SAND2000-3124
Unlimited Release
Printed December 2000

Final Report of LDRD Project:

An Electromagnetic Imaging System for Environmental Site Reconnaissance

Gary J. Denison, Guillermo M. Loubriel, Malcolm T. Buttram, Larry F. Rinehart,
Wesley Helgeson, Darwin Brown, Martin W. O'Malley, and Fred J Zutavern
Directed Energy Special Applications Department
Sandia National Laboratories
P. O. Box 5800
Albuquerque, NM 87185-1153

John Aurand*
Department of Electrical and Computer Engineering
University of New Mexico
Albuquerque, NM

Larry Carin
Department of Electrical and Computer Engineering
Duke University
Durham, NC 27708-0921

Abstract

This report provides a summary of the LDRD project titled: An Electromagnetic Imaging System for Environmental Site Reconnaissance. The major initial challenge of this LDRD was to develop a ground penetrating radar (GPR) whose peak and average radiated power surpassed that of any other in existence. Goals were set to use such a system to detect the following: 1) disrupted soil layers where there is potential for buried waste, 2) buried objects such as 55-gallon drums at depths up to 3 m, and 3) detecting contaminated soil.

Initial modeling of the problem suggested that for soil conditions similar to Puerto Rican clay loam, moisture content 10 percent (conductivity = 0.01 mhos at 350 MHz), a buried 55-gallon drum could be detected in a straightforward manner by an UWB GPR system at a depth of 3 meters. From the simulations, the highest attenuation (-50 dB) was the result of scattering from a 3-m deep vertically orientated drum. A system loss of –100 dB is a typical limit for all kinds of radar systems (either direct time-domain or swept frequency). The modeling work also determined that the waveshape of the pulse scattered off the buried drum would be relatively insensitive to drum orientation, and thus easier to detect with the GPR system.

Two GPR systems were designed around the model, built, and tested in the field during the course of the LDRD. Both systems were characterized, and reflected signals from a 55-gallon drum suspended

---

* Present address: ITT Industries, AES Division, Albuquerque, NM 87110

in air were recorded. Unfortunately, funding was unexpectedly cut in the last year of the project and no measurements could be made on buried targets.

The specific tasks/milestones for FY98, FY99, and FY00 were:

FY98	Planned	Actual
1. Develop model for detection of 55-gallon drums and contaminated soil.	2QFY98	2QFY98
2. Build transmitter system at a fixed center frequency.	2QFY98	2QFY98
3. Design and build a variable center frequency transmitter.	3QFY98	4QFY98
4. Test the transmit/receive system.	4QFY98	1QFY99
FY99 and FY00		
1. Assemble GPR system and conduct outdoor “in air” field test at 6640.	3QFY99	1QFY00
2. Obtain the necessary dig permits to bury target drums.	3QFY99	4QFY99
3. Bury drums and prepare for outdoor tests.	CANCELED	
3. Perform initial outdoor tests looking at buried target drums in Area III.	CANCELED	
4. Perform tests in 6600’s Area III environmental restoration sites.	CANCELED	

This final project document reports on the theory, hardware, and results from the GPR systems developed for this LDRD.

CONTENTS

Section

1. PROJECT OVERVIEW 4

2. MODULATORS 4
  - 2.1 DUAL-RESONANT MODULATOR 4
  - 2.2 BIPOLAR MODULATOR 5

3. SWITCHES AND PULSE FORMING NETWORKS 7
  - 3.1 HIGH GAIN GaAs SWITCHES 7
    - 3.1.1 DEVICE DESCRIPTION 7
    - 3.1.2 HIGH GAIN 9
    - 3.1.3 CURRENT FILAMENTS 9
    - 3.1.4 DEVICE LONGEVITY 10
  - 3.2 LASER DIODE ARRAYS AND ELECTRONICS 11
  - 3.3 PULSE FORMING LINES 12
    - 3.3.1 DOUBLE-SWITCHED LINE 12
    - 3.3.2 FOLDED LINES 13
    - 3.3.3 ROSS CIRCUIT 14
    - 3.3.4 FROZEN WAVE GENERATOR 16

4. ANTENNAS 19
  - 4.1 TRANSMIT ANTENNAS 19
    - 4.1.1 SG ANTENNA 19
    - 4.1.2 DOUBLE RIDGE TEM ANTENNA 21
  - 4.2 RECEIVE ANTENNAS 23

5. GPR SYSTEMS 25
  - 5.1 ROSS CIRCUIT GPR 26
  - 5.2 FROZEN WAVE GENERATOR GPR 29

6. BURIED DRUM TEST 31

7. PROJECT CALCULATIONS 32

8. CONCLUSIONS 32

9. Appendix A: Double-Ridge TEM Antenna Design for High-Power GPR System 33

10. Appendix B: Simulations of GPR Backscatter from Buried Drums 70

1) PROJECT OVERVIEW

The major initial challenge of the LDRD ‘An Electromagnetic Imaging System for Environmental Site Reconnaissance’ was to develop a system whose peak and average radiated power surpasses that of any other ground penetrating radar in existence. The direction taken was to develop an ultra-wideband (UWB) or direct time-domain radar. The advantages of this type of system are many. First, it allows straightforward removal of ground-surface backscattered energy (clutter) and reduces transmit / receive antenna crosstalk by using time-range gating of the receiver system. Thus by selecting the time gate later than the surface return, the desired backscatter from buried targets can be more easily detected. Second, the transmission of a pulse with total duration of, for example, 4-5 ns implies that one can use platforms that are at altitudes as low as 8 feet. This is important since the return power, in the radar equation, goes as range to the target to the *fourth* power. Finally, time-domain implementation results in less expensive and perhaps faster and more efficient systems. This is attractive if the GPR requires operation at heavily contaminated sites or at an accident. The primary disadvantage of the direct time-domain radar approach is *usually* more limited detection range due to lower radiated energy or average power.

Efforts to develop an UWB system were begun in FY97 with the ‘Electromagnetic Impulse Radar for Detection of Underground Structures’ LDRD. A system was designed, built, and tested to: 1) measure penetration of the transmit pulse though concrete blocks, 2) measure returns from targets in air (no penetration), and 3) measure returns from targets obscured by concrete. This system was reported in SAND98-0724. The UWB GPR concept was then enlarged to environmental remediation work, particularly the location of buried drums containing industrial waste products. Theoretical work done by Dr. John Aurand and Dr. Larry Carin indicated the need for a higher center frequency system, around 250-300 MHz. Two such systems were placed in the field in FY99 and FY00. Data was collected on the transmitted pulses, and reflected signals from a drum in air.

The purpose of this document is to report on the work done to develop the UWB GPR concept. The following basic system building blocks will be covered: modulator designs, PCSS and pulse forming networks, antennas, and system theory. Data will be presented on each of the two integrated systems.

2) MODULATORS

Two different modulators were used in this study. A dual-resonant modulator was used initially to charge a variety of pulse forming lines that required a single polarity charge voltage. A second modulator was eventually produced when bipolar charging was required. Section 3 covers the pulse forming lines (double-switched, folded, Phillies, Ross, and Frozen Wave Generator) in detail.

2.1) DUAL-RESONANT MODULATOR

Figure 2.1-1 is a schematic of the modulator used to charge the original double-switch, folded, Phillies, and Ross circuit pulse forming lines.

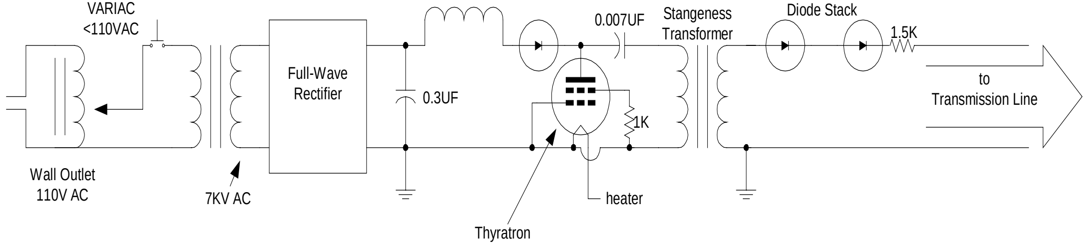

Figure 2.1-1 - Thyratron-based dual-resonant charging modulator.

AC supply voltage applied to the input of the modulator is stepped up, rectified, and in turn charges the 0.3 µF capacitor to V. When the thyratron switch closes, charge flowing from the capacitor through the 4 H inductor creates a magnetic field. The collapse of this field, when the thyratron opens, doubles the voltage across the 0.007 µF capacitor to 2V. Hence the name dual-resonant modulator. The output transformer has a primary to secondary windings ratio of 1:5.

The modulator's output pulse, measured at the secondary of the Stangenes transformer, shown in Figure 2.1-2, has a pulse width of ~1.5 µseconds FWHM. The short pulse width and single polarity voltage increase photoconductive semiconductor switch (PCSS) lifetime, which is a critical system parameter. The charging waveform applied to the switched transmission lines, after the diode stack, is shown in Figure 2.1-3.

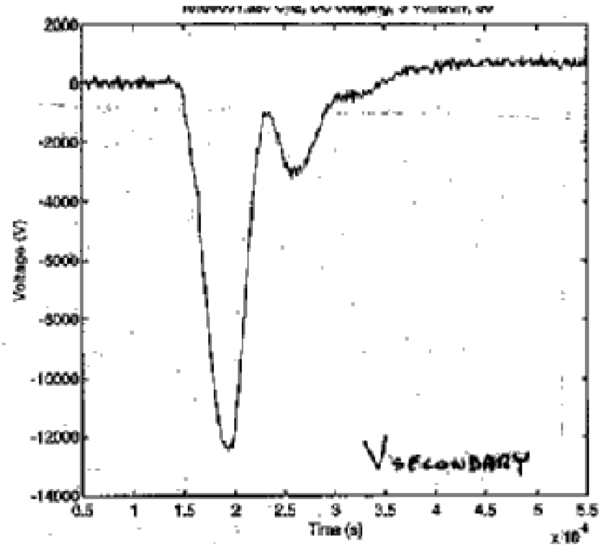

Figure 2.1-2 - Modulator output pulse at the secondary windings of the Stangenes transformer. Peak voltage is -12.5 kV.

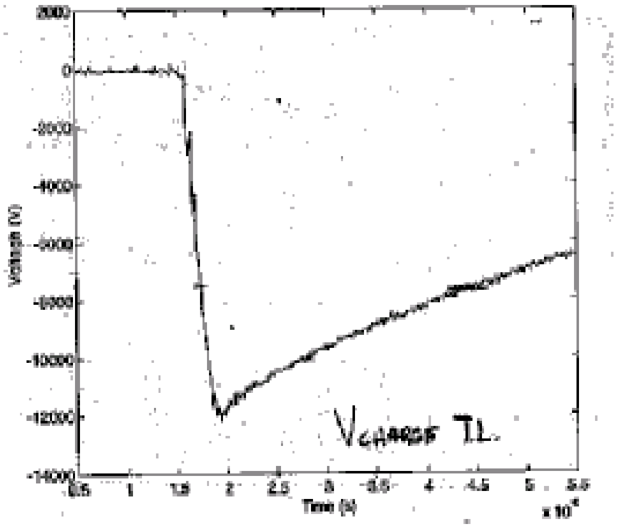

Figure 2.1-3 - Transmission line charging waveform after the diode stack. Peak voltage is 12 kV.

2.2) BIPOLAR MODULATOR

The progression of the pulse forming lines from the 2-switch design to the frozen wave generator (FWG) design required a change in modulators, unipolar to bipolar output. Figure 2.2-1 is the schematic of the bipolar modulator borrowed from another project to charge the FWG. In this design, the primary energy storage capacitor is charged positive. When the thyratron closes, the capacitor discharges through the primary windings of the transformer, inducing both a negative and positive output on the center-tapped secondary winding. The actual hardware is illustrated in Figure 2.2-2.

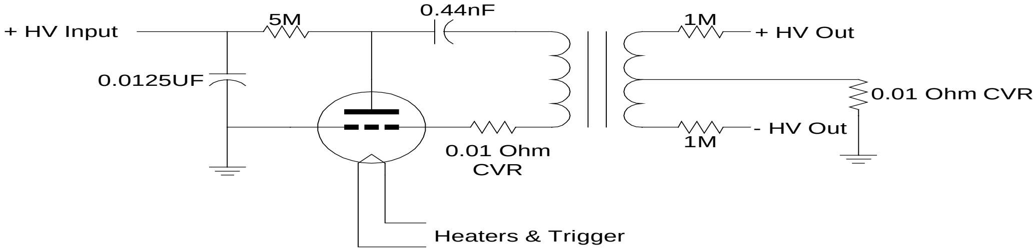

Figure 2.2-1 - Schematic of the bipolar modulator.

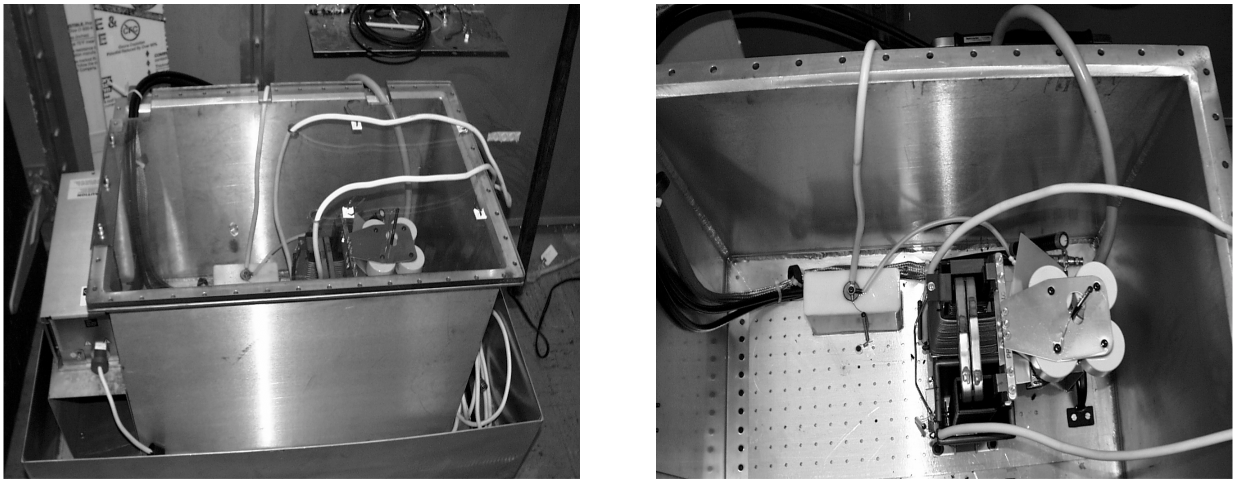

Figure 2.2-2 - Photographs of the bipolar modulator used to charge the frozen wave generator pulse forming line. The dimensions of the tank on the left are 18 in. wide by 18 in. high by 30 in. long.

The output pulse from this system was a factor of 5 shorter, approximately 250–300 ns FWHM, than the dual-resonant charging system; and therefore even more conducive to longer PCSS lifetime. It is also believed that a faster rising, shorter pulse may contribute to lower PCSS jitter. Figure 2.2-3 is an oscilloscope trace of the positive half of the modulator's output.

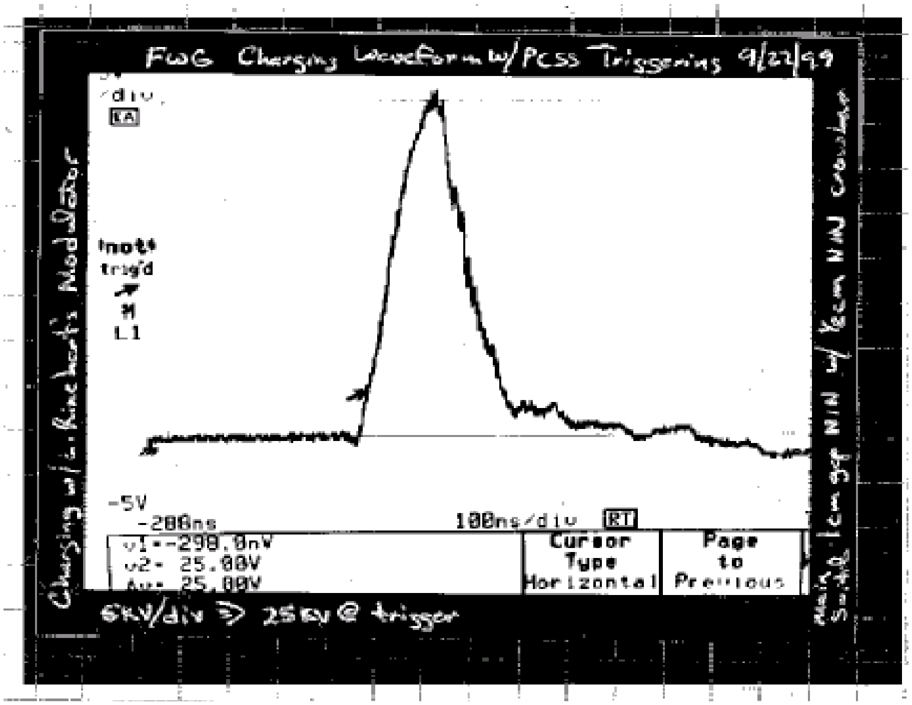

Figure 2.2-3 - Output pulse from the positive half of the bipolar modulator. Peak voltage is +25 kV.

3) SWITCHES AND PULSE FORMING NETWORKS

3.1) HIGH GAIN GaAs SWITCHES

High gain PCSS offer switching improvements in voltage, current, rise time, jitter, optical activation, size, and cost. High voltage operation of conventional (linear) PCSS, is limited by optical trigger energy requirements, which are 1,000 to 100,000 times greater than those for high gain PCSS. To understand and develop high gain PCSS many experiments have been performed (for general references, see reference 1). In order to explain what are PCSS and to describe the state-of-the-art, the following paragraphs provide a brief description of some of these associated properties and issues: (1) general device description, (2) high gain, (3) current filaments, and (4) device longevity.

3.1.1) DEVICE DESCRIPTION

The GaAs switches used in this experiment are lateral switches (see Figure 3.1-1) made from undoped GaAs of high resistivity >10^7 Ω-cm and metallic lands that connect the switch to an energy source and a load. The metallic contacts provide either p or n doped regions. The simplest n contact is the ubiquitous Ni-Ge-Au-Ni-Au metallization. The p contacts are made from Au-Be. The insulating region separating the two contacts (the gap, in analogy to spark gaps) has a length that varies from 0.2 mm to 3.4 cm since higher switched voltages require a larger gap to avoid surface flashover. Because of high electric fields the switches were immersed in a dielectric liquid (Fluorinert). Pulse charging of this configuration is typically required to reduce the surface flashover problem.

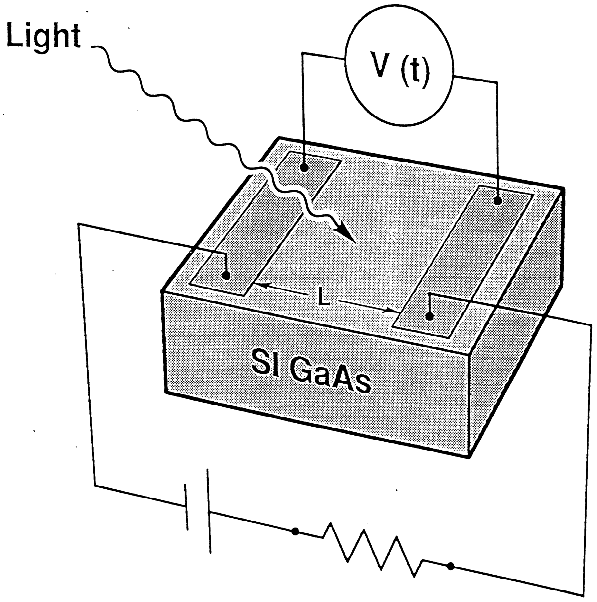

Figure 3.1-1. Schematic of the lateral semi-insulating (SI) GaAs switches used in this study. In this circuit the switch is being used to discharge a capacitor into a resistive load. The switch dimensions depend on the application. The distance between the contacts (the "gap," in analogy to spark gaps) varies from 0.2 mm to 3.4 cm, for example. Switch thickness (the vertical direction) is always 0.6 mm.

For the tests in this report, laser diode arrays were used to trigger the switch/switches (see Figure 3.1-2). Each array consisted of four laser diodes coupled to a 300 μm-diameter fiber optic. Each array delivered about 0.7 μJ in 20 ns at about 870 nm to illuminate the switch. The first GPR system utilized four arrays and fibers per switch. The wavelength of the laser diode arrays ranged from 870 to 880 nm.

Since the SNL discovery of a high gain switching mode in GaAs, these switches have been investigated for use in many high voltage applications such as: impulse and ground penetrating radar, switches for firing sets for weapons, as drivers for laser diode arrays to allow detection of objects through fog and smoke, and high voltage accelerators. PCSS offer improvements over existing pulsed power technology. The most significant are 100 ps risetime, kilohertz (continuous) and megahertz (burst) repetition rates, scalable or stackable to hundreds of kilovolts and tens of kiloamps, optical control and isolation, and solid state reliability. Table I shows the best results obtained with the switches for various applications.

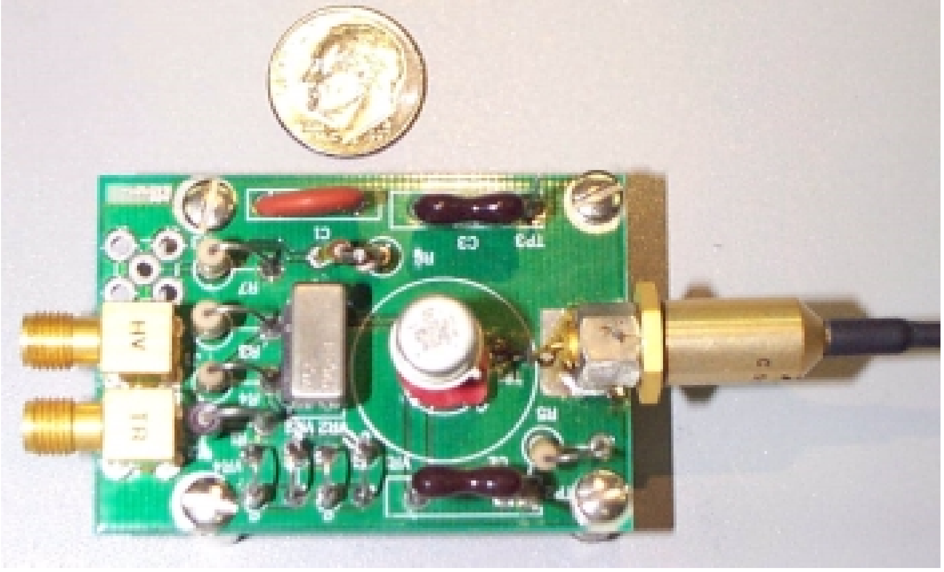

Figure 3.1-2. This close-up photograph shows the laser diode array, its electronics, and the optical fiber through which directs the laser's output onto the PCSS. The laser diode is housed in the cylindrical section at the right. The connection of the optical fiber to the laser diode is barely visible at the right. To give an idea of size a dime is also shown.

Table I **Parameter**	**GaAs, high gain mode, best individual results.**	**GaAs, high gain mode, simultaneous results.**
Switch Voltage (kV)	**220**	**100**
Switch Current (kA)	**7.0**	**1.26**
Peak Power (MW)	**650**	**48**
Rise time (ps)	**350**	**430**
R-M-S jitter (ps)	**50**	**150**
Optical Trigger Energy (nJ)	**2**	**180**
Optical Trigger Gain	**10^5**	**10^5**
Repetition Rate (Hz)	**1,000**	**1,000**
Electric Field (kV/cm)	**100**	**67**
Device Lifetime (# pulses)	**>100 x 10^6**	**5 x 10^4, (at 77 kV)**

Table I. Best switching results for high gain GaAs switches. The results in the middle column are not simultaneous.

In all the applications listed, the switch has been designed as a stand-alone system with a separate laser that triggers the switch. In a separate project we demonstrated that small lasers, capable of being monolithically integrated with the switch, did trigger the switch. This development, coupled with recent advances in switch lifetime/longevity, will allow rapid entry into new applications such as the one discussed here, ground penetrating radar.

3.1.2) HIGH GAIN

Conventional PCSS produce only 1 electron-hole pair per absorbed photon. The energy of the individual photons excites electrons from the valence band to the conduction band. This excitation is independent of the electric field across the switch, and conventional PCSS can be operated to arbitrarily low voltage. High gain PCSS, on the other hand, occurs only at high electric fields (greater than 4 kV/cm). The photo-excited carriers, which are produced by an optical trigger, gain enough energy from the electric field to scatter valence electrons into the conduction band. This process is called impact ionization or avalanche carrier generation. Because many carriers are produced per absorbed photon, switches operating in this mode require extremely low-energy optical trigger pulses, and they are called high gain PCSS in contrast to the conventional PCSS, which are often called linear PCSS. To stand off high voltage, PCSS must be made long enough to avoid avalanche carrier generation with no optical trigger (dark breakdown). The optical trigger energy for a linear PCSS scales with the square of its length. So high voltage linear PCSS can require rather high energy optical trigger pulses (25 mJ for 100 kV switches switched to 1 Ω). It is the high gain feature of GaAs PCSS that allows their triggering with small semiconductor LDA. We have triggered 100 kV gallium arsenide (GaAs) PCSS, with as little as 90 nJ. A GaAs PCSS, operating in a low impedance circuit, can produce 100,000 times as many carriers as a linear PCSS would produce.

With most insulating materials (e.g. plastic, ceramic, or glass) and undoped semiconductors (e.g. silicon, gallium phosphide (GaP), or diamond), bulk avalanche carrier generation does not occur below 200 kV/cm. Semiconductors such as GaAs and indium phosphide (InP) are very different in that high gain PCSS can be initiated at unusually low electric fields (4-6 kV/cm and 15 kV/cm, respectively). Surface breakdown limits the field across PCSS to less than the bulk breakdown field (generally 100 kV/cm). Since PCSS need to absorb light through a surface, optically activated avalanche breakdown is only practical in materials that exhibit high gain at lower fields (lower than the surface breakdown field). A very important part of the research into high gain PCSS has been to develop models for high gain at low fields in these materials.

Once avalanche carrier generation is initiated, it continues until the field across the switch drops below a threshold (4-6 kV/cm depending upon the type of GaAs). Since carrier generation causes the switch resistance to drop, in most circuits, the field across the switch will also drop. Indeed, when we first observed high gain PCSS, the most outstanding feature was that at high fields, when the switches would turn on, their voltage would drop to a constant non-zero value and stay there until the energy in the test circuit was dissipated. We originally called this switching mode “lock-on” to describe this effect. “High gain” has been adopted more recently to help distinguish this type of switching mode from other modes which also exhibit persistent conductivity, such as thermal runaway, and single or double injection. The field dependence for avalanche carrier generation that is exhibited in high gain PCSS is similar to that exhibited by Zener diodes. In series with a current limiting resistor, they will conduct whatever current is necessary to maintain a constant voltage across their contacts. In the case of a high gain PCSS, this voltage/field is the “lock-on” voltage/field or the threshold to low field avalanche carrier generation. The phase of switching during which the switch maintains this constant voltage drop is called the sustaining phase, and testing and modeling this phase is also a critical area of our research.

3.1.3) CURRENT FILAMENTS

Another important feature of high gain PCSS is that the current forms in filaments that are easily observed with a near infrared sensitive camera (most non-intensified, black and white, CCD-based cameras). When the carriers recombine (i.e. conduction electrons drop back into the valence band), infrared photons are emitted at approximately 875 nm (1.4 eV). If the filaments are near the surface of the switch, the emitted photons escape and a camera can detect them. Some images obtained in this manner are shown in Figure 3.1-3. We believe that current filaments are fundamental to high gain PCSS and we have never observed high gain without current filaments. While current filamentation can lead to catastrophic destruction of the PCSS, current amplitude and pulse widths can be limited to allow non-destructive operation. In addition, the optical trigger can be distributed across the switch in a manner that creates multiple or diffuse filaments to extend the lifetime or current carrying capacity of the switch.

3.1.4) DEVICE LONGEVITY

The biggest problem caused by the filaments is the gradual accumulation of damage at the contacts which limits their useful life to 1-10,000,000 shots depending upon the current per filament and the optical trigger distribution. Presently, device lifetime is a limitation of this technology for some applications. Although there is little change in performance, the PCSS degrade in time because the regions near the contacts are damaged on each pulse, and they gradually erode. The bulk semiconducting material shows very little, if any, degradation as the contact regions wear out. The fact that the degradation is confined to regions near the contacts suggests that developing better contacts that allow for higher current density can make substantial increases in switch lifetime. When this project started, high-gain PCSS would last for $\sim 10^4$ pulses under a specific set of test conditions (0.5 MW). During the course of this project, the lifetime has been improved to 100×10^6. In comparison, the semiconductor lasers, which trigger or are driven by these switches, can last from 10^8 to 10^{10} pulses.

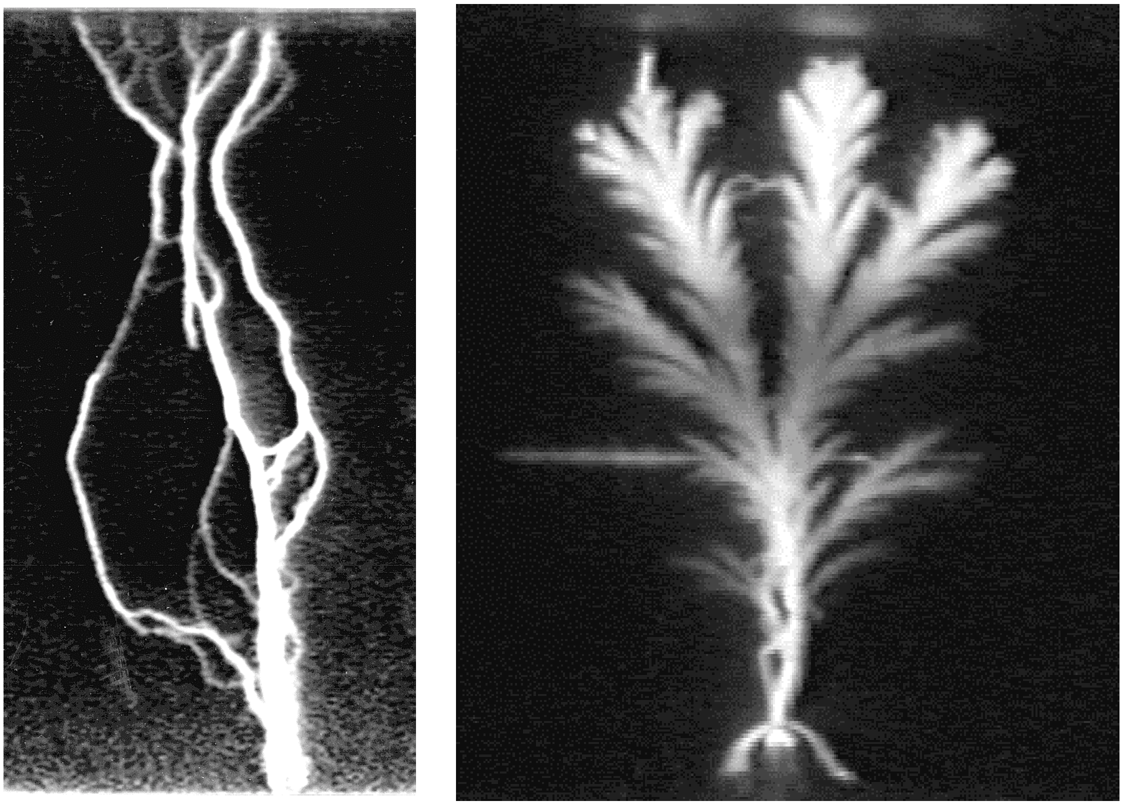

Figure 3.1-3 These photographs show examples of the current filaments which form during high gain PCSS operation. The images are recorded from the infrared (875 nm) radiation that is emitted as the carriers recombine in the switch. In both cases, the switches are 1.5 cm long (vertically). The PCSS on the left was charged to 45 kV and conducted 350 A for 10 ns. The PCSS on the right was charged to 100 kV and conducted 900 A for 1.4 ns.

We are presently fabricating new generations of deep-diffused and epitaxial-grown contacts that should yield further improvements. At higher powers or longer pulses, lifetimes are reduced.

We plan to address these issues and accelerate lifetime testing by shifting our interests to higher current and higher repetition rate testing. References 2a and 2b describe our longevity experiments.

2a A. Mar, G. M. Loubriel, F. J. Zutavern, M. W. O'Malley, W. D. Helgeson, D. J. Brown, H. P. Hjalmarson, A. G. Baca, R. L. Thornton, and R. D. Donaldson, "Doped Contacts for High-Longevity Optically-Activated, High Gain GaAs Photoconductive Semiconductor Switches," in Proceedings of 12th IEEE Pulsed Power Conference, Monterey, CA, June 27-30, 1999, pp. 303-306.

2b A. Mar, G. M. Loubriel, F. J. Zutavern, M. W. O'Malley, W. D. Helgeson, D. J. Brown, H. P. Hjalmarson, A. G. Baca, R. L. Thornton, and R. D. Donaldson,, "Doped Contacts for High-Longevity Optically Activated, High Gain GaAs Photoconductive Semiconductor Switches," in Proceedings of the 24th International Power Modulator Symposium, Norfolk, Va., June 26-29, 2000, pp. 69-72.

The longevity tests have demonstrated that there is less contact degradation with short duration currents. In our longevity test-bed we utilize a pulse charger that charges a transmission line to high voltage with a risetime of about 1 µs and a total pulse width of a few microseconds. If we discharge this transmission line when the charger is at full voltage, the switches will carry a current of 10 to 50 A for the length of the transmission line (3 to 30 ns, typically) and a much smaller current for a few microseconds. This long duration "recharge current" greatly reduces device life when compared to the case when the current only lasts for tens of nanoseconds. We determined this by adding isolation diodes between the pulse charger and the transmission line. When the line was charged, the isolation diodes would hold the line at high voltage. We would trigger the switches well after the pulse charger finished, thus discharging only the transmission line. These isolation diodes were also used in this LDRD.

3.2) <u>LASER DIODE ARRAYS AND ELECTRONICS</u>

In this LDRD we used small laser diode arrays to trigger the switches. These were purchased from Laser Diode Inc. (Model CVD-167F) and consisted of an array of four or more laser diodes that are hard coupled to a fiber optic. Their wavelength is around 870 nm. Previous studies at Sandia Labs show that this is the best wavelength to use in terms of the sensitivity of the switches to this light. The pulse duration was ~13 ns. Figure 3.2-1 shows the laser pulse intensity as a function of time. The total laser energy in each pulse is measured to be about 0.65 µJ at the end of the 300 µm diameter fiber.

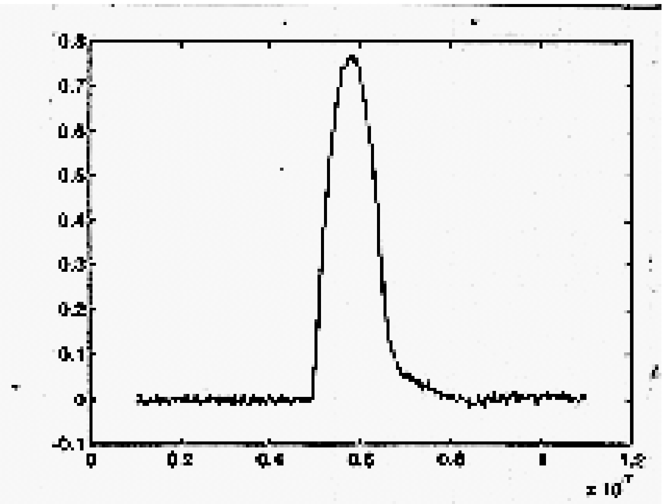

Figure 3.2-1 - The output of the laser diode array. The risetime in this waveform is 5 ns and the pulse width is 13 ns FWHM. The array's wavelength is 870 nm at 0.65 µJ per pulse.

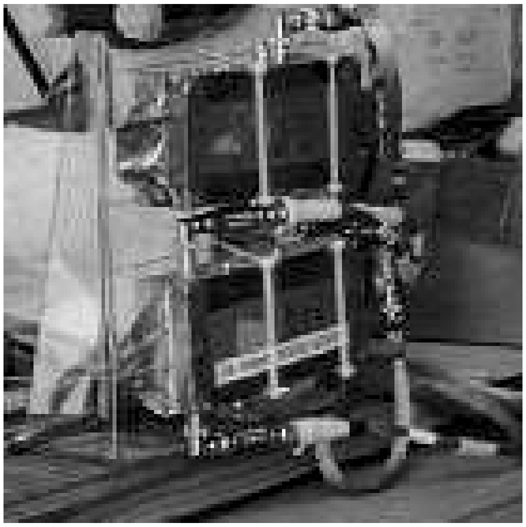

Figure 3.2-2 - Two laser diode arrays are contained in each metal box. The optic fibers route the output light to the PCSS.

The electronics that power this laser are built at SNL. In this case a single avalanche transistor is switched to deliver a pulse to the array. The package, shown in Figure 3.1-2, measures 2 in. by 2 in. by 1 in. The package requires a voltage of 400 VDC and a trigger. We are now using a small box that contains a DC power supply and a trigger generator to provide the inputs to the package. The power supply and trigger generator in the box are respectively about 3 in. by 1 in. by 1.5 in. (most of which is a DC to DC converter powered by 8 V) and 3 in. by 2 in. by 1 in. This laser can be used repetitively at up to 1 kHz. Thus, the assembled package size of a laser diode array, the electronics, the power supply, and trigger generator is less than 15 cubic in. (see Figure 3.2-2).

3.3) PULSE FORMING LINES

3.3.1) DOUBLE-SWITCHED LINE

The development of the pulse forming line (PFL), which ultimately provides the transmitting antenna with the necessary waveform, occurred over a period of 3 years. The GPR system requires a symmetric, “clean” bipolar pulse as input to the transmitting antenna, with a minimum of noise trailing the pulse. The first PFL design consisted of a single, 50-Ω transmission line switched at both ends with PCSS, shown in Figure 3.3-1.

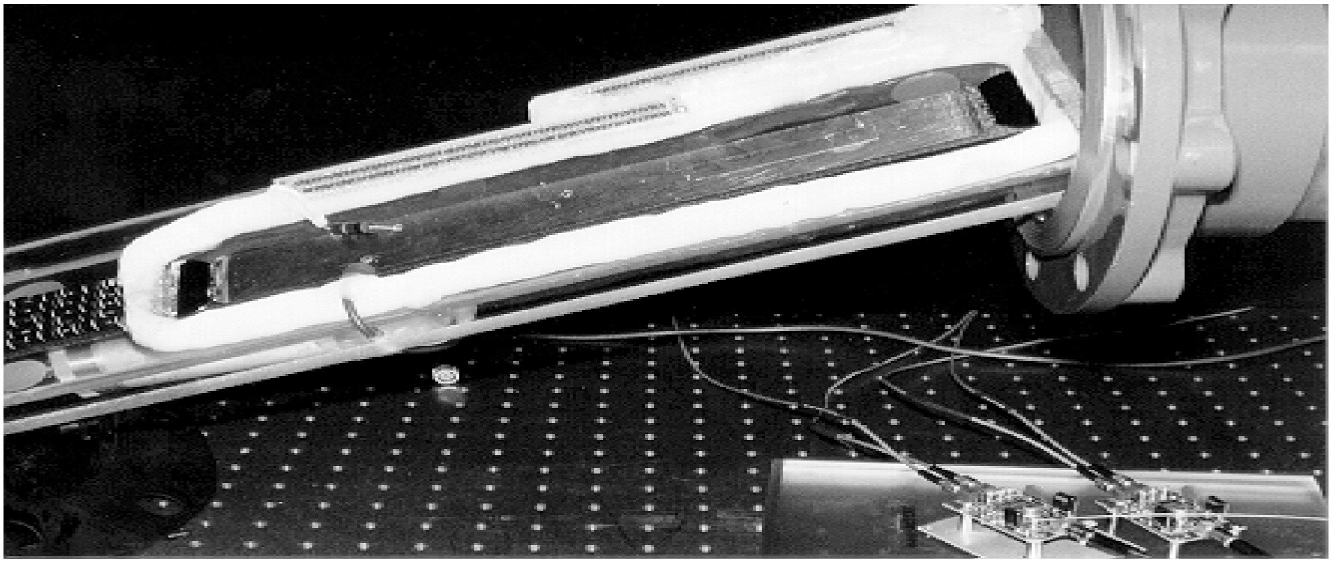

Figure 3.3-1 - Initial pulse forming line consisting of a length of transmission switched with PCSS at each end.

By switching at each end of the transmission line, a single bipolar pulse could be formed (see Figure 3.3-2). Switch jitter was a major issue in reliable and consistent production of a bipolar pulse. This line was used for the initial GPR work reported in the 1998 final report, SAND98-0724. As PFL output was increased to produce higher levels of radiated electric fields, PCSS size increased, and so did jitter in the triggering of the two switches.

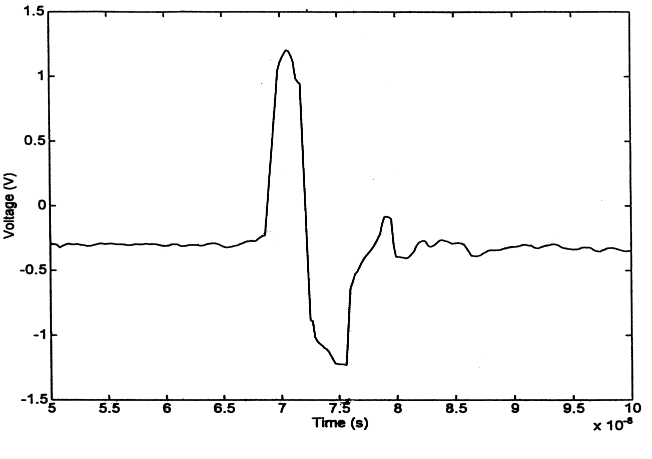

Figure 3.3-2 - Bipolar pulse produced by the 2-switch transmission line PFL.

3.3.2) FOLDED LINES

Eventually, the jitter in the 2-switch PFL became unacceptable (bipolar pulse generation unreliable) and a new design was needed. Theoretically, this same transmission line could be folded back on itself and need only one switch to produce both halves of the bipolar pulse. Figure 3.3-3 is a sketch of the design.

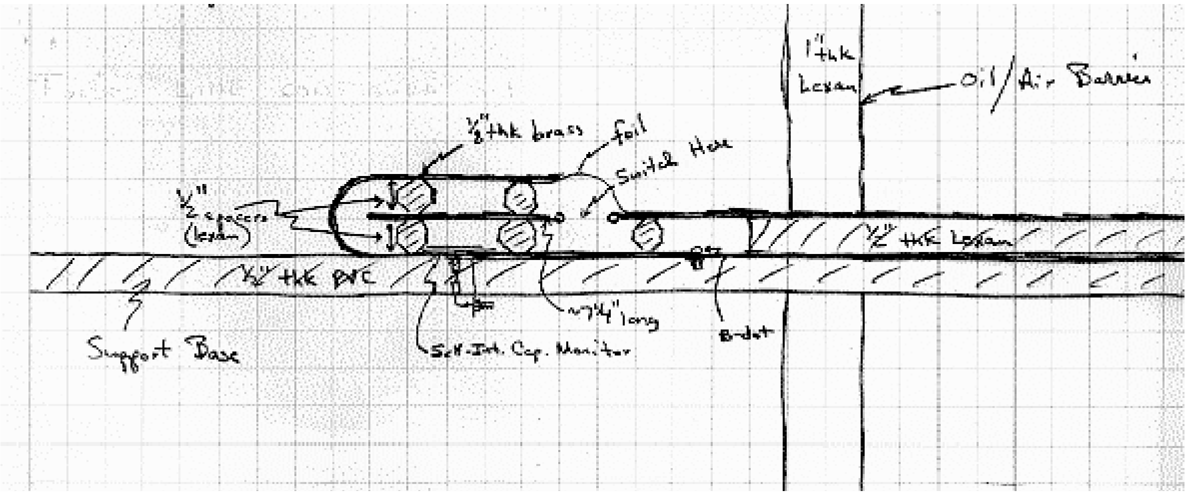

Figure 3.3-3 - Folded line PFL design.

The pulse produced from this folding is shown in Figure 3.3-4. The folded line delivered consistently a bipolar pulse, but the center frequency was low, approximately 140 MHz.

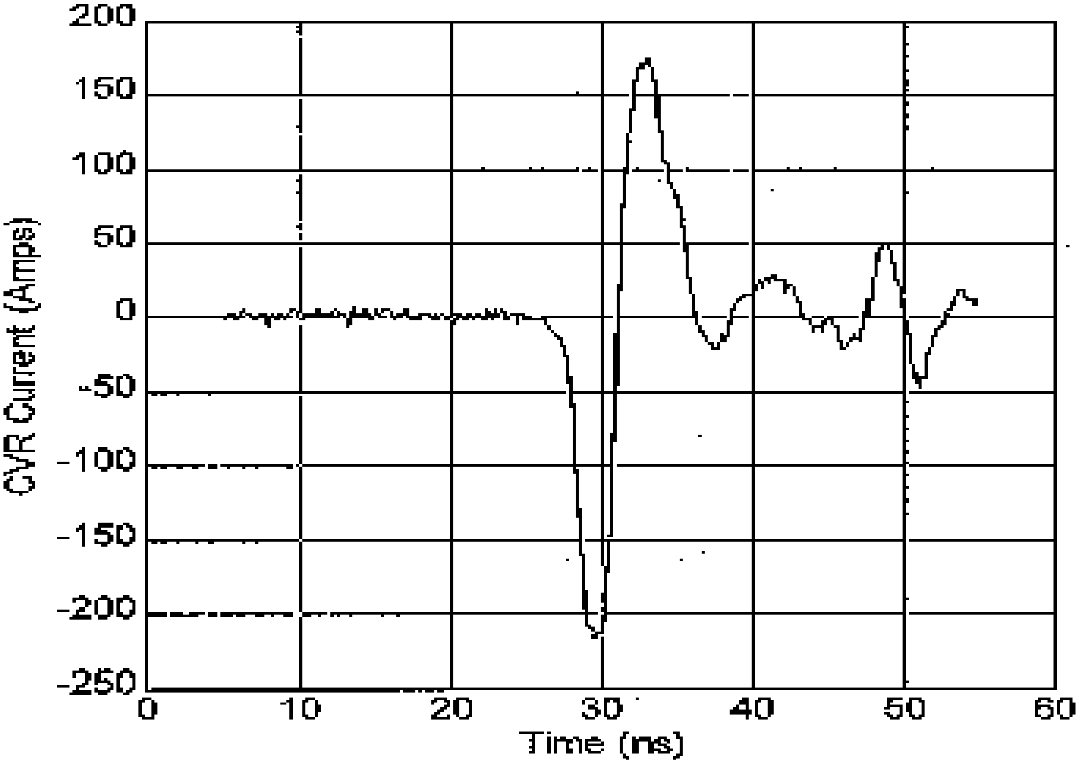

Figure 3.3-4 - Output pulse from the folded line PFL design. The measurement was made with a CVR at the end of a 50-Ohm transmission line.

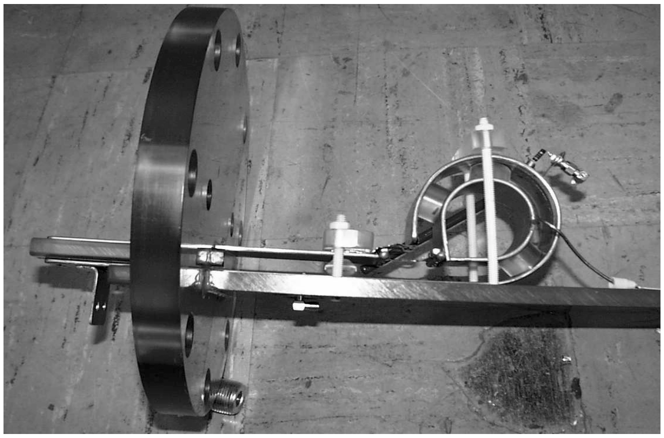

Figure 3.3-5 - Compact “Phillies” PFL ready to be inserted into modulator.

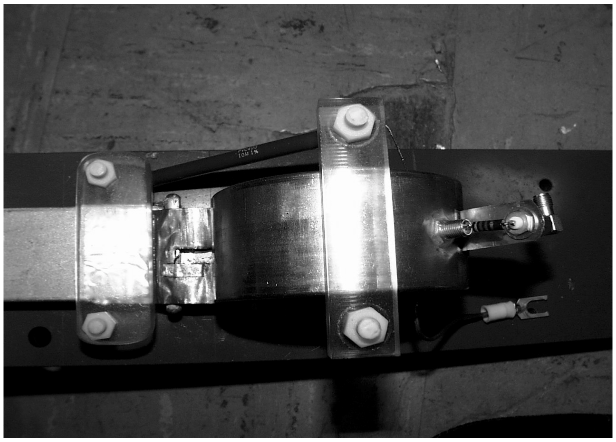

Figure 3.3-6 - Top view of the "Phillies" PFL. The PCSS is accessible through the rectangular cutout in the upper conductor of the transmission line

While trying to shorten the period of the bipolar pulse, a new design for the folded line was introduced which was more compact. This improved model was christened the “Phillies” line (see Figures 3.3-5 and 3.3-6).

The “Phillies” PFL pulse was shorter and had adequate frequency content in the 200 MHz – 300 MHz range; but the bipolar pulse (see Figure 3.3-8) was still followed by large-amplitude ringing and only about half the charging voltage was available in the generated pulse.

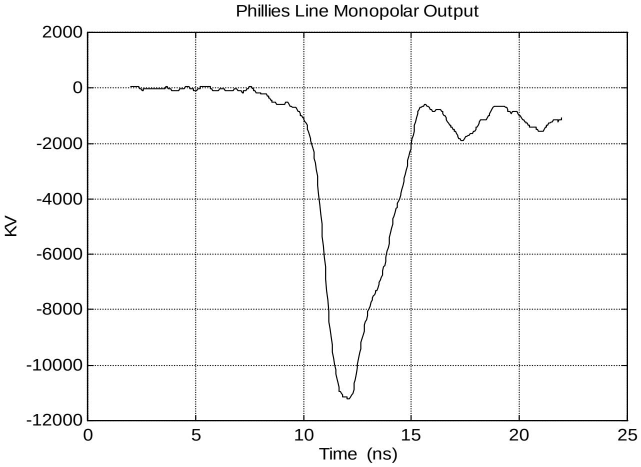

Figure 3.3-7 - "Phillies" PFL output when only the front half of the pulse is switched. The charge voltage is –30 kV.

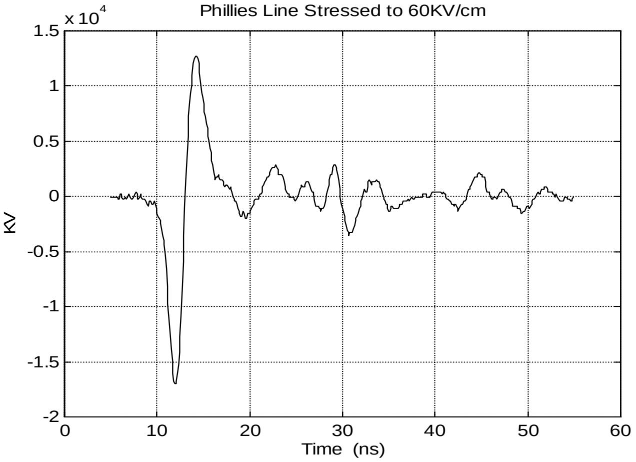

Figure 3.3-8 - 'Phillies" output when the complete PFL is switched. The charge voltage is –60 kV.

3.3.3) ROSS CIRCUIT

The need for a “better looking” pulse introduced another bipolar PFL design, the Ross circuit. The Ross circuit design produces the required bipolar waveform using a shorted-stub/transmission line. Figure 3.3-9 is a circuit model of the Ross circuit. A 3.35-in. length of 50-Ω transmission line is charged by the dual-resonant modulator, represented by the battery, and discharged by a photoconductive, semi-conductor switch (PCSS). The resulting unipolar pulse, with width < 2 ns FWHM, is injected into a

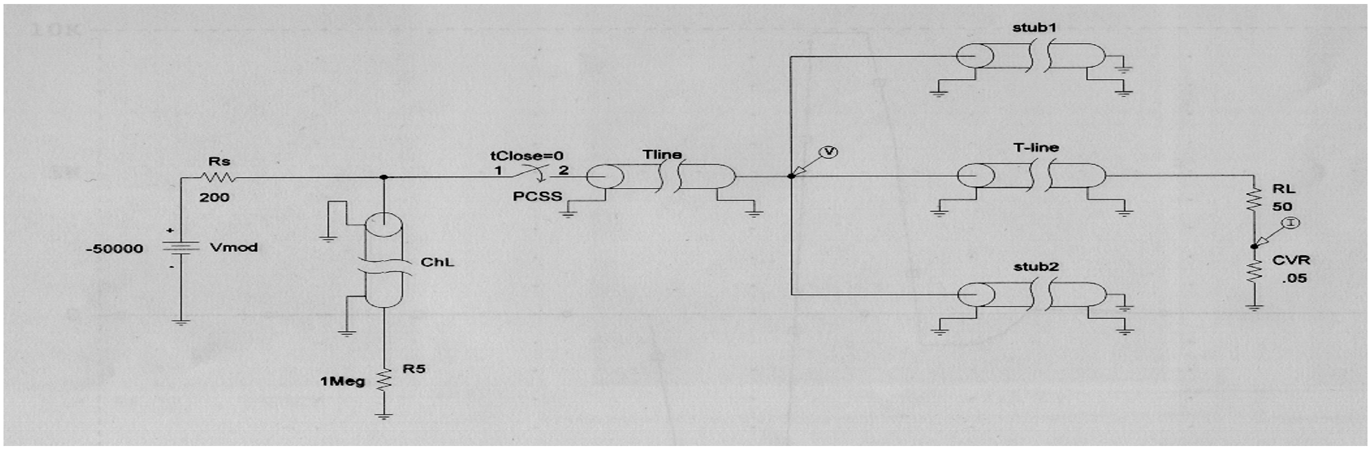

Figure 3.3-9 - Ross circuit model.

matched impedance transmission line. Branching off of this line are two shorted, transmission line stubs. Each stub is electrically half the length of the input pulse width. One fourth of the input unipolar pulse travels down each stub, inverts and reflects at the shorted end, and then adds onto the end of the original forward-traveling pulse. The circuit model in Figure 3.9 produces the bipolar waveform shown in Figure 3.3-10 at the circuit's output CVR.

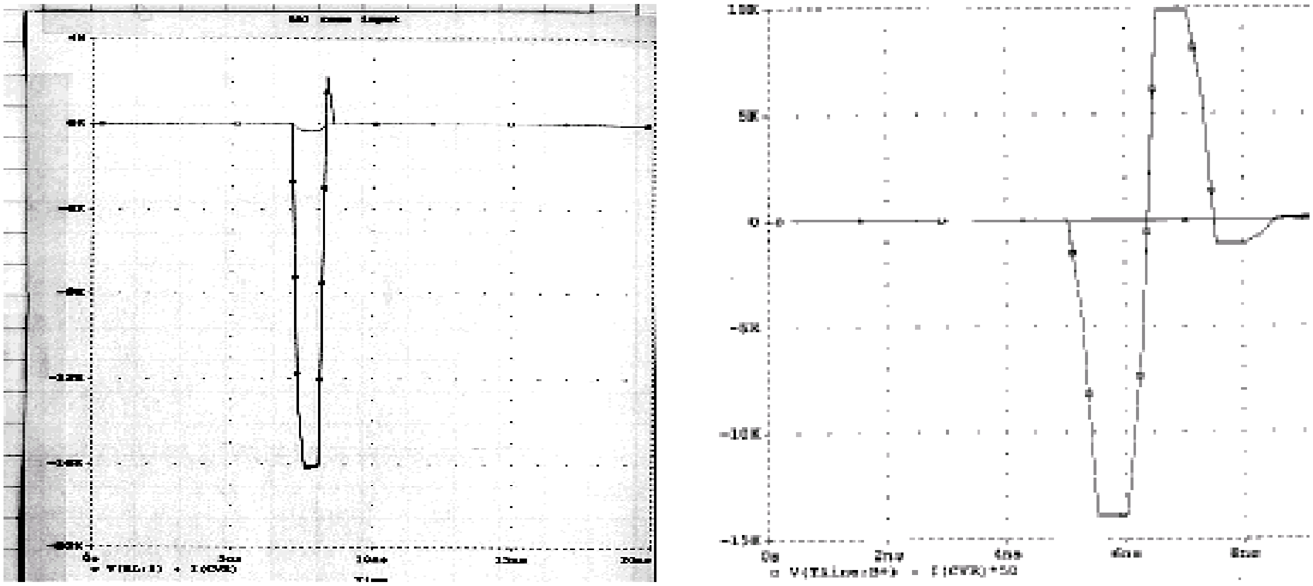

Figure 3.3-10 - Ross circuit model waveforms - unipolar input pulse and the bipolar output.

The actual hardware and resulting output pulse are shown in Figures 3.3-11 and 3.3-12, respectively. The input transmission line is oil-insulated while the Ross circuit, itself, is surrounded by air. The Ross circuit produced a consistent bipolar pulse; but also produced late-time reflections, which added clutter to the measurements. This circuit was also not extremely efficient. Only 70% of the Ross circuit's input voltage was available at the antenna input connection, but this was an improvement to the "Phillies" folded line concept. It was this design that was taken to Tech Area III/Bldg. 6640 and attached to an antenna in the fall of 1998 in order to begin making measurements. That work will be discussed later in this paper.

Figure 3.3-11 –Photographs of the input transmission line (left) and Ross circuit (right).

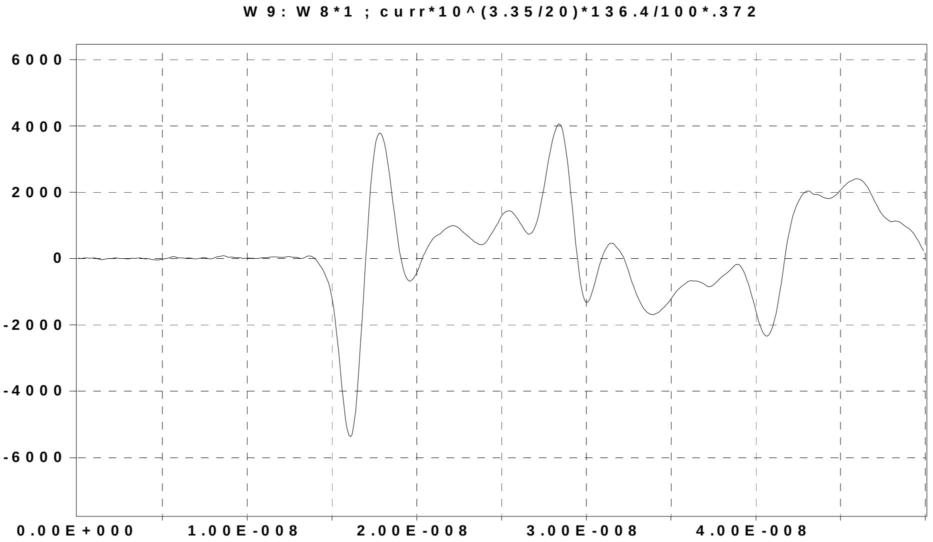

Figure 3.3-12 - Bipolar output pulse from the Ross circuit PFL.

3.3.4) FROZEN WAVE GENERATOR

After field testing the Ross circuit GPR in the Fall of 1998, development of a new, frequency-tunable, bipolar source began. The new source would be required to produce no after-pulse artifacts (or at least none after 5–10 ns); because reflected return signals from buried drums were expected to be small, and a transmit pulse with trailing components would clutter the measurement. The next generation source was designed around the frozen wave generator (FWG) concept illustrated in Figure 3.3-13. The outer conductors of the two 50-Ω coaxial transmission lines are pulse-charged to ±V/2. Closing the center switch, PCSS, launches a pulse in both directions out of each charged transmission line, which in turn add to ±V across the load (100 Ω) or antenna terminals. The crowbar switch was added to short out (crowbar) the forward going pulse after a single cycle. Hence, no late time features.

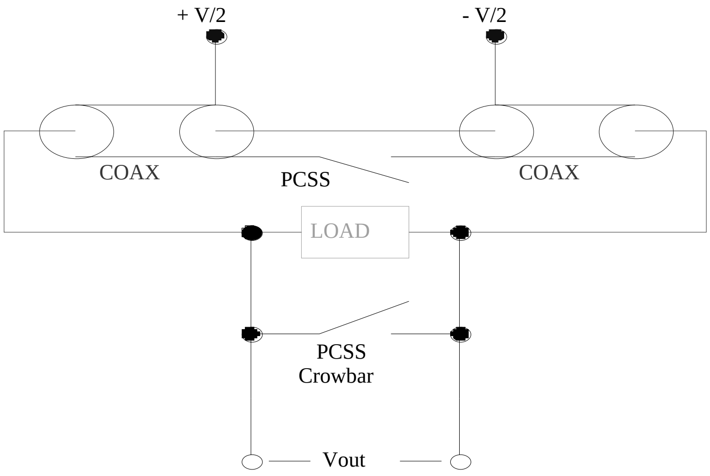

Figure 3.3-13 - Drawing of the frozen wave generator concept.

Data taken from an early benchtop prototype are shown below in Figures 3.3-14 and 3.3-15. The charge voltage in each case was ±3 kV. Circuit efficiency has been improved, and the after-pulse artifacts have been reduced. Instead of using a cylindrical coax, the conceptual design was folded back on itself and modified to a rectangular coaxial version. Views from the mechanical drawings of the field version of the FWG are shown in Figure 3.3-16.

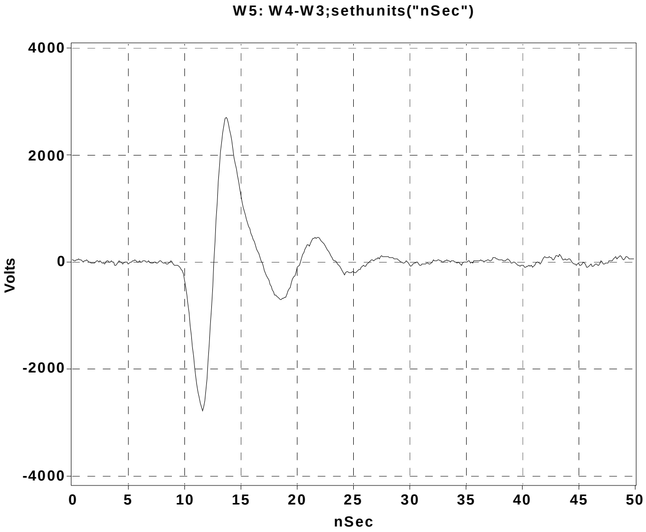

Figure 3.3-14 - FWG output pulse measured differentially across the circuit's output terminals. Crowbar switch not applied.

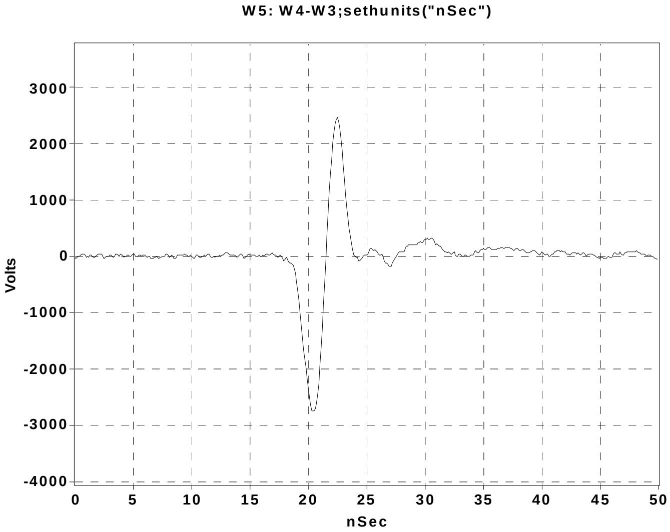

Figure 3.3-15 - FWG output pulse with crowbar switch applied.

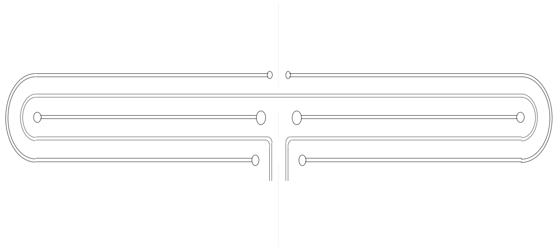

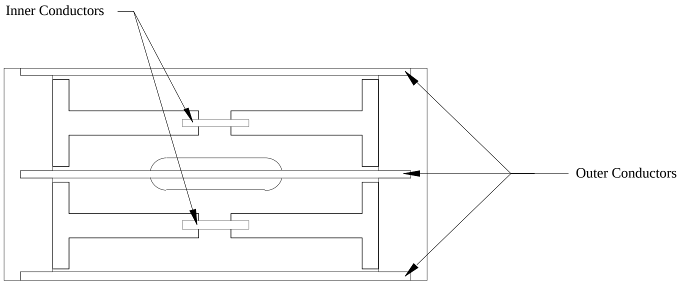

Figure 3.3-16 – Cutaway side (left) and end (right) views of the mechanical drawings of the rectangular coax FWG.

Photographs of the rectangular coax FWG are shown in Figure 3.3-17. Visible in the photographs are the outer conductors in aluminum and brass, the series charging resistors, and the antenna terminals. The inner conductors and the PCSS main and crowbar switches can be seen in Figure 3.3-18.

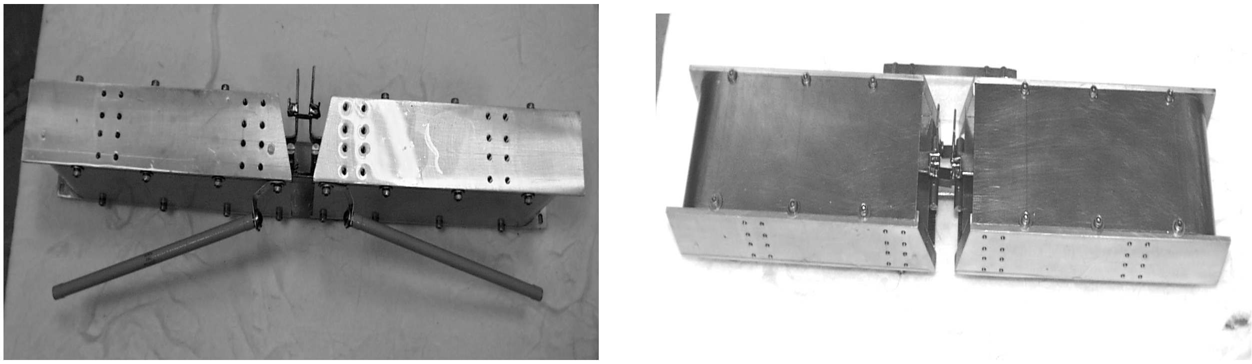

Figure 3.3-17 - Side (left) and bottom (right) views of the rectangular coax FWG. The housing measures 3-1/4 in. wide by 2 in. high by 16 in. long.

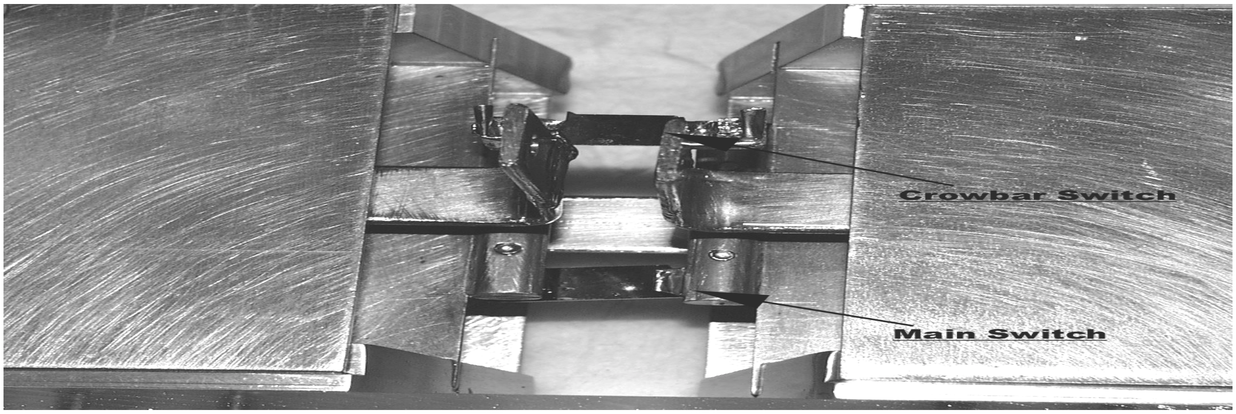

Figure 3.3-18 - Exposed center conductors, and main and crowbar PCSS.

The FWG was assembled as shown in Figure 3.3-19. The antenna terminals are in the foreground of the photograph. Connection to the charging resistors is achieved by the two white leads penetrating the back cover of the plastic box. When the FWG is running, the box is filled with silicone oil, which acts as the impedance-setting dielectric and high voltage insulation.

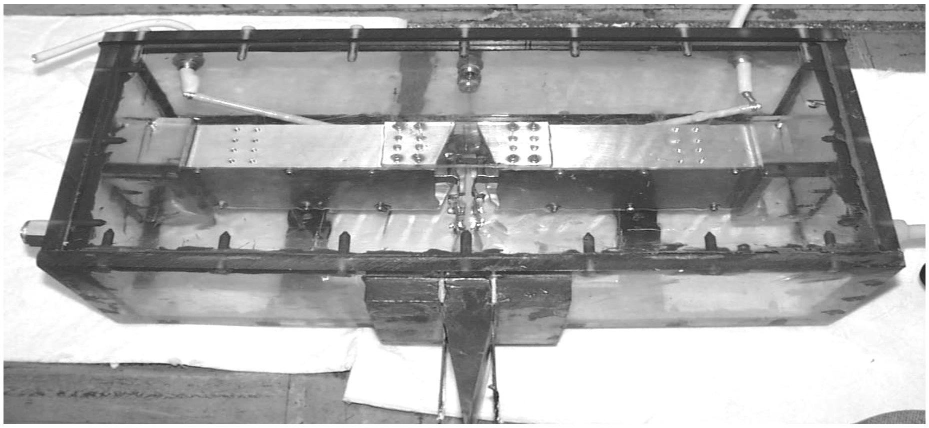

Figure 3.3-19 - FWG installed in its LEXAN box. 9 in. wide by 6-1/2 in. deep by 19 in. long.

Before the assembly was connected to an antenna, the antenna terminals were attached to a 100 Ω transmission line, which was terminated into a matched resistive load. When charged to ± 25 kV by the bipolar modulator, the output pulse, at the load, and its FFT, is shown in Figure 3.3-20. The output pulse measures 33 kV $_{\text{peak-to-peak}}$. Its frequency spectrum peaks at approximately 170 MHz, down ~5 dB at 250MHz. Accounting for PCSS "lock-on" losses of about 4 kV/cm of switch gap length (8 kV total), the FWG is delivering ~80% of its charging voltage to the load.

The second GPR system to be put into the field would be driven by the combination of bipolar modulator and frozen wave generator.

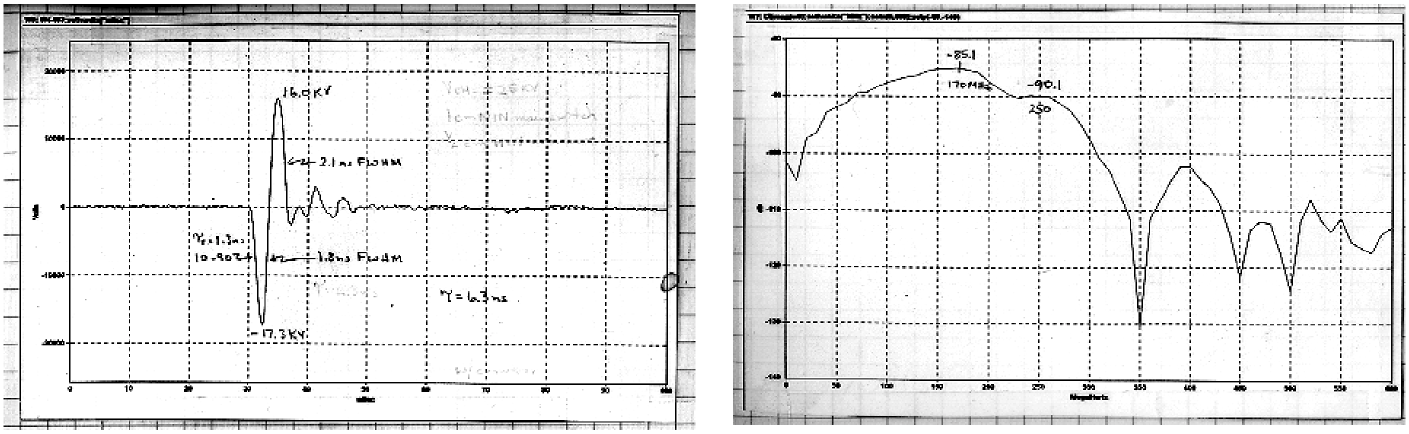

Figure 3.3-20 - FWG output pulse and its spectrum.

4) ANTENNAS

4.1) TRANSMIT ANTENNAS

4.1.1) SG ANTENNA

Two different antennas were used to transmit during the FY99 and FY00 GPR field tests in Tech Area III. In early FY99, an existing antenna (SG) (see Figure 4.1.1-1) was connected to the Ross circuit GPR system.

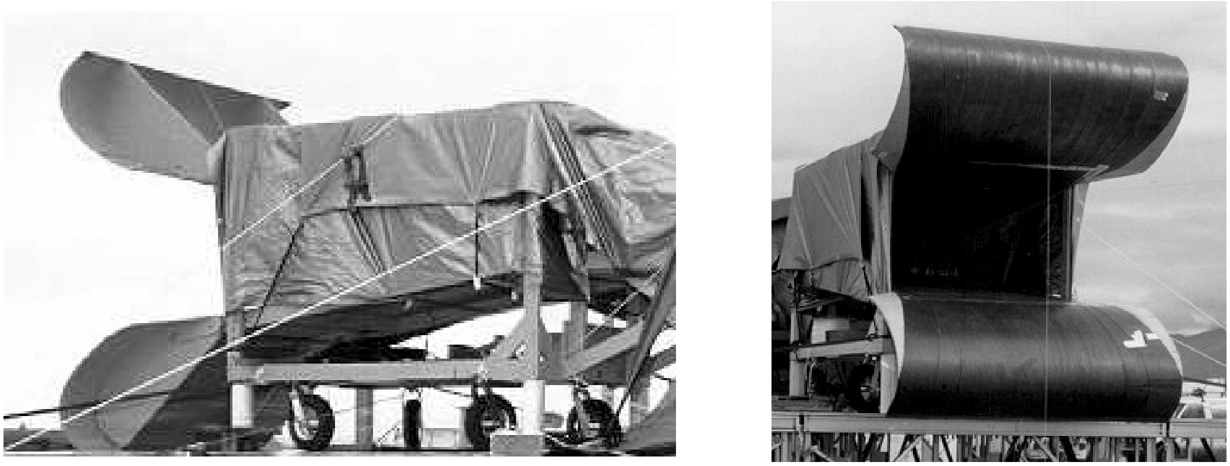

Figure 4.1.1-1 - Photographs of the transmit antenna used in the fall, '98, outdoor test. The antenna measures 6 ft. wide by 7 ft. high by 14 ft. long.

This antenna was described in an LDRD final report released in 1998 (SAND98-0724). At 200 – 250 MHz, the antenna acts as a derivative antenna, which is ideal for this application. Time domain reflectometer (TDR) data on the antenna and the transmission line connecting the Ross circuit to the antenna are shown in Figure 4.1.1-2. The change in system impedance is fairly smooth as it transitions from 50 Ω at its input to free space impedance (377 Ω) at the aperture of the antenna.

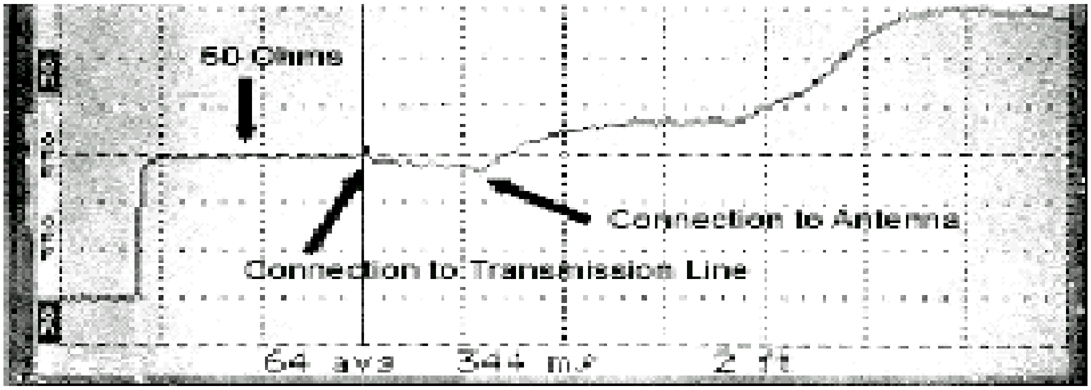

Figure 4.1.1-2 TDR data on the impedance changes between the Ross circuit and the output aperture of the antenna.

The input pulse to the antenna was monitored with a groundplane-version D-dot mounted in the throat of the antenna. This data will be presented later in the report. The antenna's output pattern, or electric field map, when driven by the Ross circuit, is shown in Figure 4.1.1-3. The mapping was accomplished by measuring the amplitude of the radiated electric field ($V_{pk-pk}/2$) in 5° increments on either side of the antenna's centerline with a free-field sensor positioned at a radial distance of 30 feet from the output aperture of the antenna. Note that the pattern is highly directional. Half power (-3 dB) occurs at ~± 20 degrees.

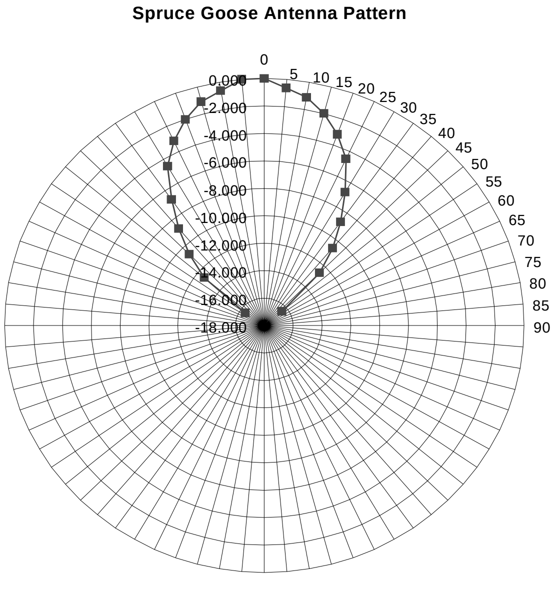

Figure 4.1.1-3 - Electric field pattern for the SG antenna.

4.1.2) DOUBLE RIDGE TEM ANTENNA

A second antenna was developed especially for the FWG GPR system during FY99 and FY00. Dr. John Aurand designed the double ridge TEM antenna (DRT) based on the required performance of the FWG GPR system. The theory behind the design is presented in a final report written by Dr. Aurand under Sandia contract BF-6512 (see Appendix A). Figure 4.1.2-1 is a drawing of the antenna built and used in the field in Tech Area III. The design has been scaled up by a factor of 9 from the model to provide optimum performance at the desired center frequency of 250 MHz. The antenna halves were cut out of two-inch thick, high-density foam in order to conserve weight, and then covered with copper foil to provide the conducting surfaces of the antenna. The two halves were spaced apart such that the input impedance would be 100 Ω and then gradually opened to terminate at the impedance of free space. Figure 4.1.2-2 is the TDR record of the DRT antenna from its input (~90 Ω) to the end of the flares (~200 Ω).

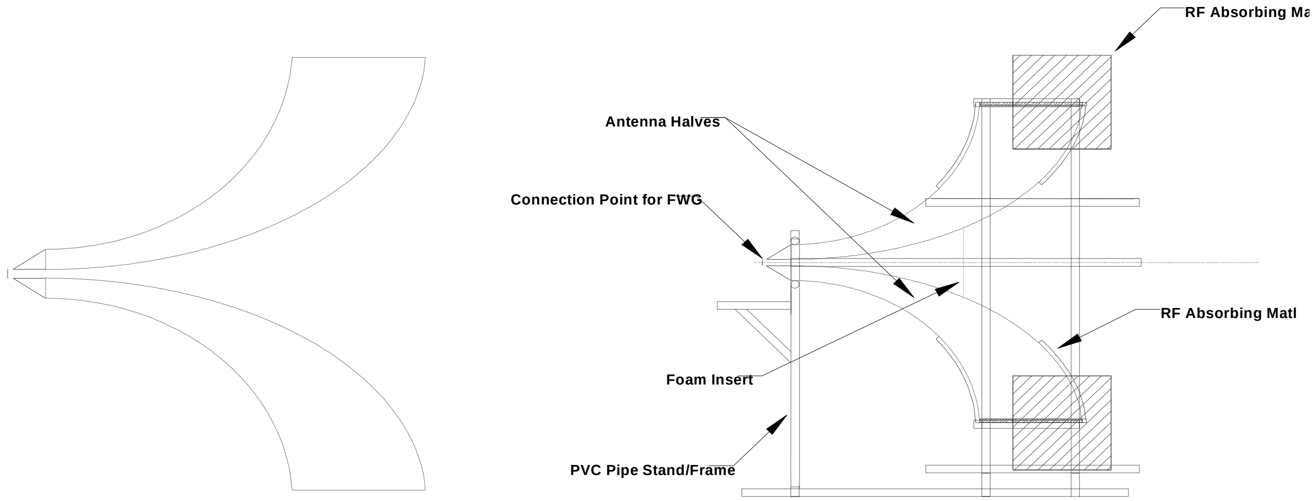

Figure 4.1.2-1 - Drawings of the DRT antenna alone (left) and installed in its support structure. The antenna assembly (on the right) was 3 ft. wide by 10 ft. high by 8 ft. long.

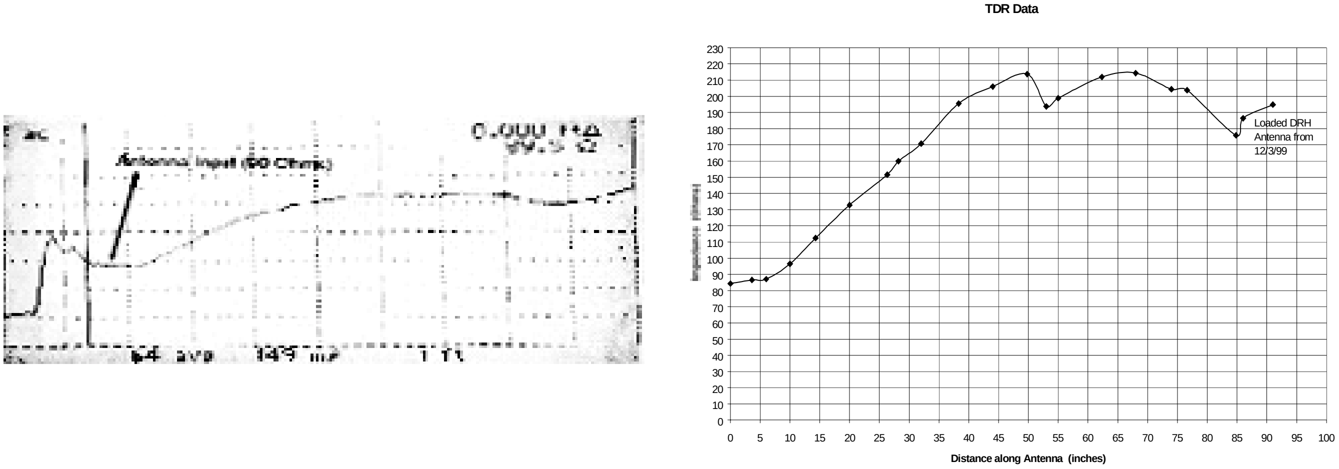

Figure 4.1.2-2 - TDR data on the DRT antenna and a plot of its impedance vs. distance along the inner conductor.

The PVC-pipe stand illustrated in Figure 4.1.2-1 provided support and maintained spacing for the two antenna halves. Carbon-loaded RF absorber material was attached to the output flares of each antenna half in order to reduce reflections from the ends of the antenna, which would introduce late-time ringing to the radiated RF. The shelf on the left side of the stand provided support for the FWG assembly, which attached to the parallel-plate input of the antenna.

Figure 4.1.2-3 shows the pattern of the radiated electric field; and a comparison of the patterns from the DRT antenna and the antenna shown in Figure 4.1.1-1. The pattern for the DRT antenna is somewhat broader, as the half-power points occur at ± 32° from antenna bore-sight.

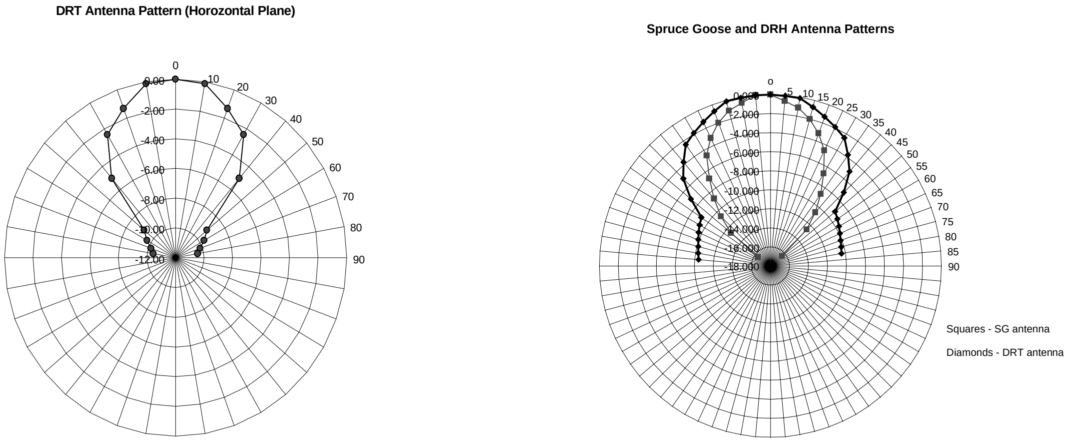

Figure 4.1.2-3 - Radiated electric field pattern of the DRT antenna (left) and a comparison of the two GPR antennas.

The input pulse to the DRT antenna was monitored using two groundplane-style D-dot electric field sensors (see Figure 4.1.2-4) and subtracting one signal from another.

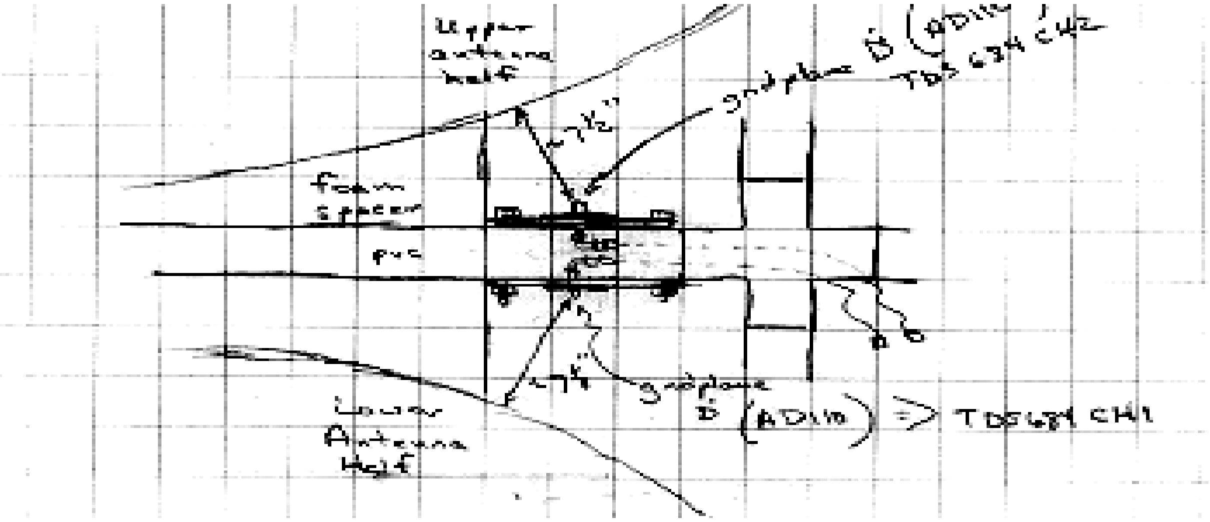

Figure 4.1.2-4 - Sketch of the differential monitor used to observe the antenna input pulse.

4.2) RECEIVE ANTENNAS

Three commercially available antennas were used to receive transmitted and reflected signals during the course of the two field tests. Each was initially selected for its particular capabilities and general ability to satisfy the following criteria: a) sensitive to the center frequency of the radiated RF from the transmitting portion of the GPR system b) fieldable, and c) provide a reasonable signal to noise ratio. Three commercial products were fielded, EG&G's ACD-4R D-dot free field sensor, Prodyn's B-100D(A) B-dot free field sensor, and A. H. Systems' Model SAS-200/570 DRG Horn Antenna.

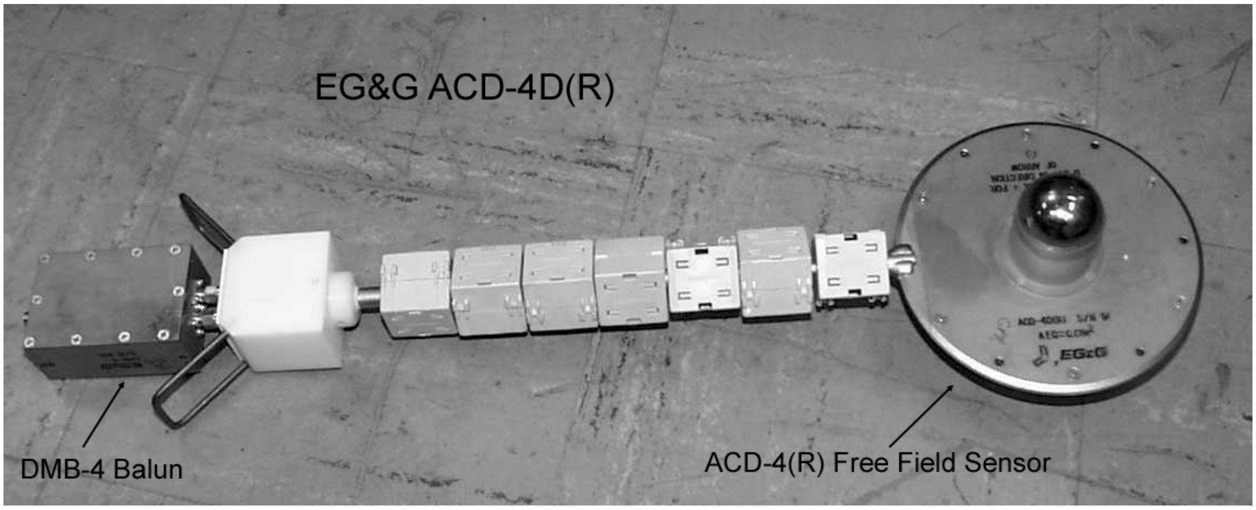

Figure 4.2-1 - EG&G ACD-4R sensor and DMB-4 balun monitor combination.

A photograph of the EG&G ACD-4R D-dot free field monitor is shown in Figure 4.2-1. The monitor consists of two parts, the free field sensor and a balun. The free field asymptotic conical dipole (ACD) sensor is used to measure time rate of change of displacement current (dD/dt) created by the presence of an electric field. The two asymptotic elements are accurately positioned on opposite sides of a common ground plane, and provide a differential output. A differential-mode balun transforms the balanced 100-Ω signal from the free field sensor to an unbalanced signal for input to a 50-Ω coaxial cable. After applying the correct relationships and integrating the signal, electric field strength can be

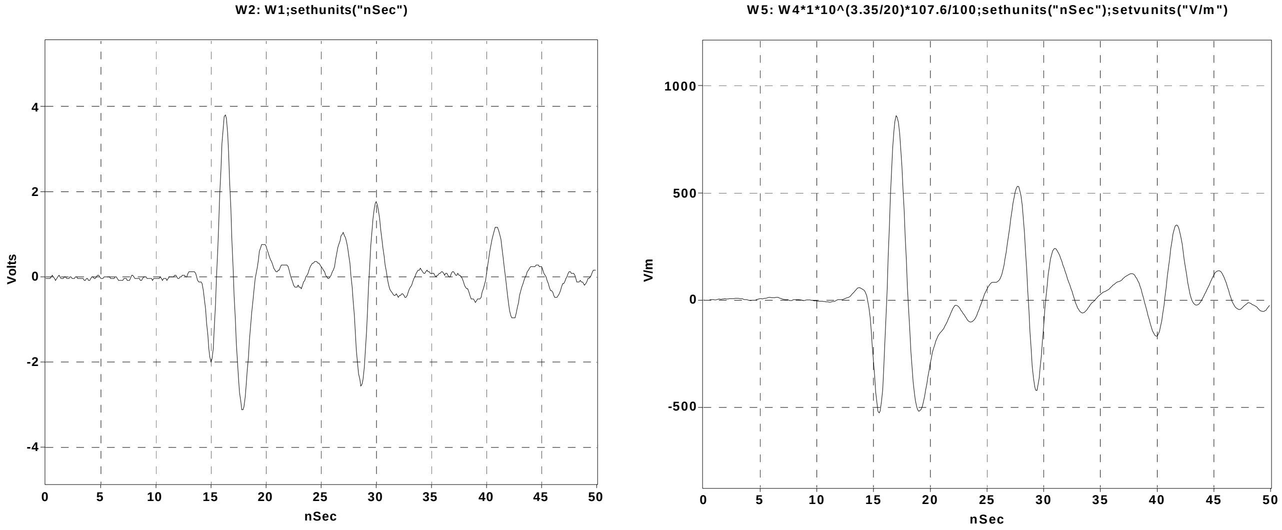

Figure 4.2-2 - Data taken with an ACD-4(R) D-dot. The waveform on the left is the raw data from the monitor. The trace on the left has been integrated and scaled to yield V/m.

derived. Figure 4.2-2 shows raw and scaled data captured by an ACD4 D-dot, placed 30 feet in front of and directly in line with the antenna aperture, from a pulse radiated by the dual-resonant modulator/SG antenna GPR during the field test in the fall of '98. The peak-to-peak amplitude of the raw signal is ~7 V. When used to monitor returns from a reflecting target, all of the receiving sensors were placed roughly 22 feet from the reflecting object at an angle of about 63° to bore site. The data collected from the reflected signal is shown in Figure 4.2-3. The waveform is inverted at reflection. The raw signal's amplitude is ~0.3 $V_{\text{peak-to-peak}}$. It is this signal that will be compared to the output from the other two receiving antennas.

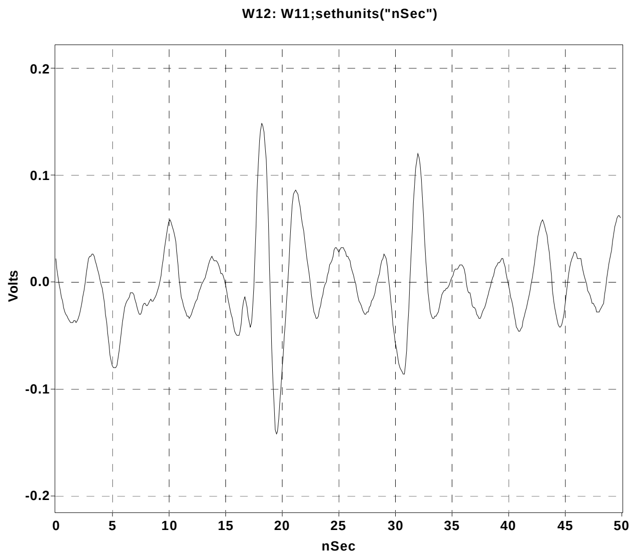

Figure 4.2-3 - Raw data from an ACD-4(R) D-dot measuring the reflected signal from a 55-gallon drum.

Another monitor used to detect reflected signals was the Prodyn Model B-100D(A) free field B-dot sensor, shown in Figure 4.2-4. A B-dot sensor measures the rate-of-change of a magnetic field in free space. This particular design is effectively a half-turn loop driving the output connector. A balun is used in conjunction with the sensor, as it was with the D-dot. Electric field strength can be derived after applying the correct relationships. Figure 4.2-5 illustrates data collected with the B-dot monitor. For the same output from the transmitting antenna, the output from the B-dot is only 0.03 $V_{\text{peak-to-peak}}$, in part do to its smaller sensor area. The benefit to using the B-dot is its directivity. By properly orienting the sensor, a source of "noise" (unwanted RF emissions from the GPR system) can be placed in a null, and not added into the reflected signal.

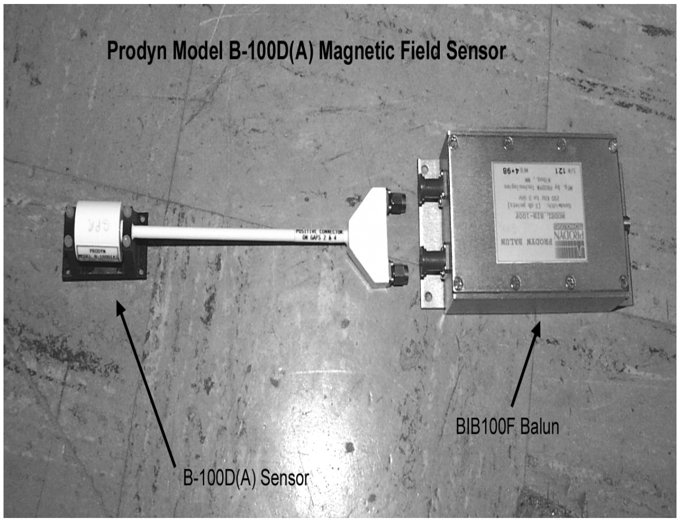

Figure 4.2-4 - Prodyn B-dot sensor and balun.

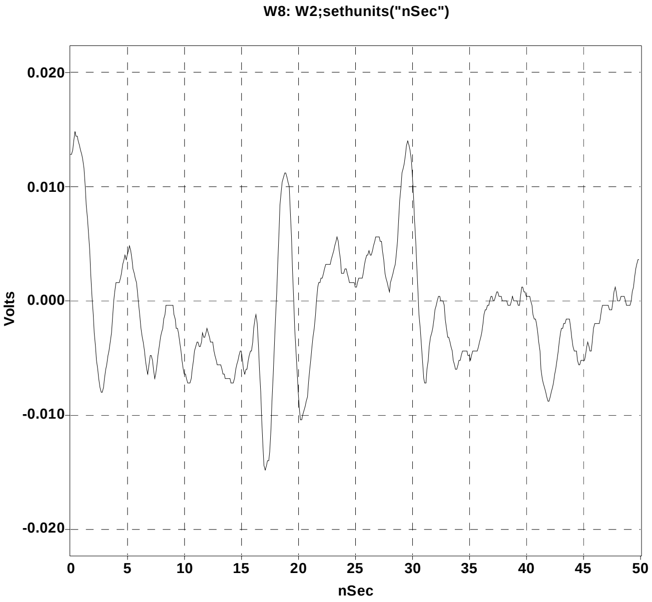

Figure 4.2-5 - Raw signal from the B-dot monitor.

The third and last receiving antenna applied to this project was a double-ridge horn antenna, Model SAS-200/570, made by A. H. Systems shown in Figure 4.2-6. The advantage in using this antenna was increased gain. The received signal's amplitude, shown in Figure 4.2-7, was over 20 $V_{\text{peak-to-peak}}$, but the signature waveform was masked by the amplified noise. Data analysis techniques used to

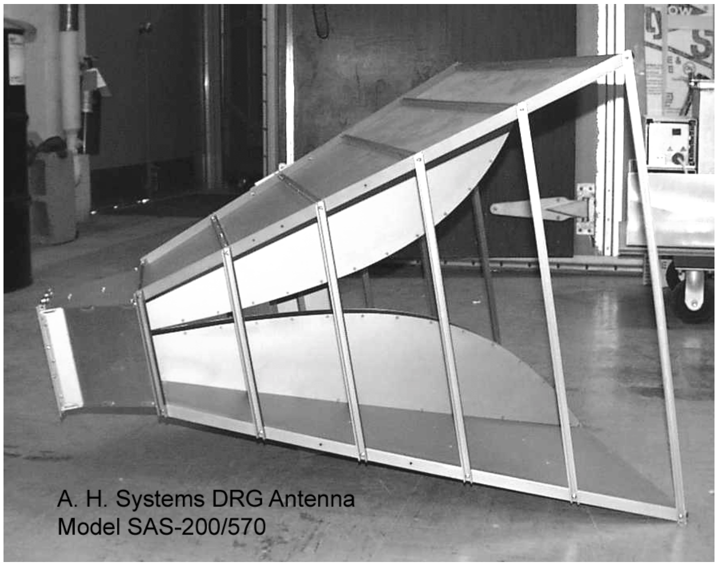

Figure 4.2-6 - A. H. Systems DRG Model SAS-200/570 antenna.

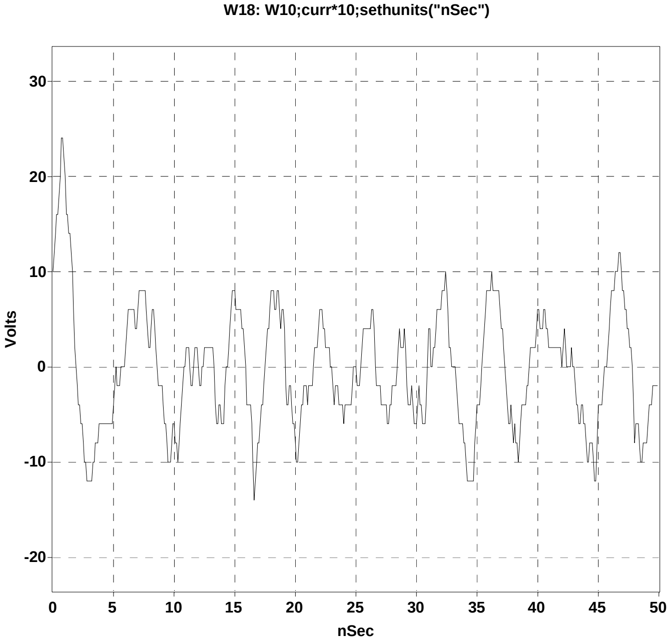

Figure 4.2-7 - Raw signal from the A. H. Systems antenna.

remove the noise will be discussed in the GPR systems portion of this report. Overall, the ACD-4 D-dot monitor was the sensor of choice, due to its relatively clean signal and reasonable signal output.

5) GPR SYSTEMS

Figure 5.1-1 illustrates the following five basic components, excluding the target, of the time domain GPR system; a primary power source, modulator, pulse forming network (PFN), transmit antenna, and a receive antenna (bistatic system). Each of these components has been described in a previous section of this report. The goal of the LDRD was to assemble the components and demonstrate system capability.

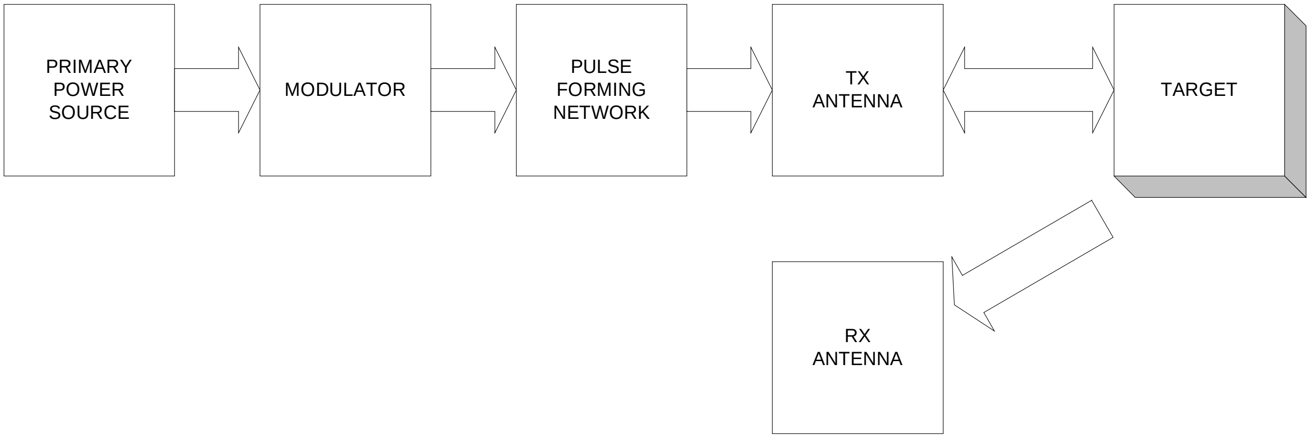

Figure 5.1-1 - Block diagram of the basic time-domain GPR system.

5.1) ROSS CIRCUIT GPR

The first such system fielded in Tech Area III/Bldg. 6640 was the Ross circuit GPR. Bldg. 6640 was chosen to be the test site for outdoor radiation because 1) this facility has an approved license from Sandia to radiate outdoors, 2) an elevated groundplane exists upon which to place the antenna, and 3) site control is easily achieved.

Primary power for the Ross GPR was 110 VAC from the nearby facility. The dual-resonant modulator was used to charge an LDA-triggered, PCSS-switched transmission line. The unipolar pulse from the transmission line was input to the Ross circuit, which in turn outputs a bipolar pulse to the SG antenna (Tx antenna). An EG&G ACD-4R D-dot (Rx antenna) was used to receive the reflected signal from a barrel target. The system components are shown in Figure 5.1-1 and the assembly in Figure 5.1-2. The transmitter assembly was placed on top of the groundplane in order to decrease the effect of ground bounce on the transmitted signal. The target drum is lined up on the antenna bore site, about 10 feet in front of the antenna. The Rx antenna is in front of the drum and off to one side. Figures 5.1-3 – 5.1-6 illustrate the pulses output from each section of the system.

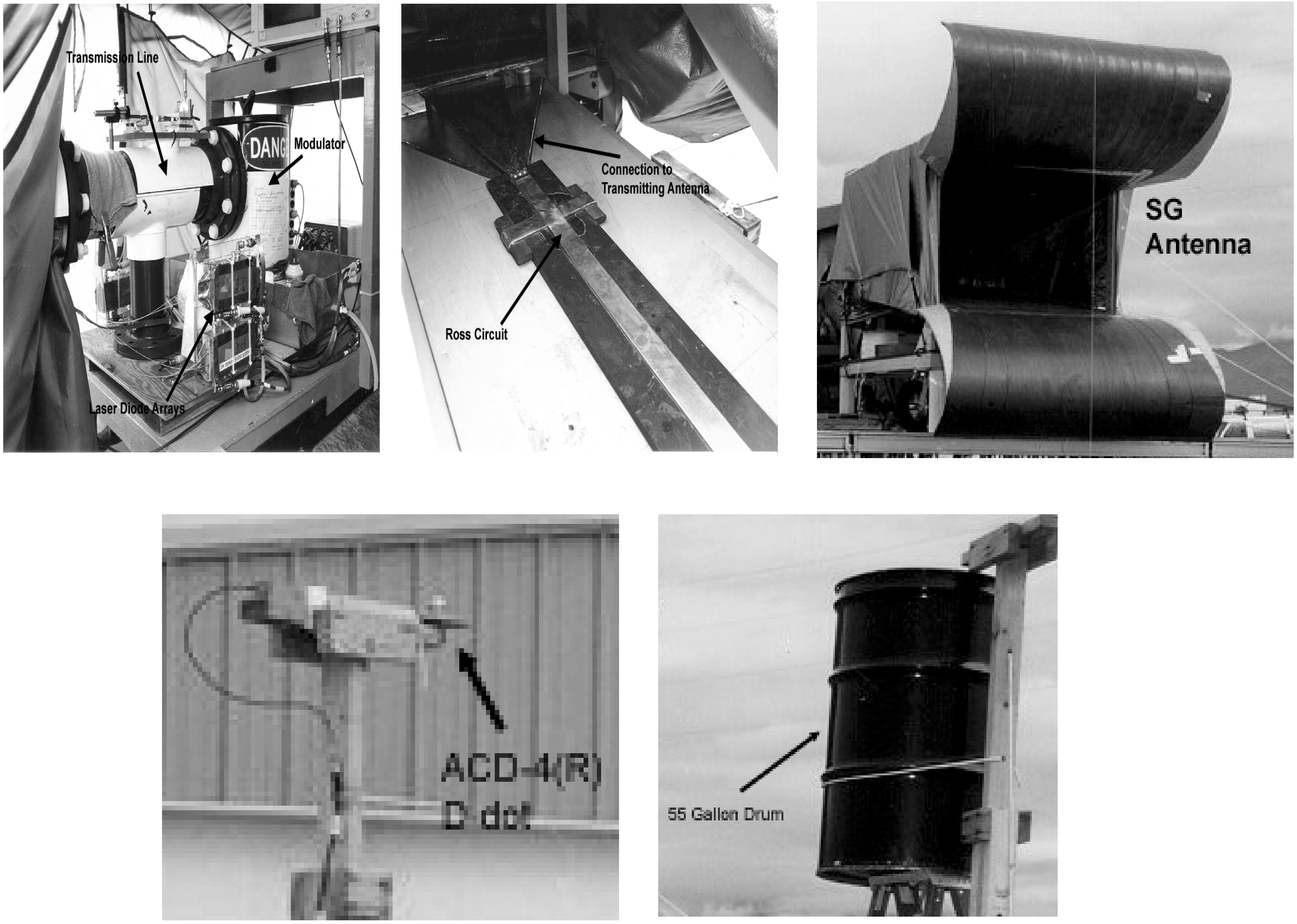

Figure 5.1-1 - Components of the Ross circuit GPR (u. left to l. right) - modulator and transmission line, Ross circuit, Tx antenna, Rx antenna, and drum target.

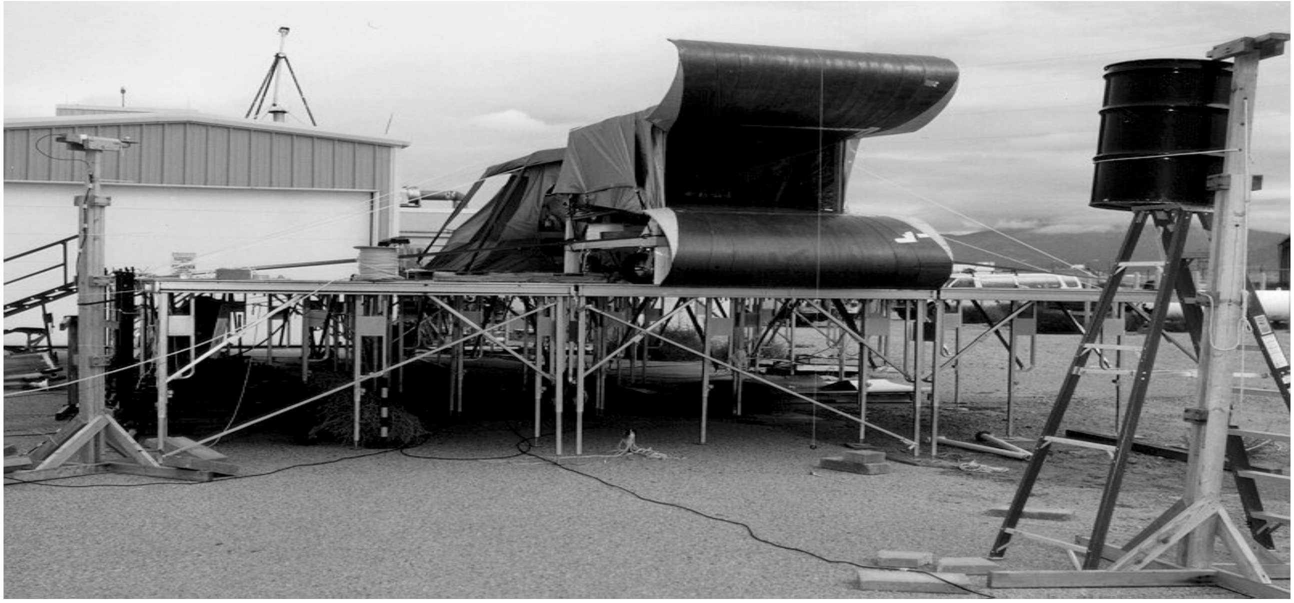

Figure 5.1-2 - Ross circuit GPR system assembled and operating on the groundplane immediately south of Bldg. 6640 in Tech Area III.

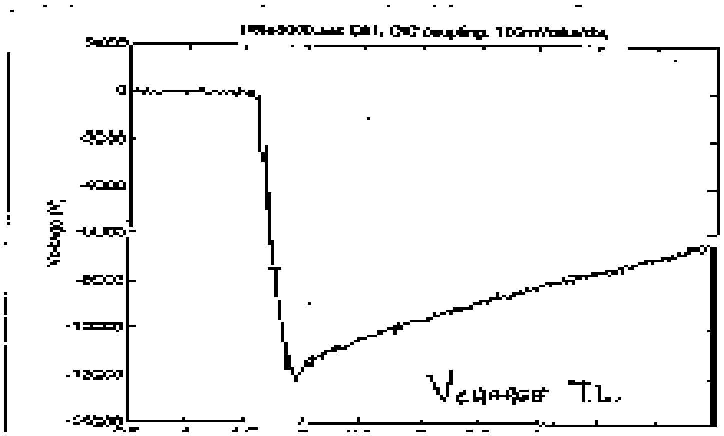

Figure 5.1-3 - Modulator output/transmission line charging waveform. V_{pk} = 12 kV.

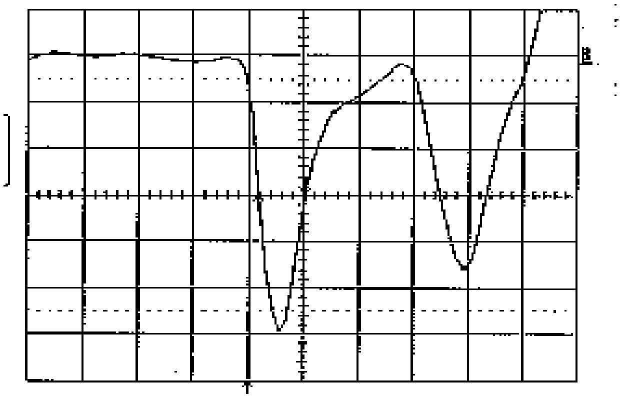

Figure 5.1-4 - Output pulse from the PCSS-switched transmission line. V_{pk} = -17 kV.

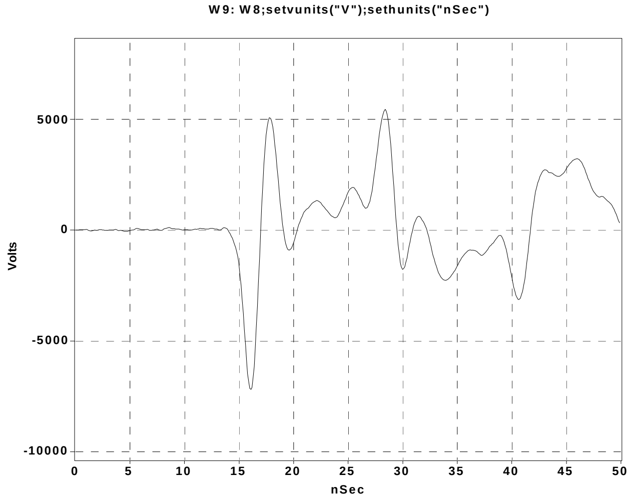

Figure 5.1-5 - Ross circuit output pulse/Tx antenna input. $V_{pk\text{-}to\text{-}pk}$ = 12 kV.

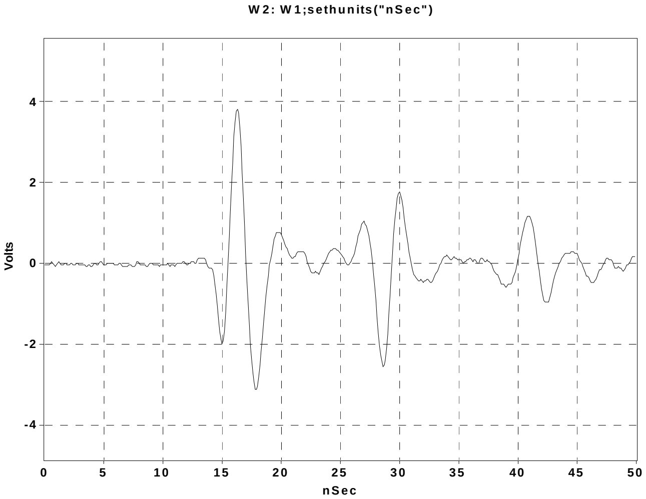

Figure 5.1-6 - Waveform radiated by the transmit antenna, as measured by a D-dot monitor.

In Figures 5.1-7 and 5.1-8, the analysis of the reflected signal from a barrel is illustrated. First, the signal reflected by the drum (the inverse of the transmitted signal), in air, is captured by the Rx antenna. Next, a background "noise" measurement is made. That is, the signal seen by the same Rx antenna is recorded when the system is pulsed, and a reflecting drum is not present. Finally, the background is subtracted from the drum return and the characteristic pulse appears.

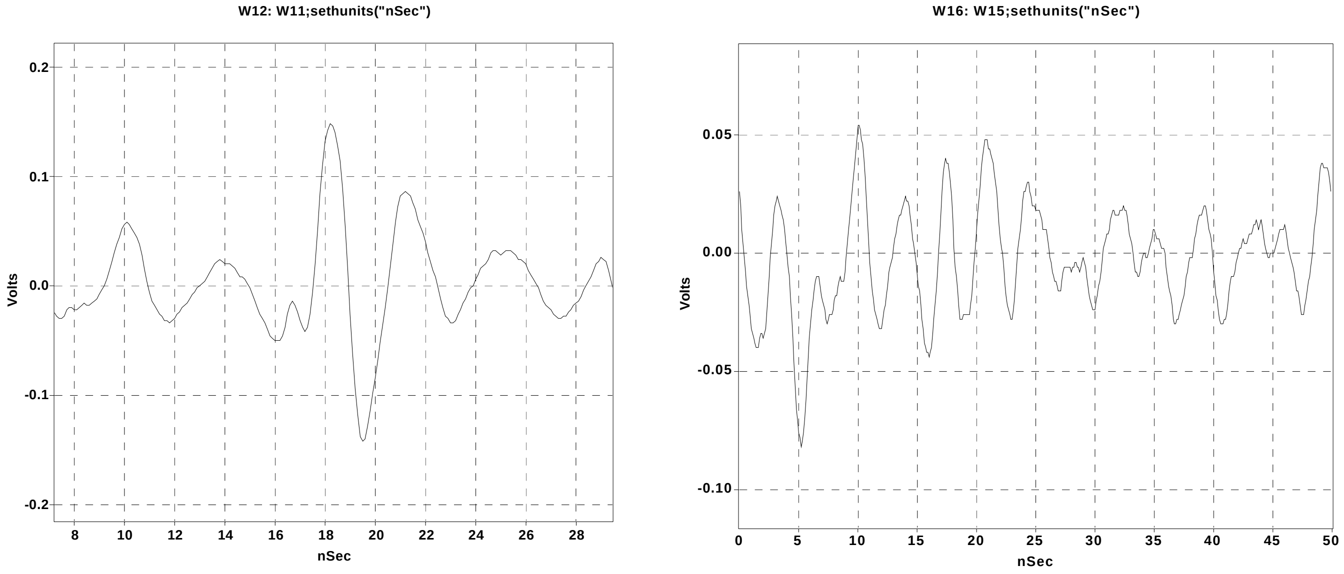

Figure 5.1-7 - On the left is the raw reflected signal from a 55-gallon drum. On the right, "noise" detected by the same monitor, when no barrel is present.

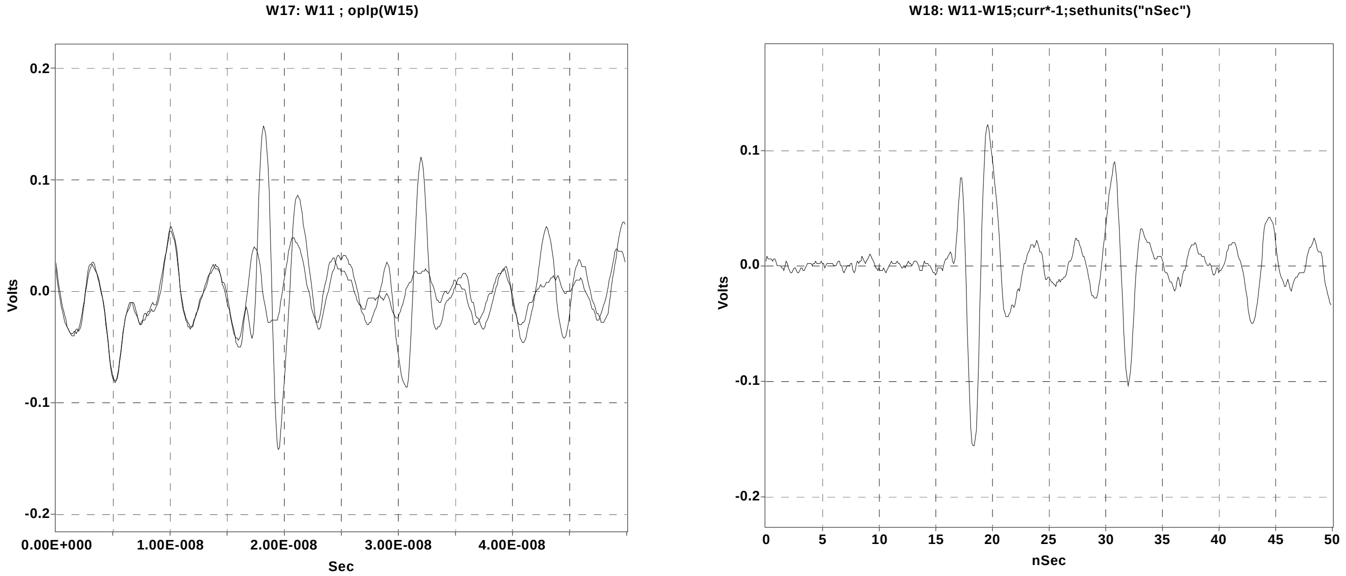

Figure 5.1-8 - Removal of background "noise" from the signal reflected by a 55-gallon drum. The frame on the left contains both the noise and the desired signature. The frame on the right is the result of subtracting out the noise.

Once the distance to the reflecting object is known, further filtering can be applied to the data to isolate the signature waveform; and the result would appear as shown in Figure 5.1-9.

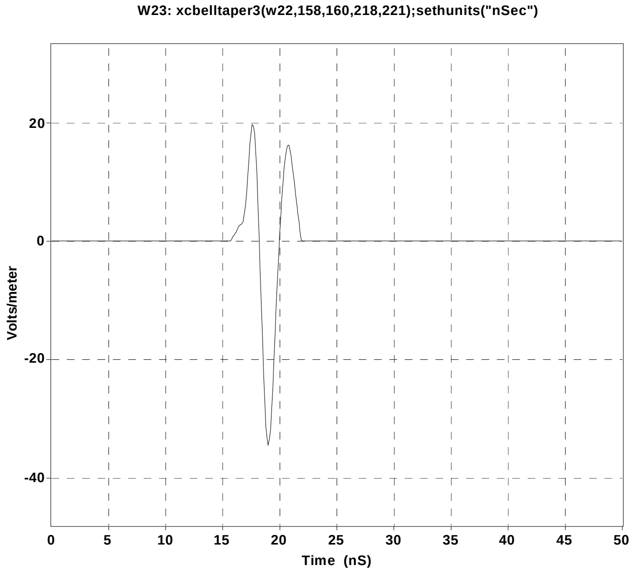

Figure 5.1-9 – Resulting waveform after applying filtering algorithms to a known-position drum.

Several other receiving antennas, as described in Section 4, were evaluated. The D-dot provided adequate signal amplitude, along with relatively low noise coupling, as long as the sensor was shielded from side-emitting RF from the antenna and Ross circuit. The B-dot free field monitor was less sensitive to the unwanted RF noise; but due to its small pickup loop area, yielded a factor of 10 less in signal amplitude. Less pickup would be a serious problem when attenuation through layers of soil comes into play. The double-ridge horn antenna provided the highest amplitude return signals; but also the most difficult signal from which to extract the barrel signature waveform.

This demonstration was performed in the Fall of 1998. A decision was made to design a more compact, fieldable system which would be used to look for buried drums. This decision initiated the design of the FWG pulse-forming network and the DRT transmit antenna.

5.2) FROZEN WAVE GENERATOR GPR

Referring back to Figure 5.1-1, the FWG GPR used 110 VAC for primary power, provided by either the 6640 facility or a generator. The AC power was converted to DC by a high voltage supply, which in turn charged the modulator. The dual-resonant modulator was replaced with the bipolar model described in Section 2. The bipolar pulse required as input to the transmit antenna would now be produced by the PCSS-triggered FWG PFN, eliminating the bulky transmission line/Ross circuit assembly. The DRT antenna was lighter and easier to handle than the SG antenna of the previous GPR system, but still was about 8 feet long and 8 feet high, due to the center frequency of the transmitted pulse. These components are shown in Figures 5.2-1 and 5.2-2. This GPR was also assembled on the groundplane at Building 6640.

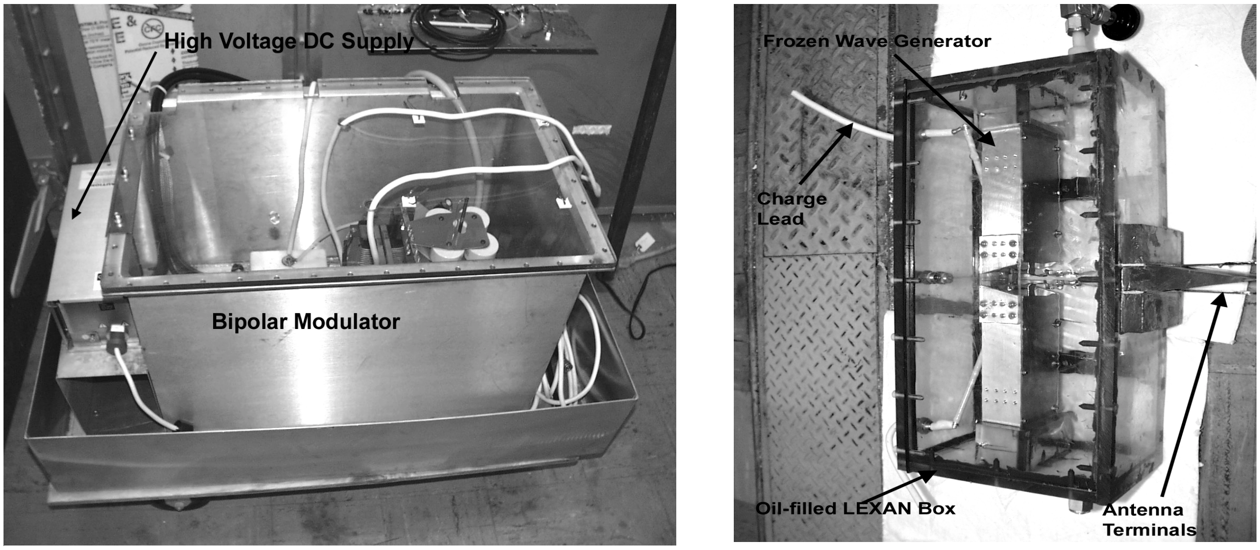

Figure 5.2-1 - On the left is the high voltage DC supply and bipolar modulator assembly, which provides the ± charge voltages for the FWG pulse forming network, shown on the right.

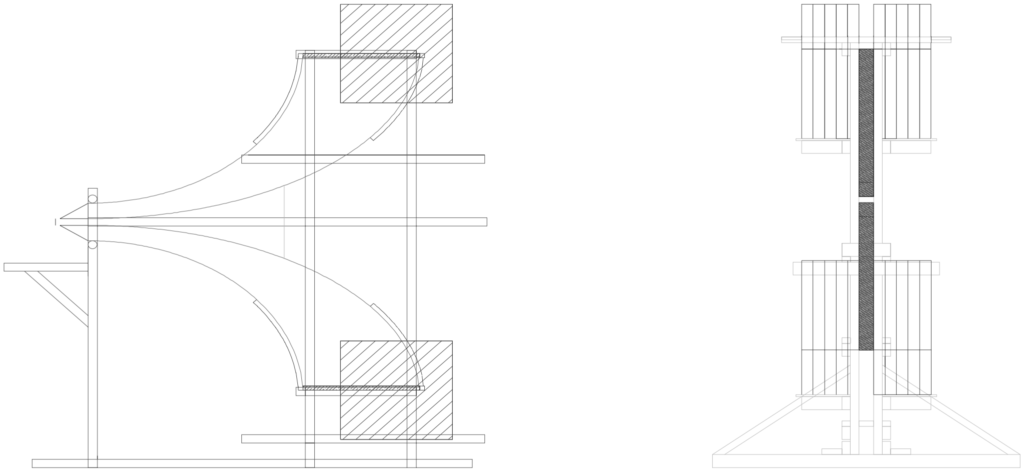

Figure 5.2-2 - Drawings of the DRT antenna used in the FWG GPR system.

Unfortunately, no photographs were taken of the FWG system before a 60-mph gust of wind destroyed the antenna. However, before it was damaged, data was collected on the system and is shown in Figures 5.2-3 – 5.2-4. The waveform on the left in Figure 5.2.3 is the positive half of the output pulse of the bipolar modulator. This pulse is the charging waveform for one-half of the FWG module. The main PCSS in the FWG is triggered at the peak of this pulse. The crowbar-PCSS is delayed from the main switch by the period of a single cycle. The resulting output of the FWG is shown on the right in Figure 5.2.3. This pulse is the input to the DRT antenna, which in turn radiates a derivative of its input. The radiated GPR signal from the FWG-based system is shown on the left in Figure 5.2-4. The signal

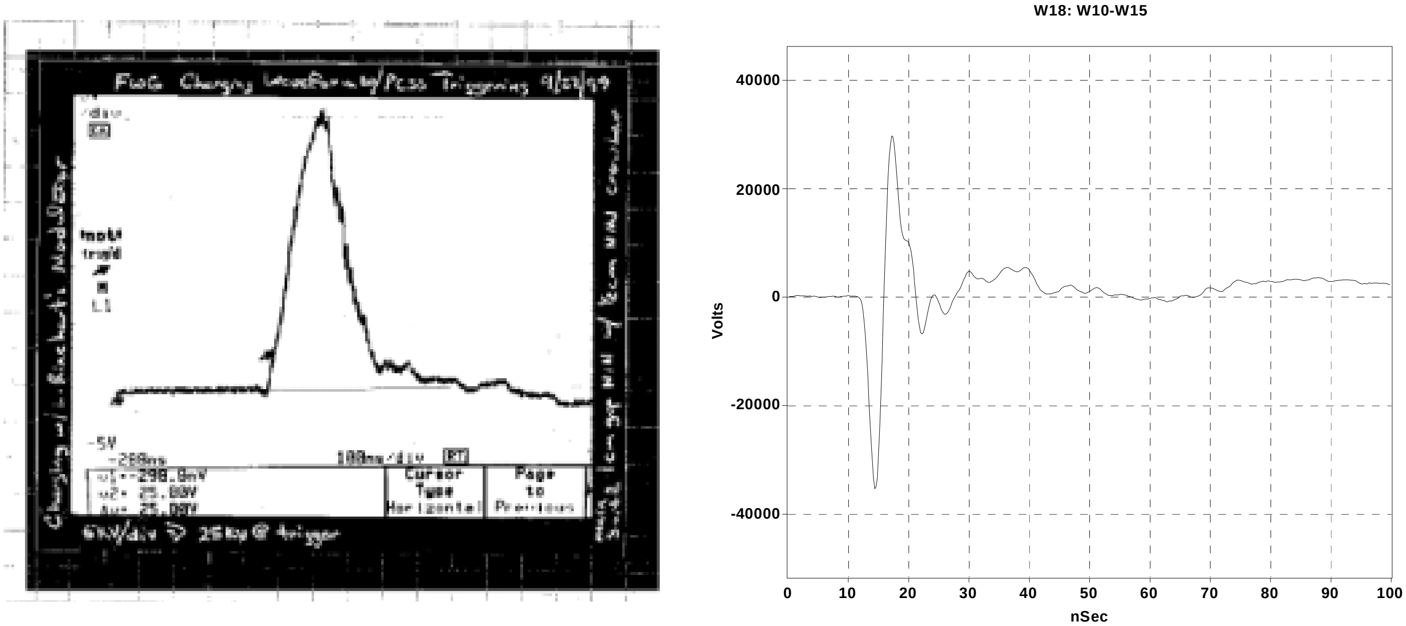

Figure 5.2-3 - On the left is the positive half of the output pulse from the bipolar modulator (V_{pk} = 25 kV). The waveform on the right is the resulting output pulse from both halves of the FWG, which is the input pulse to the DRT antenna.

shown in the Figure below is an improvement (little or no follow-on signal) over the Ross circuit output pulse shown in Figure 5.1-6. No target reflections were recorded before the system was damaged by wind gust.

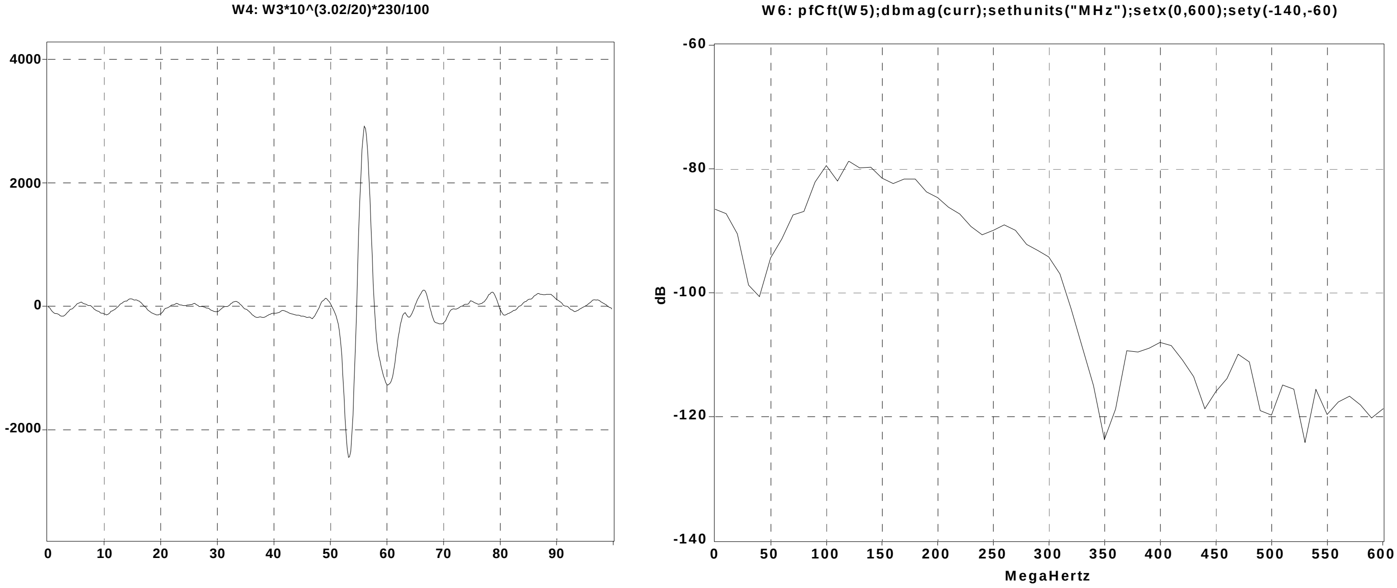

Figure 5.2-4 - The waveform on the left is the pulse radiated by the DRT antenna. On the right is the FFT of that waveform.

6) BURIED DRUM TEST

Prior to fielding the FWG GPR, the installation of a pattern of buried 55-gallon drums was nearly achieved. DOE and KAFB had approved the burial plan. The required environmental impact study and corresponding NEPA document had been completed, and a construction contact had been placed. One week before digging was to start the LDRD peer review committee cut the funding to finish the last year of this 3-year LDRD. The drawing shown in Figure 6.1 illustrates the proposed site, which would have allowed the project to take data on buried drums. The pattern was designed to: 1) minimize the square footage of disturbed soil, and 2) minimize reflected signal coupling from adjacent holes. Each hole would have been 6 feet in diameter and backfilled with sand. Figure 6.2 shows how the barrels

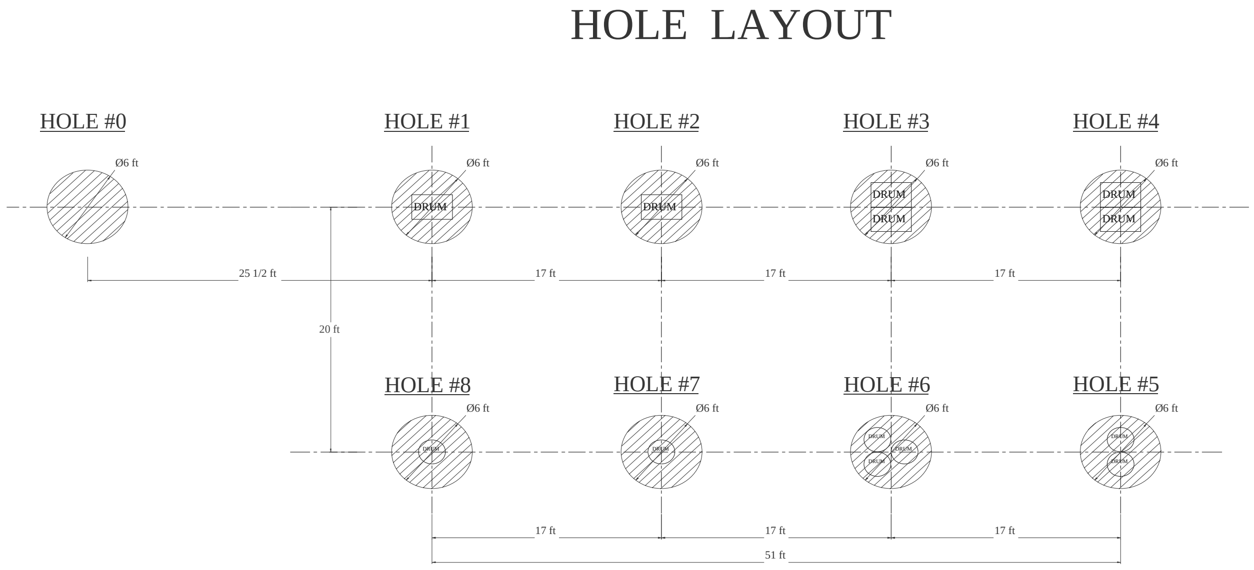

Figure 6-1 - Top view of the proposed drum burial plan.

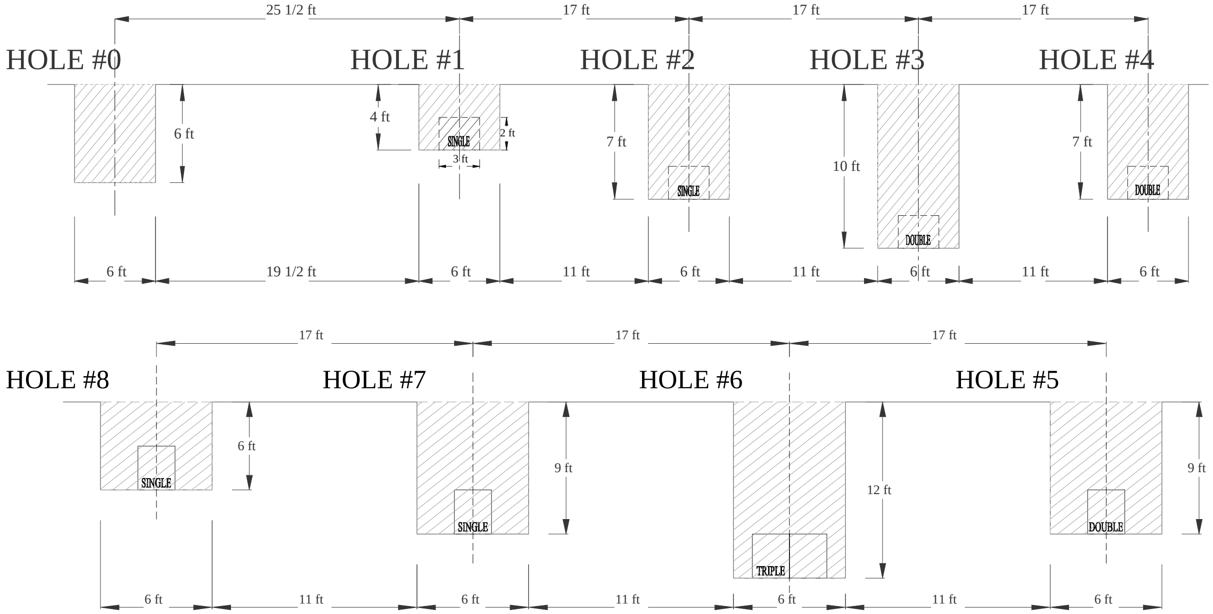

Figure 6-2 - Barrel layout for the 9-hole pattern. The barrels in Holes 1 – 4 would have rested horizontally, while in Holes 5 – 8, the barrels would have been positioned vertically.

would have been arranged in the holes. Hole #0 was to be the no-barrel control.

7) PROJECT CALCULATIONS

In the Spring of 1999, Dr. John Aurand, now with ITT AES, prepared a report for this LDRD investigating the propagation of ground-penetrating radar, and the quantification of the viability of the proposed high-power GPR system. This work was based on a sophisticated Method of Moments model developed by Dr. Larry Carin at Duke University to study the problem of scattering from buried mines. Dr. Aurand's report is included in this report.

8) CONCLUSIONS

The major initial challenge of the LDRD 'An Electromagnetic Imaging System for Environmental Site Reconnaissance' was to develop a system whose peak and average radiated power surpasses that of any other ground penetrating radar in existence. The direction taken was to develop an ultra-wideband (UWB) or direct time-domain radar. Two such systems were designed, built, and tested. Both the Ross circuit and the FWG system demonstrated the capability to radiate the pulse shapes required by theory to detect buried 55-gallon drums. The FWG/DRT antenna system was an improvement in system size and in the fidelity of the radiated signal.

Both GPR systems used photoconductive semiconductor switches (PCSS) to discharge the pulse forming networks. These switches provided for reliable and consistent generation of the transmitted signal, with the lifetime required of a practical system.

Unfortunately, the project's funding was cut off before the final experiments could be done.

APPENDIX A
Double-Ridge TEM Antenna Design for High-Power GPR System

Dr. John Aurand

July 16, 1999

2^{nd} & Final Report
Work Sponsored by Sandia National Laboratories
Contract BF-6512, Dr. Guillermo Loubriel

Introduction

This report describes the development of a bistatic transmit/receive (tx/rx) antenna system for use with a high-power VHF transient pulser in a ground-penetrating radar (GPR) system. This work was performed under contract to Sandia Labs, for the LDRD ‘An Electromagnetic Imaging System for Environmental Site Reconnaissance.’ The purpose of the antenna work is to design and develop appropriate antennas for this particular GPR system. The overall purpose of the GPR system is to detect buried 55-gal. drums in environmental reconnaissance applications.

Scale-Model Antenna Development

An identical pair of small antennas were designed and optimized for this project. They were scaled up in frequency (down in size) to permit clean antenna radiation measurements within an indoor lab environment. The primary operating band was 1 GHz to 3 GHz, with the intention that when finished, they would be scaled back down in frequency for correct VHF operation.

Because this GPR system is a transient or direct time-domain system, the antennas had to have clean time response (in terms of both input ringdown and radiation/reception), and fairly wide bandwidth (about a decade in frequency ratio). As a result, some type of transverse electromagnetic (TEM) antenna would be used. In addition, because of the large wavelengths involved in the VHF band, it was desirable to minimize the physical size of the antennas. Thus, a flared profile was deemed necessary for efficient radiation over broad bandwidth in a compact size. Fortunately, the limit which this size constrant imposes on antenna gain was acceptable because of the additional requirement that the main-beam beamwidth be sufficiently broad for suitable use in a scanned synthetic-aperture radar (SAR) operating mode.

A further requirement for clean transient radar use is that the antenna ringdown be sufficiently minimized to provide an easy identification of target echos amongst possible late-time ringing of the antennas or system components. So the decision was made to incorporate lossy loading of the antennas in order to minimize ringing, especially difficult given the compact electrical size required.

The last requirement was one of input transmission-line topology. The high-power frozen-wave generator has a 100-Ω parallel-plate output line, driven with a floating bipolar voltage pulse. Thus, the transmitting antenna has to mate to a 100-Ω parallel-plate line, and be fully insulated from other parts of the GPR system. The receiver will consist of an oscilloscope with 50-Ω input, and the associated coaxial transmission line. So the receiving antenna has to mate to a 50-Ω coax input.

The scale-model antennas were designed with a 50-Ω coax input (SMA female connector) for straightforward measurements. A scaled version of it may be used directly for the VHF receiving antenna, whereas the VHF transmitting antenna will start with a 100-Ω parallel-plate input instead. The overall size of the two will be about the same – the primary difference will be the feed transition designs.

After careful study of a wide variety of TEM antenna topologies – including the extreme cases of parallel-plate geometry (like conventional TEM horns, and with low impedance) and tapered-slot geometry (also coplanar or finline, and with high impedance), we decided to design a new hybrid configuration – we call it the double-ridge TEM antenna. It consists of a pair of flared ridge conductors (like parallel-plate, but with ridge sides attached to the plate edges). As far as we know from the literature, this is a new variation of TEM antenna. It is designed at the feed to mate to parallel-plate geometry, and as it flares apart, it behaves more like a tapered slot antenna, which has the desirable characteristic that the main beam is very symmetrical. This is good for clean SAR processing later on.

The basis for the well-behaved main beam is that the electromagnetic (EM) field distribution in the antenna has comparable tapers in the E-plane and H-plane. In contrast, conventional TEM horns (with parallel-plate cross-section) have very unequal E-plane and H-plane beamwidths, as well as decreased gain due to externally-cancelling fields. Fig. 1 shows the electric field distribution of a hollow section of double-ridge line, corresponding to the actual cross-section of the scale-model at a longitudinal position halfway out from the feed to the aperture. Compare this to Fig. 2, which depicts the electric field distribution for the same size parallel-plate line. Note that the surge impedance is much lower with the ridge sides in place. As a result, it is straightforward to design the double-ridge TEM antenna to match 50-Ω and 100-Ω system components. These plots were made with the electrostatic EM code called Electro (from Integrated Engineering).

Fig. 3 shows the unloaded version of the initial double-ridge antenna design. It was designed to be cut out of a single 0.5-in. thick sheet of Lexan plastic, and the conductors consist of copper strips and added copper tape. Fig. 4 shows the final, optimized antenna with a particular combination of lossy-foam loading material surrounding the aperture ends of the ridges. It should be noted that it took more effort to design the transition from the transverse 50-Ω SMA coaxial feed to the 50-Ω input point of the flared double-ridge antenna itself than it took to design the flared antenna. This is because the EM fields must be forced to make a dramatic change from transverse coaxial geometry to microstrip to parallel-plate to double-ridge geometry. In the process of iteratively designing the transition cross-section, we developed a fractional-width relationship with Atwater’s microstrip impedance formulation to quantify the effect of ridge height on surge impedance. The dimensions of the double-ridge input section are: ridge width = 0.5 in., ridge separation = 0.105 in., and ridge (side) height = 0.75 in. The characteristic impedance of this line was 49.9 Ω using Electro.

Fig. 5 is a side view of the optimized scale-model antenna. The exact mathematical taper for the inside edge and also the outside edge of the ridge is a quarter section of an ellipse. This elliptical taper was chosen over more-commonly used exponential tapers because it provides a complete flare to a perpendicular face at the aperture. This strong curvature provides the best diffraction radiation for a given size, yielding the best input match and radiation gain for a given size. Exponential tapers are often used in tapered slot antennas and waveguide horn antennas, and elliptical sections have been used for controlling the aperture diffraction of horn antennas. Even though a degree of freedom is lost with the elliptical curve (it is entirely determined by the feed and aperture endpoints) compared to a 3-parameter exponential curve, we believe that judicious choice of the overall antenna length and height will yield an elliptical taper with the best antenna properties. The equations for the elliptical tapers are given later in the report.

Fig. 6 shows the details of the ridge conductor sides for the final version of scale-model antenna. Fig. 7 provides the design of the middle layer of carbon-loaded absorber sheet, and Fig. 8 gives the details for the outer layers of absorber. In terms of antenna loading, several different types can be used. We chose carbon-loaded sheet foam absorber for this project because Sandia has an ample supply of comparable absorber. When doing frequency scaling, dimensions scale inversely as frequency. And it is critical that the absorber used in the scale model have the same loss characteristics as the absorber used in the VHF antennas will have. We had available a variety of LS sheets from Emerson & Cuming, and four different versions of loading were experimented with. The best version of loading utilized LS-22 type throughout the scale model. Heavier loading could have been used to improve the scale-model antenna performance further, but that wasn’t done. The absorber which Sandia has that is best for the final VHF antenna design is AN-77 sheet, 2-in. thick and 24-in. square. LS-22 has similar loss in the 1-3 GHz band that AN-77 has in the VHF band. So the best scale-model loading consisted of five layers of 0.5-in. thick LS-22 sheet, sandwiched around the aperture end of the ridges. Even more absorber was tried, but the improvement didn’t warrant the additional size and material necessary.

Fig. 9 shows the experimental setup in the UNM lab for doing this antenna work. A Tektronix CSA-803 sampling oscilloscope (on the left, closer to the antenna under test) and Hewlett-Packard 8719A vector network analyzer were the main instruments used.

Fig. 10 is a plot of the model-antenna surge impedance, based on a step TDR measurement of one of the antennas. Also shown (with square symbols) is the approximate surge impedance along the flared elliptical taper, based on a parallel-plate vee transmission line. These data were taken out of Sensor & Simulation Note 221. Note that the ridge impedance is indeed much lower than the parallel-plate geometry. The two triangle symbols are the impedances calculated using Electro. One symbol (at 0.5 axial location) corresponds to Fig. 1. The other is at the double-ridge feedpoint. We are surprised at the discrepancy between the TDR measurement and the electrostatic-code result midway through the antenna, and with limited time, were unable to determine the reason why.

After the step-TDR measurements were made of several antenna variations, another time-domain configuration was used to measure the input reflection for a scaled bipolar pulse. Fig. 11 shows the bipolar pulse (‘reference pulse’) we were able to cleanly generate that most resembles the high-power FWG pulse which will be driving the VHF system. It also shows the complicated waveform reflected from the antenna. This reflected wave is shown in larger scale in Fig. 12. The largest reflected features are from the input transition from SMA connector to 50-Ω double-ridge beginning of the antenna proper. A vertical line was placed in Fig. 12 to identify the separate antenna regions. The critical reflection is from the aperture tips of the ridges, and for this particular bipolar-pulse excitation, it had an amplitude of 5% of the incident peak value of the bipolar pulse. This is $20\ \log(0.05) = -26\ \mathrm{dB}$ relative to incident peak. This level of reflected current is fairly good, but not superb. It was very difficult to achieve better reduction of antenna ringing, especially at frequencies where the antenna length or height is so small electrically that it doesn’t radiate well.

After the bipolar time-domain input reflection measurement, we moved to vector analyzer measurements of the scale-model antennas. Fig. 13 shows the frequency-domain input match of the final version of antenna. The ‘entire antenna’ trace is the ungated swept-frequency input reflection coefficient, while the ‘time-gated aperture mismatch’ trace was generated by time-gating out the worst reflection, that of the input feed transition. See Fig. 14 for the corresponding time-domain bandpass response of the input match. This is dB versus equivalent time, and is computed internally in the network analyzer with an inverse FFT. There are two broad time impulse features – the reflection from the input feed transition (from –500 ps to about 1.2 ns), and the reflection from the aperture of the double-ridge antenna section (from 1.3 ns to about 2.3 ns). These correspond to the same regions shown in Fig. 12 for the bipolar pulse excitation. Then in Fig. 14, a time gate was used to eliminate the input transition mismatch feature; the gated trace in Fig. 13 results. It should be noted that the mismatch of the feed transition is at least 10 dB worse (higher) than the aperture reflection – look at the level of the two features in Fig. 14. Then note in Fig. 13 what effect the feed mismatch has on the overall antenna match – a -20 dB return loss for most of the band, compared to -30 dB return loss corresponding to the aperture reflection alone. This emphasizes the importance of clean transmission-line transitions in the antenna feed section. Now, because the high-power pulser connection is parallel-plate rather than coaxial, with a less severe field transition required, the aperture-gated reflection of Fig. 13 is the pertinent trace to consider. But because the receiving antenna will be just like the scale-model antenna in terms of feed design, the receiving antenna will probably have more ringing in it than the transmitting antenna will.

This aperture-gated input match is replotted in Fig. 15 for convenience in interpreting the relative level of match. The reflected wave from the antenna aperture back to the input of the antenna is at most about 3% above 1.3 GHz. So if this antenna were driven with a pulse whose spectral content was entirely above 1.3 GHz, then the resulting reflected wave would be at most 3% of the incident voltage level. Alternatively, if the antenna were driven with a pulse which had significant spectral content below 1.3 GHz, then a much larger reflected pulse would be generated. The low-frequency rolloff shown in Fig. 15 is universal for finite-sized antennas – as the frequency drops, the wavelength increases, and the electrical size of the antenna drops. The radiation efficiency drops as a result, as well as the input match deteriorating. This illustrates the classic fundamental antenna limit of antenna size versus frequency.

After the input match was examined with the four versions of absorber loading attempted, then the tx/rx bistatic side-by-side antenna configuration was put together. Fig. 16 shows the antenna pair (both with the same final loading version), with a center-center separation of 25 cm. The network analyzer was used in an S_{21} measurement mode to measure the mutual coupling between the two antennas. The isolation between them was measured as a function of antenna spacing (or separation), and it improves (the mutual coupling drops) as the spacing increases. Note that this is an H-plane array of two antennas – the other type of array would be an E-plane array, where the two antennas are coplanar with one another (one above the other). The H-plane array was the only case measured because it offers the most compact physical size for a given isolation level. An E-plane array would have been very tall as well – more difficult to field.

Even though it would have been useful to obtain direct time-domain mutual-coupling measurements for prediction of the VHF system performance, it was impossible. This isolation measurement could not be done with the bipolar time-domain system available because the signal amplitudes were far too small.

Then a variety of shielding arrangements were attempted, with an antenna spacing of 20 cm (center to center). This included different numbers of LS-22 absorber sheet layers, with and without sheet metal, different size shields, and shields in different positions. By comparing the mutual coupling (or isolation) for these configurations, we determined the dominant coupling mechanisms for the parallel antennas. The first coupling to occur in time is direct sideways radiation between the two feedpoints. Then as the tx current is traveling out along the antenna, the magnetic field expands and couples to the side of the other antenna. This direct-sideways coupling was directly reduced by the intervening shield – especically with metal. The second coupling to occur is when the main beam radiates out in front of the tx antenna, and diffracts around the front edge of the intervening shield, and is then picked up by the rx antenna. This front-edge diffraction was the most difficult to reduce, because most of the energy is radiated in the endfire/main-beam direction. The only way to improve that isolation was to extend the intervening shield out in front of the antenna apertures (and the farther it protrudes in front of the antennas, the better the isolation). The third coupling to occur is when the side radiation diffracts above and below the intervening shield. This was very effectively removed by adding a sheet of absorber above the antenna-shield-antenna structure, and also a sheet below it. The diffracted wave is then directly attenuated by the top and bottom absorber sheets.

Fig. 17 shows fairly complete shielding – but the top and bottom absorber sheets were not in place for that measurement. There is an intervening shield consisting of a sandwich of one 0.5-in. thick LS-22 sheet, sheet metal, and another LS-22 absorber sheet. This extended 10 cm in front of the antenna apertures, and went completely back behind the feedpoints. The most complex (and best) shielding arrangement was that shown in Fig. 17, plus a single sheet of LS-22 absorber both resting on top and sitting underneath the entire assembly. Fig. 18 shows the resulting isolation achieved, as well as the mutual coupling between unshielded antennas. This amount of isolation (better than 53 dB above 1 GHz) is impressive. EM fields want to propagate, and bistatic isolation is difficult to achieve because it requires strong control of wave propagation, including reflection, refraction, diffraction, and absorption. Fig. 19 provides the corresponding time-domain bandpass response for the isolation measurements of Fig. 18. Note that the worst feature on the 'best shielding' trace of Fig. 19 – the narrow peak at 2.8 ns – is the diffraction around the front edge of the intervening shield.

The last antenna measurements consisted of the bistatic tx/rx configuration and best shielding arrangement, with a flat-plate reference reflector set up in the main-beam direction. The goal was to measure the tx/rx antenna transfer function, using the reflected wave component off of the flat metal plate. Again, the network analyzer was necessary because the bipolar time-domain measurement system wasn't sensitive enough. Two values of antenna-aperture to flat-plate range were used – 60 cm and 80 cm. With the flat plate 60 cm in front of the antenna apertures, and the antennas parallel to each other and perpendicular to the plate, Fig. 20 shows the time-domain response of S_{21} between antenna ports. There is a time-gated response, centered on the specular bounce off of the plate. There is also earlier-time mutual coupling between the antennas (described above), and later-time multipath propagation features. The first of the two late-time peaks is a double bounce: the wave reflects off the plate, back to the front edge of the intervening shield, back to the flat plate, and into the rx antenna. The second of the two peaks is the double bounce between the plate and the aperture portion of the antennas. Based on the time-gated plate reflection, Fig. 21 shows the overall transfer function for this bistatic scale-model antenna system. The two items to note are that it increases with frequency (because the antenna gain increases with frequency, due to increasing electrical size), and that the overall level is between -30 & -45 dB. This transfer function represents the amplitude of the received voltage from the rx antenna, relative to the spectral content of the pulse used to excite the tx antenna.

Vector analyzer measurements were also made of individual antenna boresight gain in the same bistatic configuration, but using S_{11} in a monostatic mode. These data may be used for antenna gain calculations or bistatic antenna pattern measurements. Time was too limited to report this data though. It should be noted though that the bistatic $S_{21}(f)$ is about 5 dB lower than the monostatic $S_{11}(f)$ because of the specular-bounce angle being off boresight due to the parallel antenna geometry. Thus, the 5-dB drop is due to both the tx pattern and rx pattern rolloff from main-beam/boresight direction of each antenna.

Frequency-Scaled Antenna Design

After the extensive experiments were performed in empirically developing a pair of scale-model antennas, the resulting performance parameters were scaled down in frequency for corresponding designs in the VHF frequency range. The goal is to derive good designs for both the transmitting and receiving antennas for use as part of the high-power GPR system for detecting buried drums.

Fig. 22 shows the high-power bipolar pulse of Sandia's frozen-wave generator (FWG), design #3, measured on 4/19/99. Overlaid is a frequency-scaled version of the low-power bipolar pulse used to examine the input reflection characteristics of the individual scale-model antennas. The actual low-power bipolar pulse had a spectral peak at 1.37 GHz, which was designed to be just above the 1-GHz lower end of the scale-model operating band of 1-3 GHz. This was done to simulate the difficult operating condition of driving the scale-model double-ridge antenna with a wideband low-frequency excitation – the worst combination in terms of input match, ringing, or bistatic isolation. In Fig. 22, the scale pulse was shifted down a factor of 8.7. And the spectrum of both the high-power FWG pulse and the downshifted scale-model pulse is given in Fig.23. The scale factor of 8.7 provides the best spectral fit, as well as the most symmetrical tails of the bipolar time-domain pulses (note that it is faster on the leading tail, and slower on the trailing tail). As a result, Figs. 11 and 12 provide the most direct prediction of VHF antenna reflection performance when driven with the FWG pulse if the model antenna is scaled up in size exactly a factor of 8.7. Thus, we expect a transmitting antenna reflection of about 5% peak when driven with the FWG pulse, and the antenna is 8.7 times larger than the model antenna.

Fig. 24 shows the critical electrical antenna parameters frequency scaled by the same factor of 8.7. The gated-aperture input match is given, the bistatic tx/rx isolation (with best shielding) is given, as well as the gated bistatic tx/rx transfer function from the flat-plate reflection. Compare the trend in each parameter with the spectral content of the FWG pulse – this gives an indication of the predicted aggregate behavior of the VHF transmitting antenna if scaled up in size 8.7.

And as an aid in determining the actual size of the VHF antennas (both tx and rx), these antenna parameters were scaled by three different factors: 7.0, 8.0, and 9.0. In terms of physical dimensions, look at Fig. 5 again. The overall size of the scale-model antenna is as follows: length (from double-ridge 50-Ω input to front face of absorber blocks) = 23 cm (9.0 in.), height (from bottom of bottom absorber block to top of top absorber block) = 32 cm (12.6 in.), and width (of each absorber block) = 2.5 in. And for the bistatic H-plane configuration, the overall width of the antenna pair is 10.4 in. (from outside to outside of each absorber block). The integral feed transition from transverse SMA 50-Ω coax to 50-Ω double-ridge beginning of the antenna proper is 2.0 in. long. So the receiving antenna length is 11.0 in. total. By multiplying these dimensions by the frequency-scale factor, the following VHF antenna sizes result:

Frequency-Scale Ratio	Overall Length	Overall Height	Antenna Width	Overall Tx/ Rx Width
9.0	99 in.(8.3 ft)	113 in.(9.5 ft)	22.5 in.	94 in.(7.8 ft)
8.7	96 in.(8.0 ft)	110 in.(9.1 ft)	21.8 in.	91 in.(7.5 ft)
8.0	88 in.(7.3 ft)	101 in.(8.4 ft)	20.0 in.	83 in.(6.9 ft)
7.0	77 in.(6.4 ft)	88 in.(7.4 ft)	17.5 in.	73 in.(6.1 ft)

Fig. 25 shows the aperture-gated input match (voltage reflection coefficient) for these scale factors, as well as the spectrum of the FWG pulse. The overall reflected wave coming back to the pulser will have a spectrum computed by multiplying the input pulse spectrum and this reflection coefficient. Even though there doesn't seem to be much difference between these three traces, note that for the smaller antennas (x7 or x8 rather than x9), more of the FWG pulse spectrum is reflected back to the pulser. In other words, with the larger scale factor (the larger the VHF antenna), the better the input match relative to the excitation pulse spectrum. If smaller size is really critical, we have to live with more ringing in the antenna. If cleaner late-time ringdown is critical, we have to use a larger antenna.

Fig. 26 shows the other two critical parameters, for the bistatic tx/rx configuration. One is the tx/rx antenna transfer function. This represents the overall system sensitivity, from the spectral content of the tx pulser to the spectral content of the received target waveform. Note that the ground attenuation, and target scattering transfer function (as described in the earlier report) must be added (if working in dB) to this antenna transfer function in order to predict or estimate the overall received-signal sensitivity for the target echo coming out of the ground. As the scale factor increases (larger VHF antenna), the tranfer function shifts down more, effectively increasing the antenna transfer function in the passband of the FWG pulse spectrum. This increases the maximum depth of penetration, and improves the receiver ratio of target signal to mutual coupling between tx & rx antennas. Lastly, note that the flat-plate reflection was measured at a range of 60 cm (23.6 in., about 2 ft.) between the front face of the double-ridge aperture and the plate reflector, so the equivalent VHF range to the plate would be about 14 ft. for a scale factor of 7.0, 16 ft. for a factor of 8.0, or 18 ft. for a factor of 9.0. The expected height of the antenna system above the ground for the planned high-power GPR outdoor field experiments is 10 ft. As a result, the tx/rx bistatic antenna transfer function will increase due to the shorter range than that from the model antenna results. So the actual tx/rx transfer function at VHF will be stronger than that shown in Fig. 26.

The other parameter is the tx/rx antenna isolation. As the scale factor increases, the isolation curve shifts lower, also effectively improving the isolation. This behaves like the input match – that is, the larger the antenna, the better the isolation performance. Now, in Fig. 26, we define a crossover frequency, above which the tx/rx antenna transfer function is greater than the tx/rx antenna isolation. The difference between the two represents the usable dynamic range of the GPR system if time-domain gating of the receiver (oscilloscope) is not employed. There will always be a time separation between the antenna mutual coupling and the reflected wave off the surface of the ground, as well as additional time down to the buried drum and back out. This well-defined time lag will be a direct way to identify buried drums using received waveforms.

Limited project time precluded the next step in this analysis – multiplying the FWG pulse spectrum by appropriately processed portions of these three parameters, and then inverse transforming to get the predicted time-domain responses for the high-power GPR system. The earlier buried-drum calculations could also then be combined with this antenna characterization to provide a complete pulser-to-receiver estimation of the received target echos.

The conclusion for this antenna analysis is that the electrical performance improves with size. The larger we build the VHF antenna pair, the better the resulting radar performance will be. And it should be noted that because the AN-77 sheet absorber has an aggregate loading which isn’t quite as lossy in the VHF band as the LS-22 is in the scale-model antenna band, it may very well be necessary to use thicker amounts of AN-77 than the directly-scaled dimensions would indicate.

In terms of the tx/rx antenna isolation shielding, there are several guidelines as well. The more absorber, the better. The best shielding is to surround each antenna in a metal ‘box’ which is lined with absorber. Thus, for the proposed H-plane pair array, there would basically be an intervening shield wall, with top and bottom walls at a minimum. The intervening shield wall should extend in front of the antenna apertures at least as much as the scale factor times the amount used in the model measurements (10 cm, or 4 in.). Each face of the intervening wall should be lined with absorber, as well as the interior side of the top and bottom walls. The absorber should overlap the edges of the metal shield plates by a few inches to reduce ringing and reflections from the shield plates themselves.

For the 100-Ω parallel-plate transmitting antenna feed, a gradual transition to double-ridge line should be made. See the sketch of Fig. 27. And to reduce useless current flow inside the ridges themselves, this transition should be packed with absorber inside the ridges. The actual dimensions of the 100-Ω section of line can be determined by several iterative runs of Electro.

The actual elliptical tapers (directly for the 50-Ω rx antenna, and modified for the 100-Ω tx antenna as needed for physical connection to the FWG pulser) are straightforward to compute. Use the scale factor desired to scale up these two ridge tapers. For the scale-model antennas, the ridge outline is plotted in Fig. 28. The equation for the upper inside ridge edge is:

$$x_{in}(z) = x_i + \left(x_a - x_i\right)\left(1 - \sqrt{1 - \left(\frac{z}{z_a}\right)^2}\right), \text{ for } z = 0 - z_a,$$

where x_i is the input half-height (0.1335 cm), x_a is the aperture half-height (12 cm), and z_a is the axial length (20 cm). Note that all you need are the input separation (divided by 2), the length, and the aperture height (divided by 2). The lower inside ridge edge is the negative of this curve. And the elliptical-taper equation for the outside ridge edge is:

$$x_{out}(z) = x_1 + \left(x_a - x_1\right)\left(1 - \sqrt{1 - \left(\frac{z}{z_1}\right)^2}\right), \text{ for } z = 0 - z_1,$$

where x_1 is the input half-height (2.0385 cm), and z_1 is the axial length of the outside edge. Here, we intuitively chose z_1 to be 65% of z_a (13 cm). This was based on some prior tapered slot antenna work in the literature, and isn't considered critical; if z_1 is 50% of z_a, the plate width at the aperture top is unnecessarily wide, whereas if z_1 is 75% of z_a, the ridge width will be a bit too narrow for well-distributed fields in the antenna (which may decrease the tx gain). Then the equations for the actual VHF antennas will be multiplied by the frequency scale factor discussed above.

In conclusion, we have experimentally developed a pair of scale-model antennas for optimum performance with the given requirements for this GPR system. By appropriately scaling up their size, the VHF antenna pair should operate in a very similar manner. The only additional design issue besides the size scaling issue are the details necessary in designing the input transitions for the transmitting antenna and the receiving antenna.

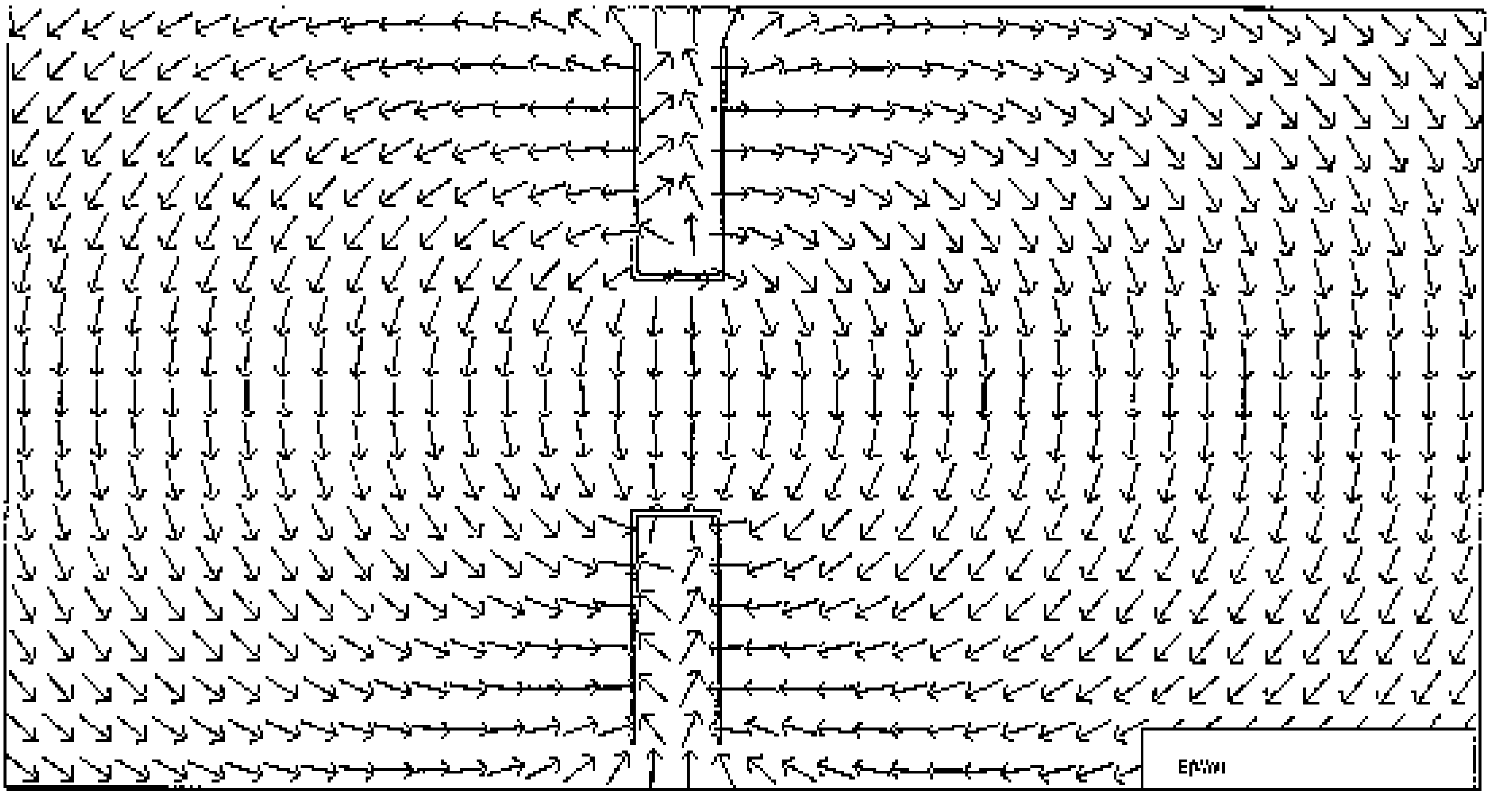

Analysis mode: ELECTRO 2D Field. Analysis type: Dielectric Analysis
E-Field arrows / Impedance = 179 Ohms =
Symbol file: C:\ESVEBWINELE4D\JAurend5-99_run11.dbs DATE = Jul. 14, 1999 TIME= 15:40:27.00

run11: w = 0.5 in
d = 1.2 in
h = 1.2 in

$Z_o \approx 179\,\Omega$

Halfway out in horn.

Fig. 1- E-Field Distribution of Double-Ridge Section Halfway Out in Antenna.

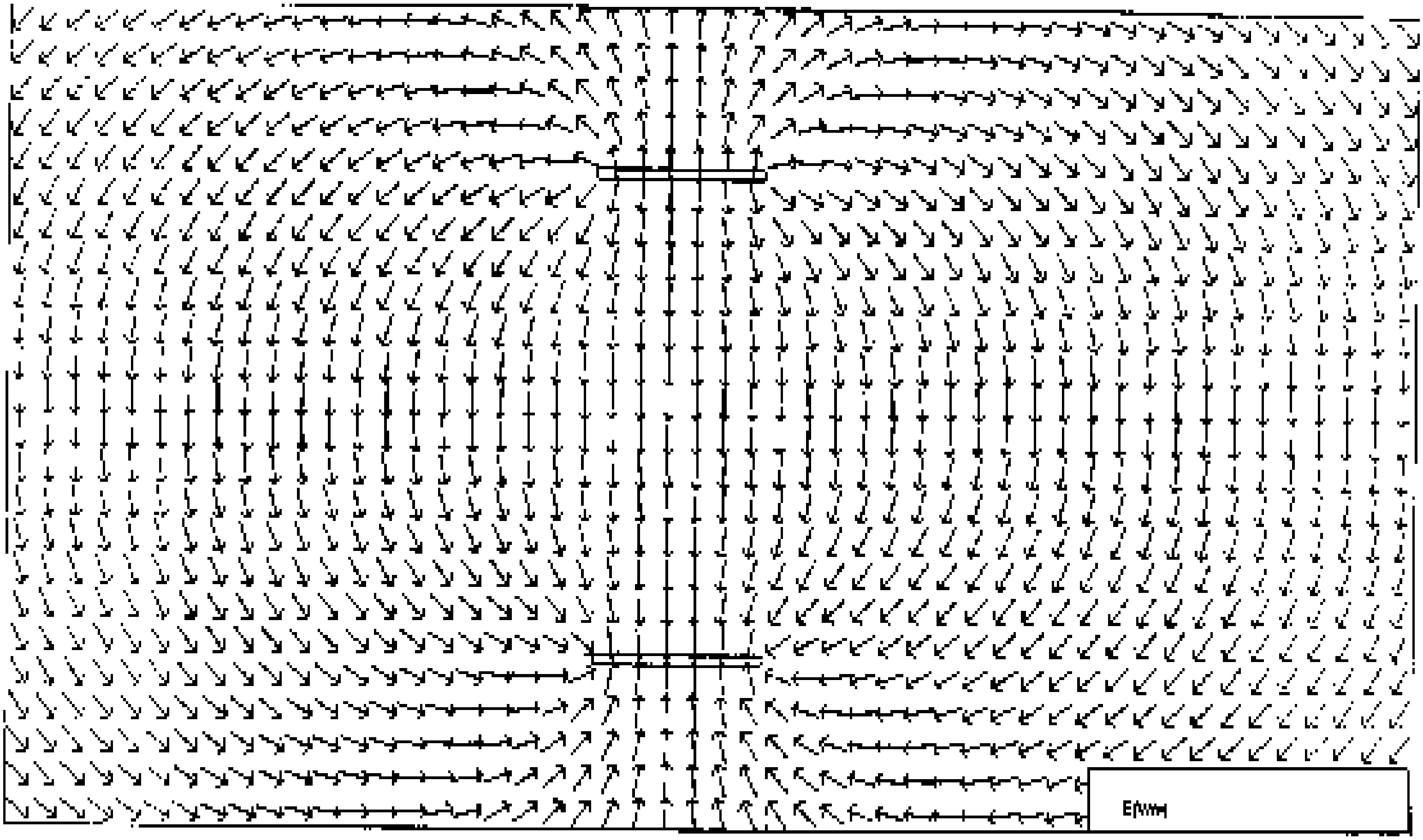

Analysis mode: ELECTRO 2D Field. Analysis type: Dielectric Analysis
E-Field arrows / Impedance = 264.9 Ohms
Current file: C:\[illegible]\VANELEAD\JAurand4-ss_run13.dsv DATE = Jul. 14 1999 TIME= 15:29 36.00

Emit: w = 0.5 in

δ = 1.2 in

Parallel Plate

Z_o = 264.9 Ω

Fig. 2- E-Field Distribution of Comparable Parallel-Plate Section.

This Page Intentionally Left Blank

Fig. 3- Unloaded Initial Design of Double-Ridge Antenna.

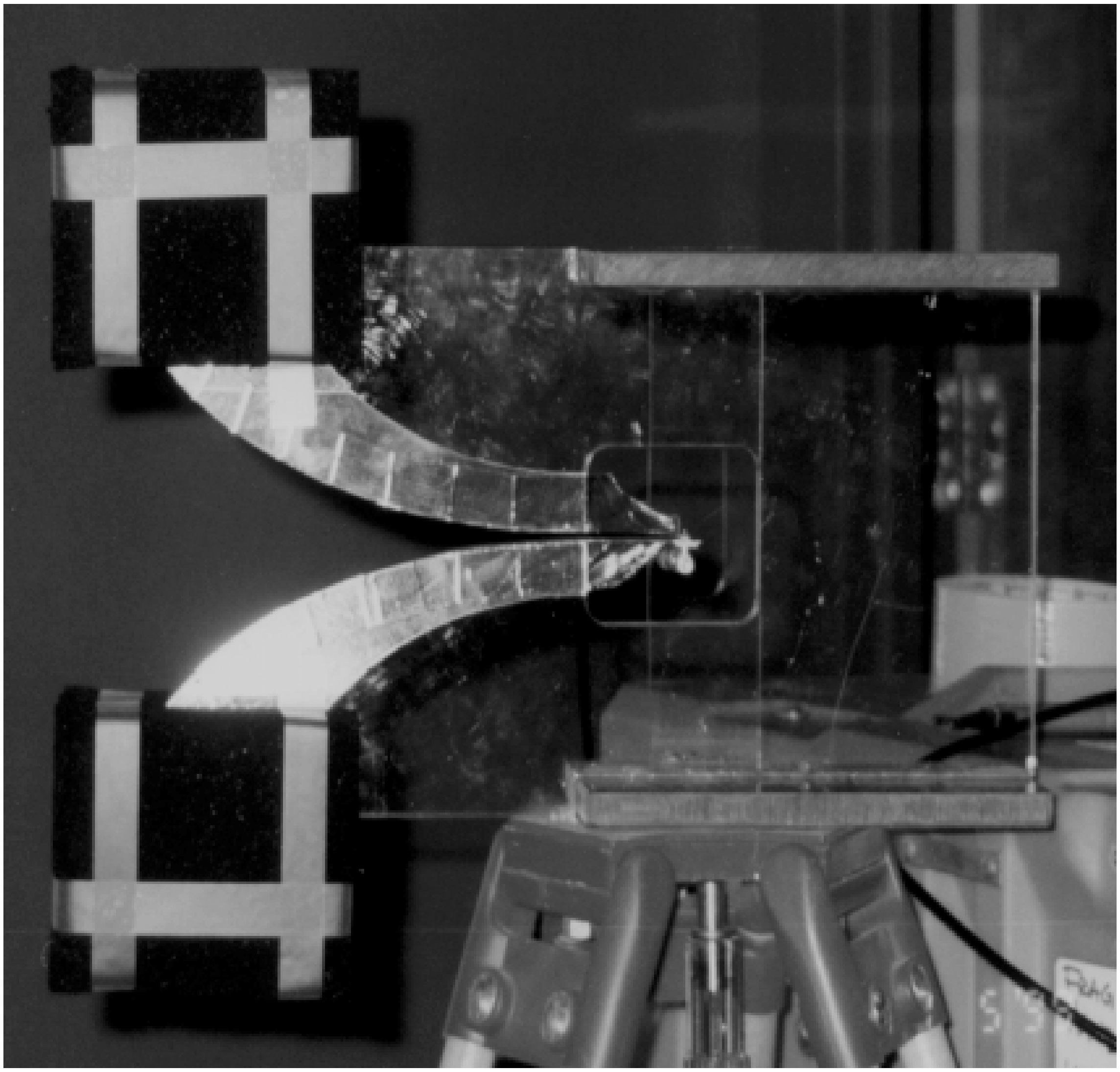

Fig. 4- Final Design of Double-Ridge Antenna.

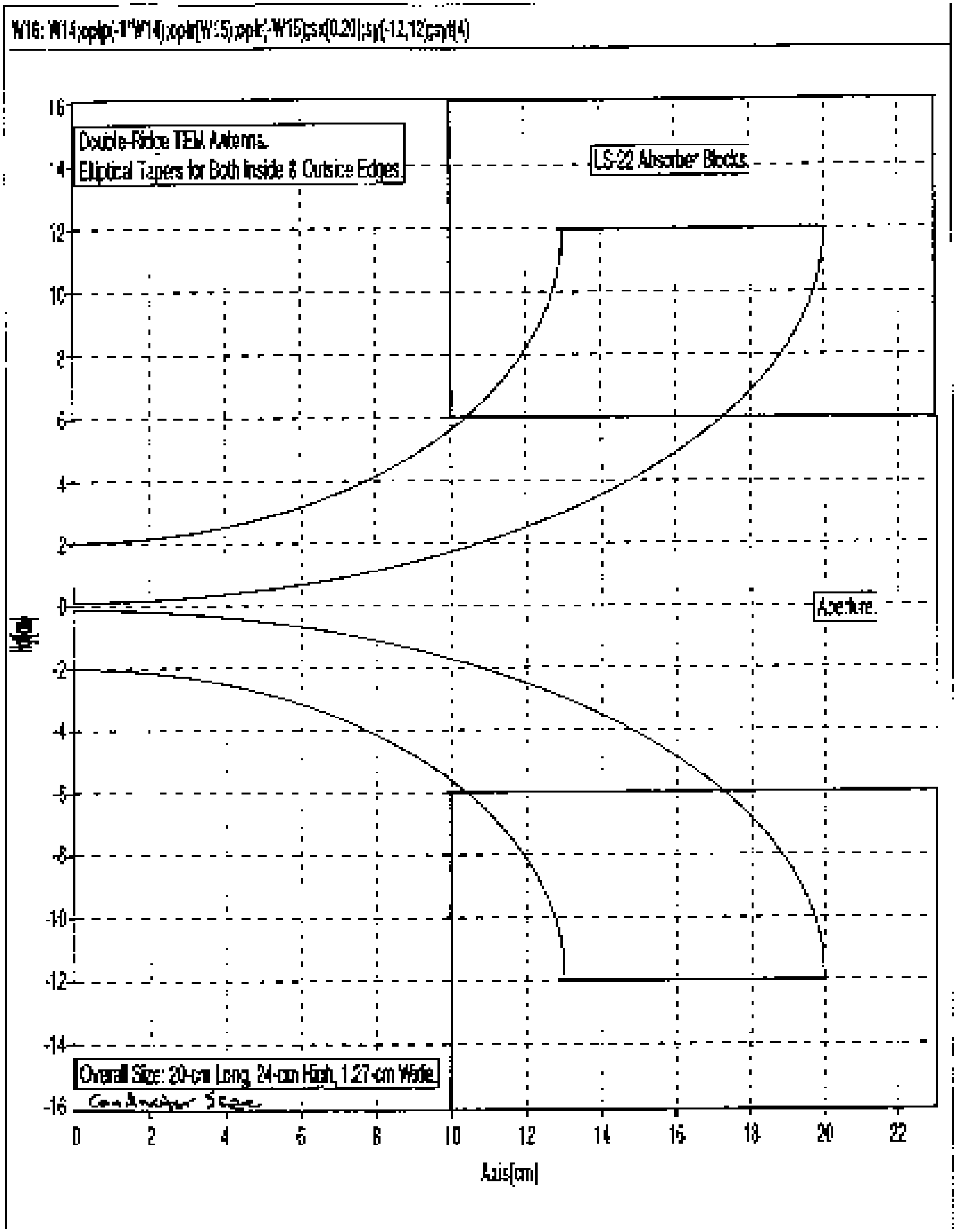

Fig. 5- Layout of Final Scale-Model Double-Ridge Antenna.

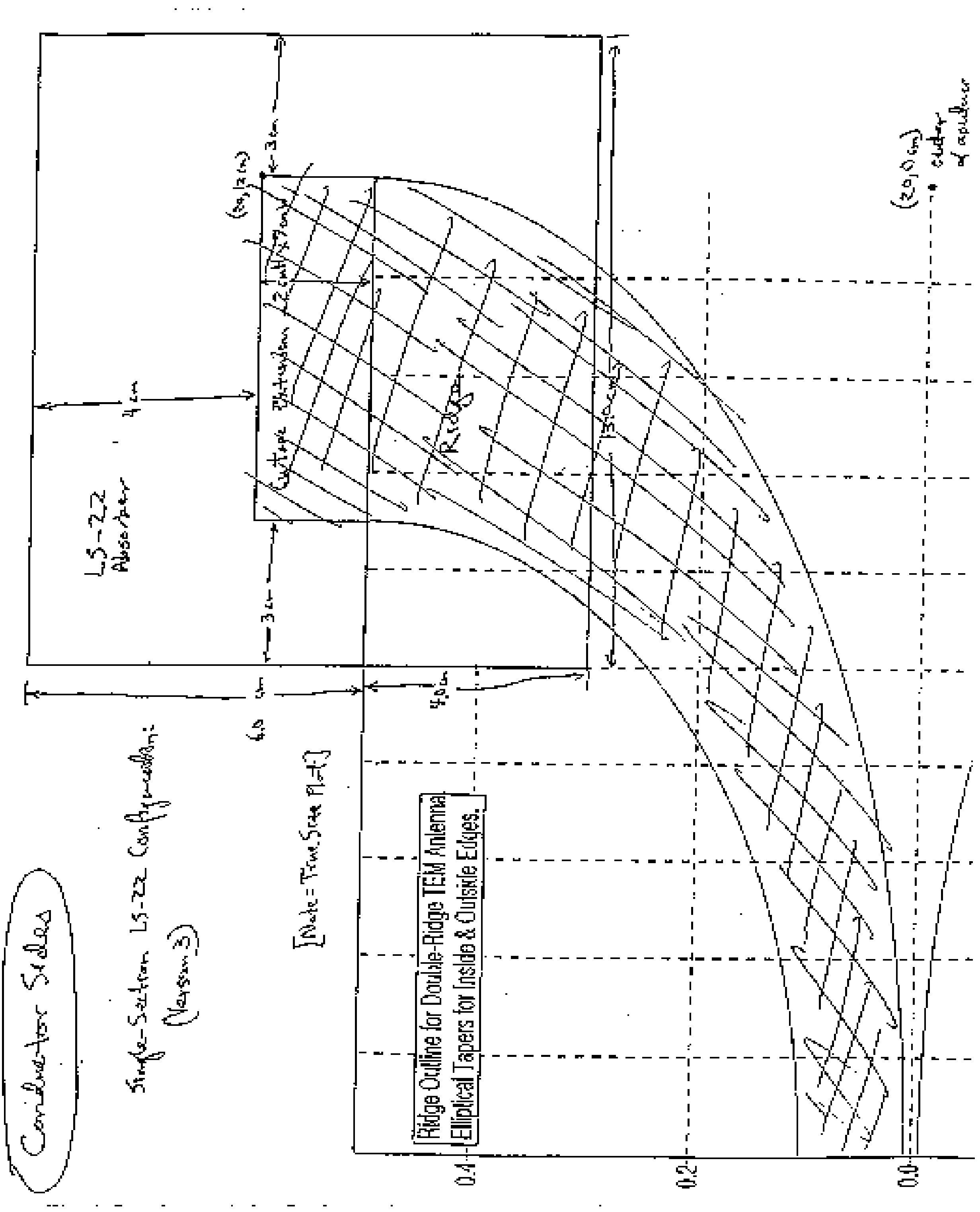

Fig. 6- Detail of the Ridge Conductors for the Scale-Model Double-Ridge Antenna.

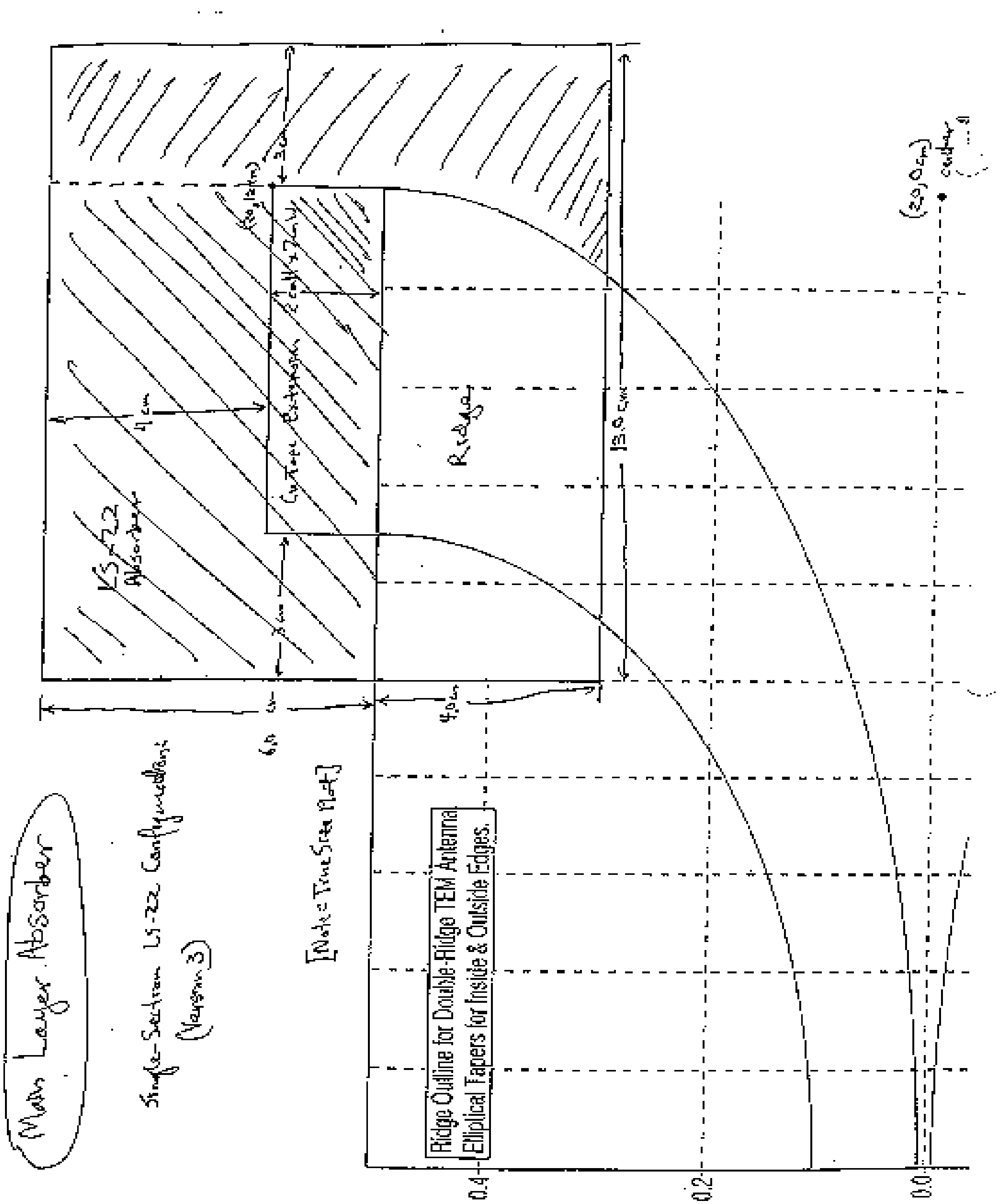

Fig. 7- Detail of the Middle Absorber Layer in the Scale-Model Antenna.

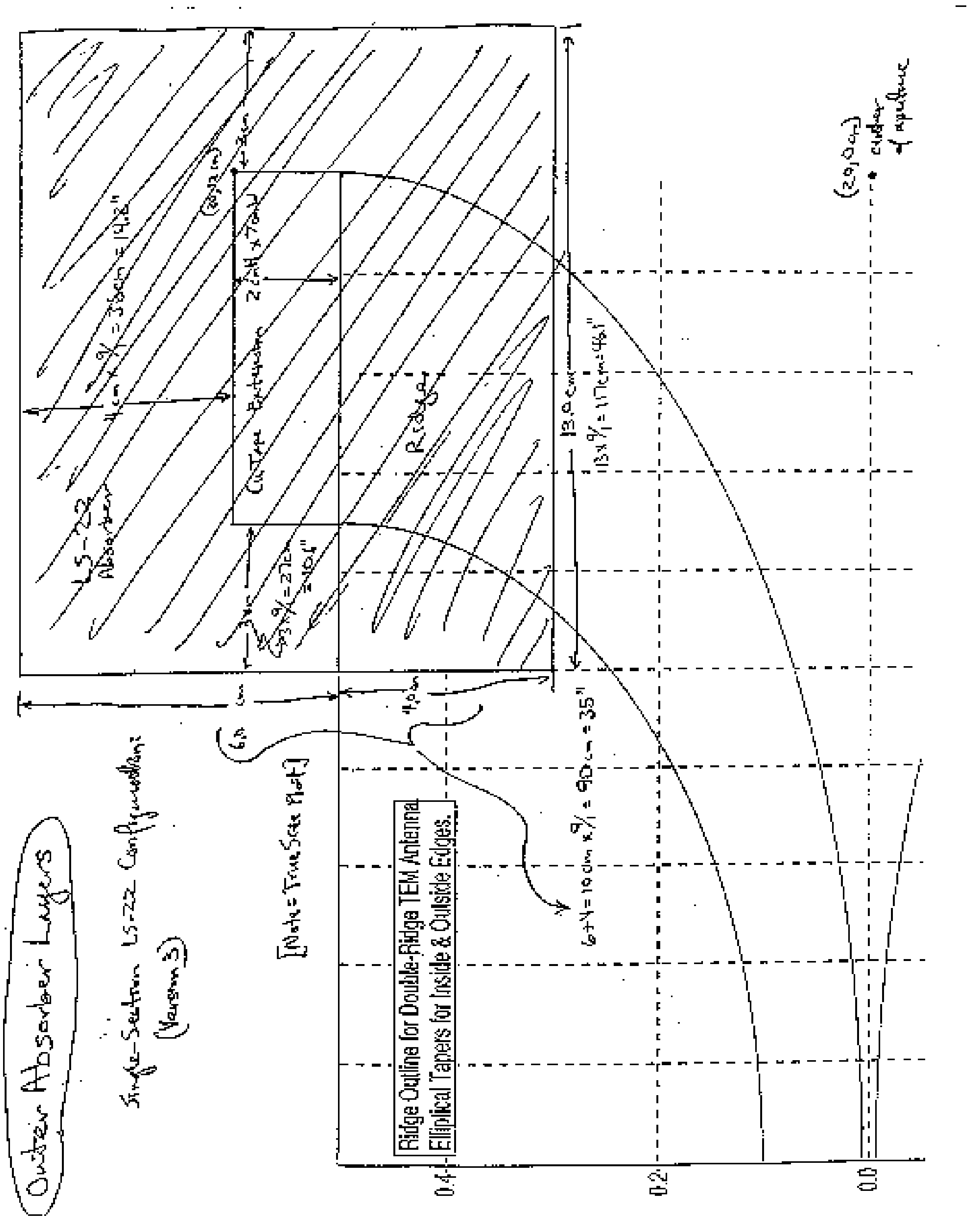

Fig. 8- Detail of the Side Absorber Layers for the Scale-Model Antenna.

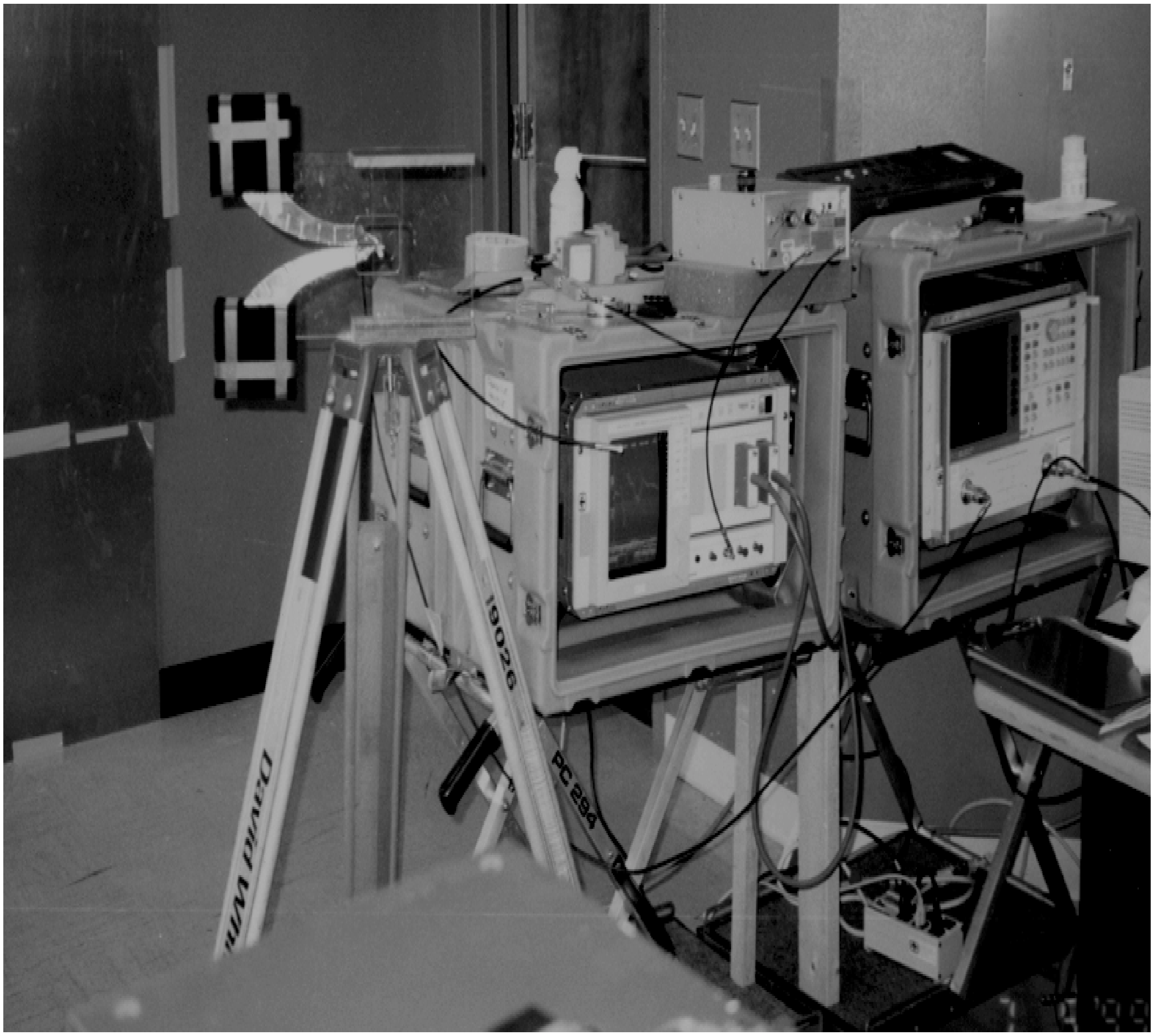

Fig. 9- Experimental Setup for Scale-Model Antenna Measurements.

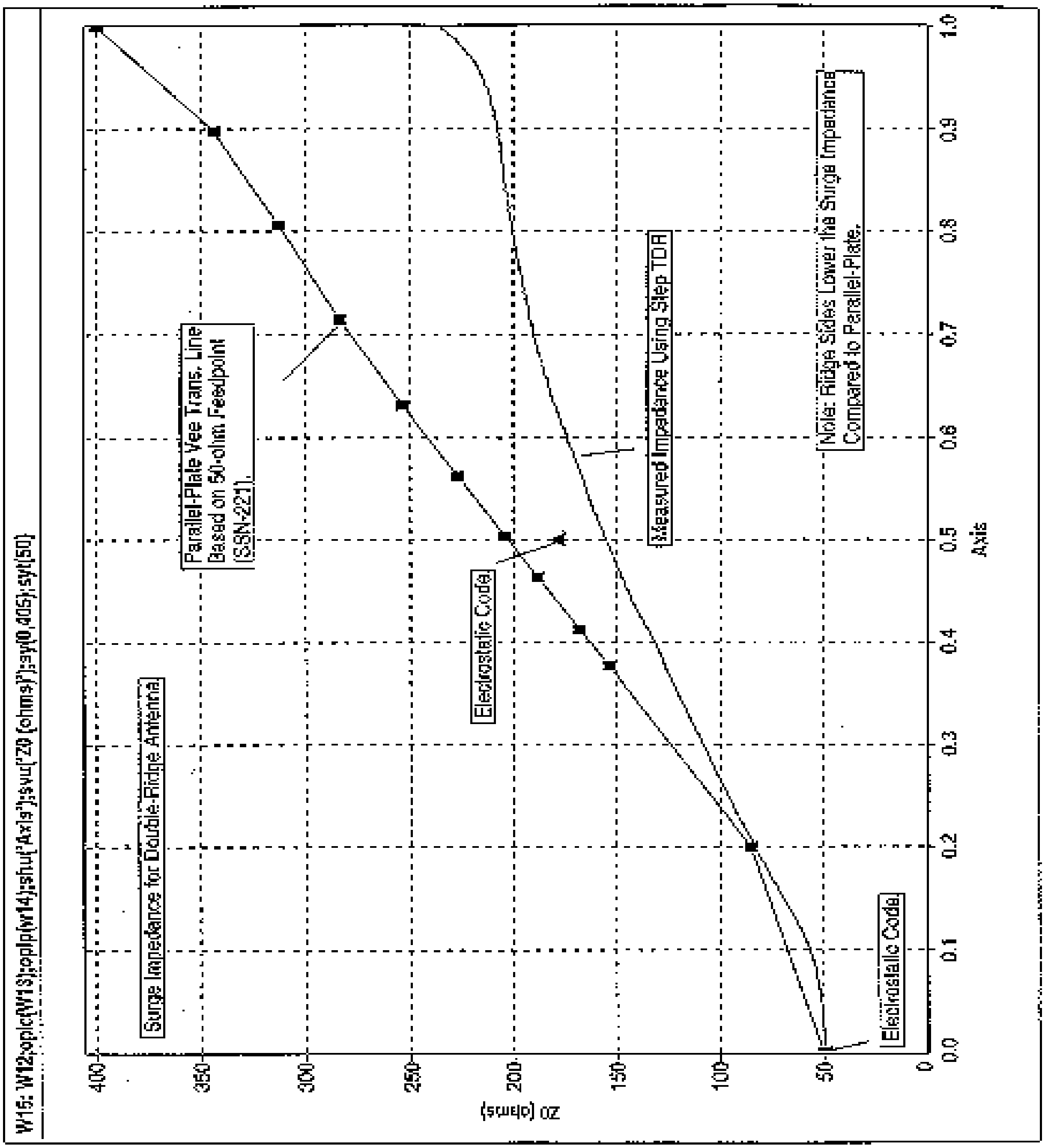

Fig. 10- Step-TDR Surge Impedance of Double-Ridge Antenna.

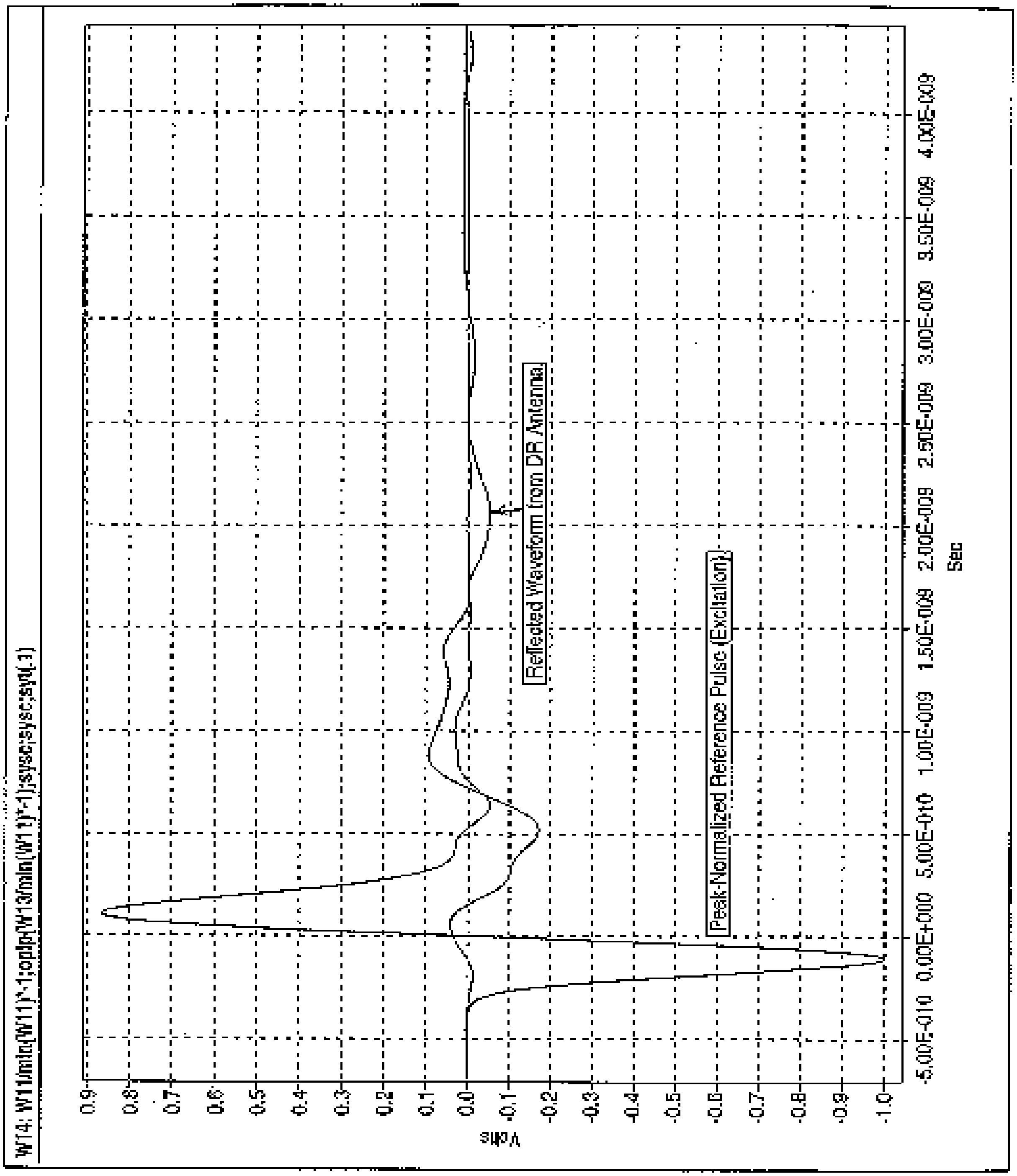

Fig. 11- Input Reflection Measurement Using Bipolar Pulse.

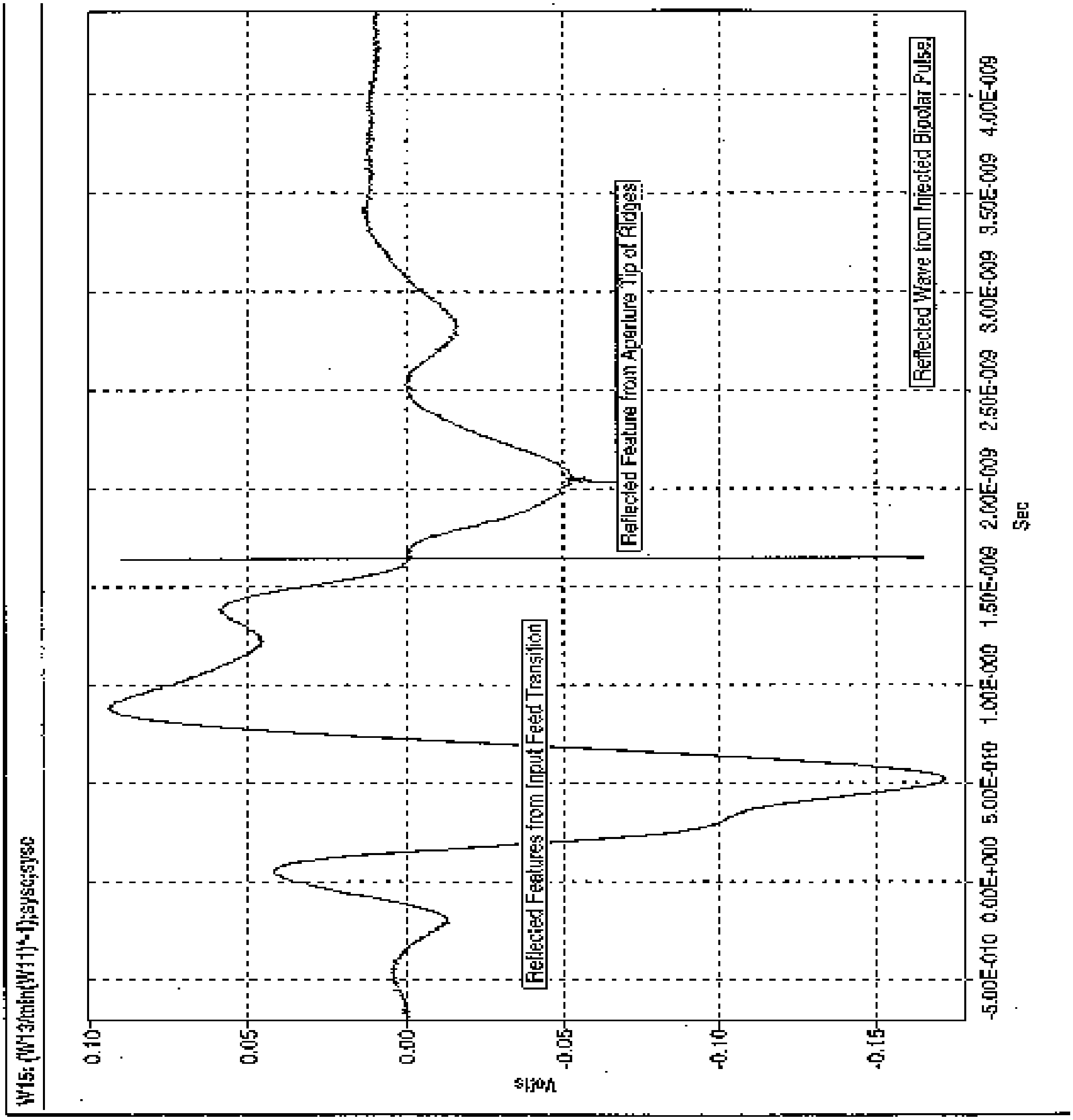

Fig. 12- Expanded View of Reflected Wave from Scale-Model Antenna.

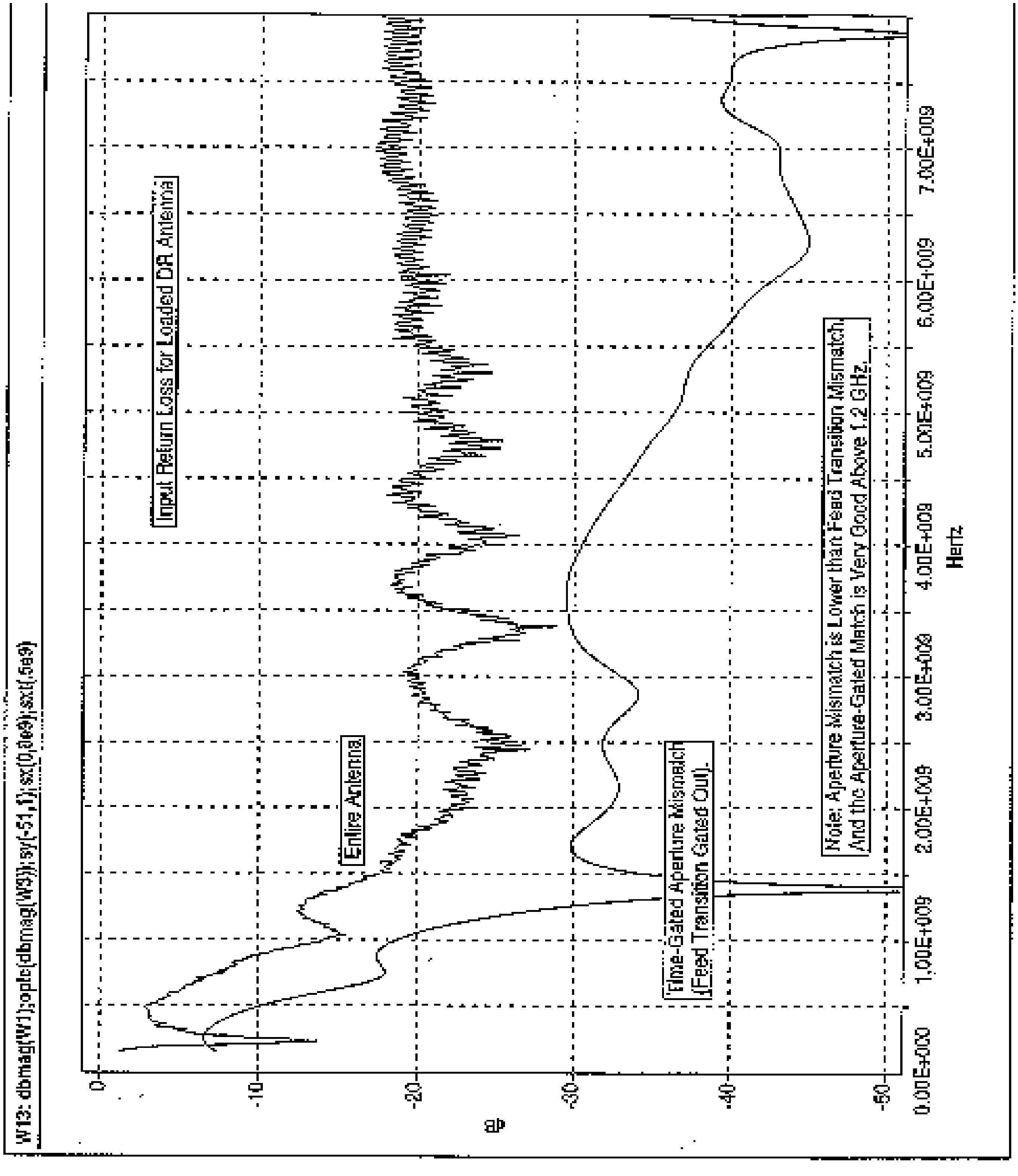

Fig. 13-Input Match of Scale-Model Antenna Using Vector Analyzer.

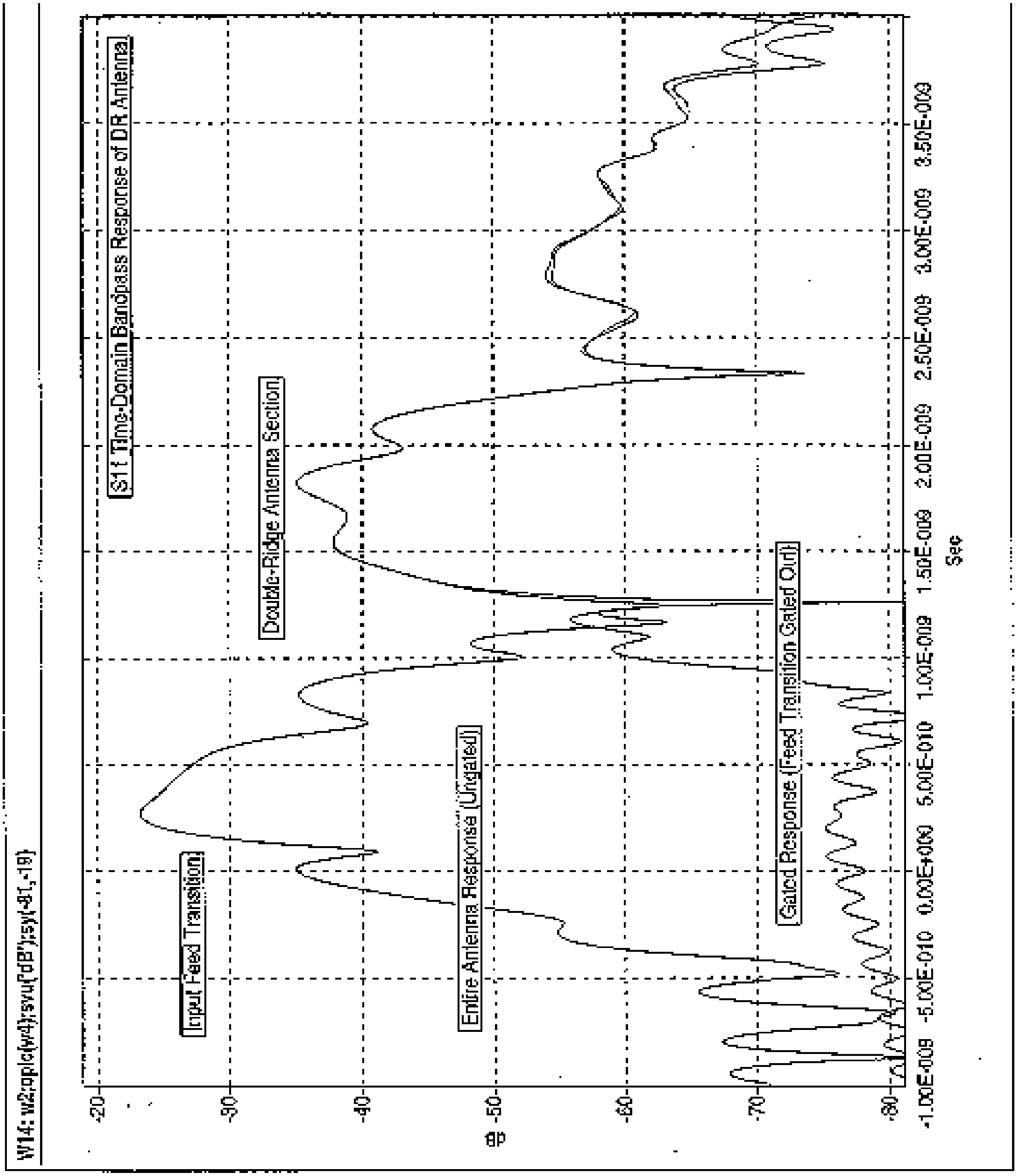

Fig. 14- Time-domain Bandpass Response of Input Match.

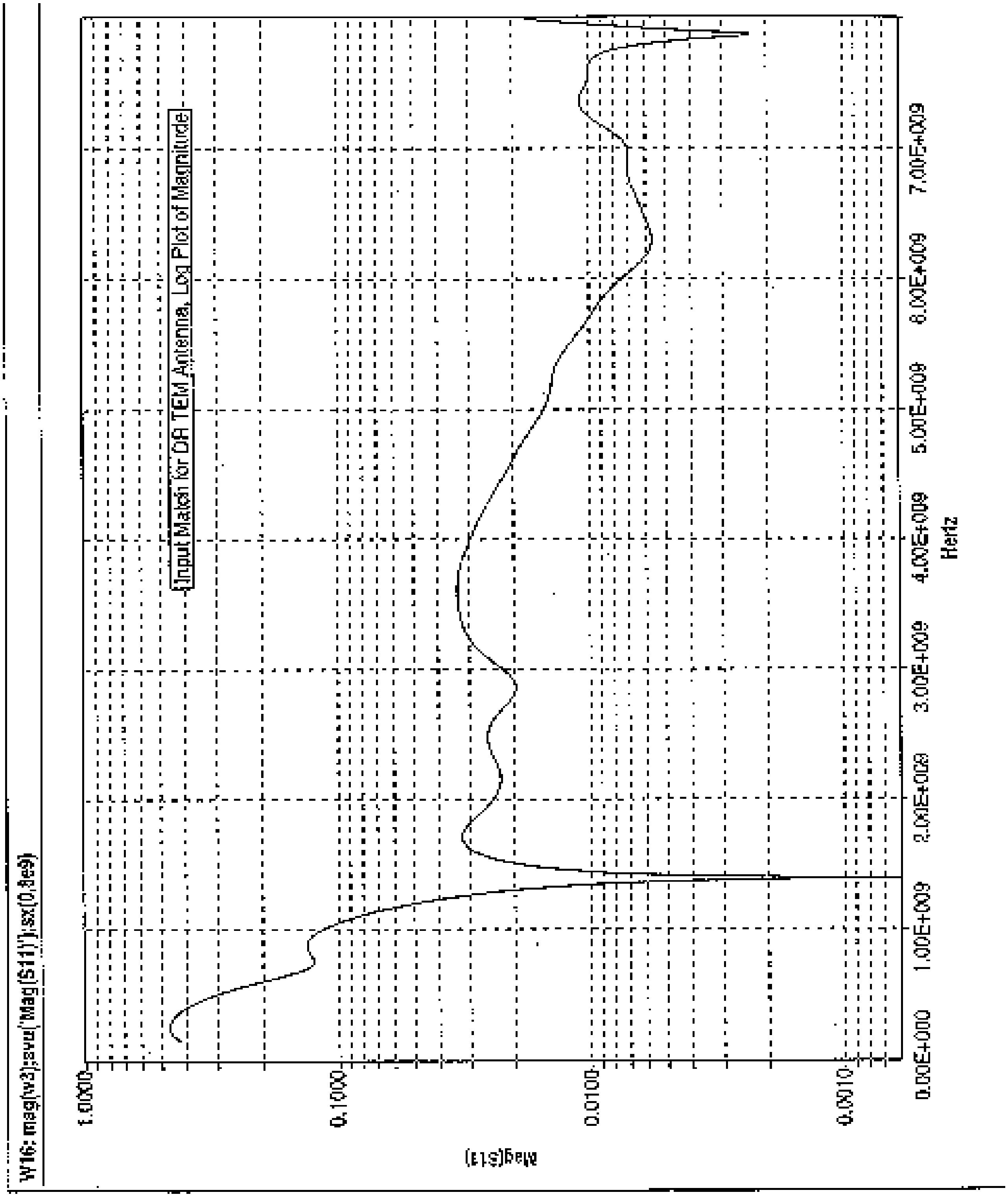

Fig. 15- Alternative Plot of Gated Input Match of Scale-Model Antenna.

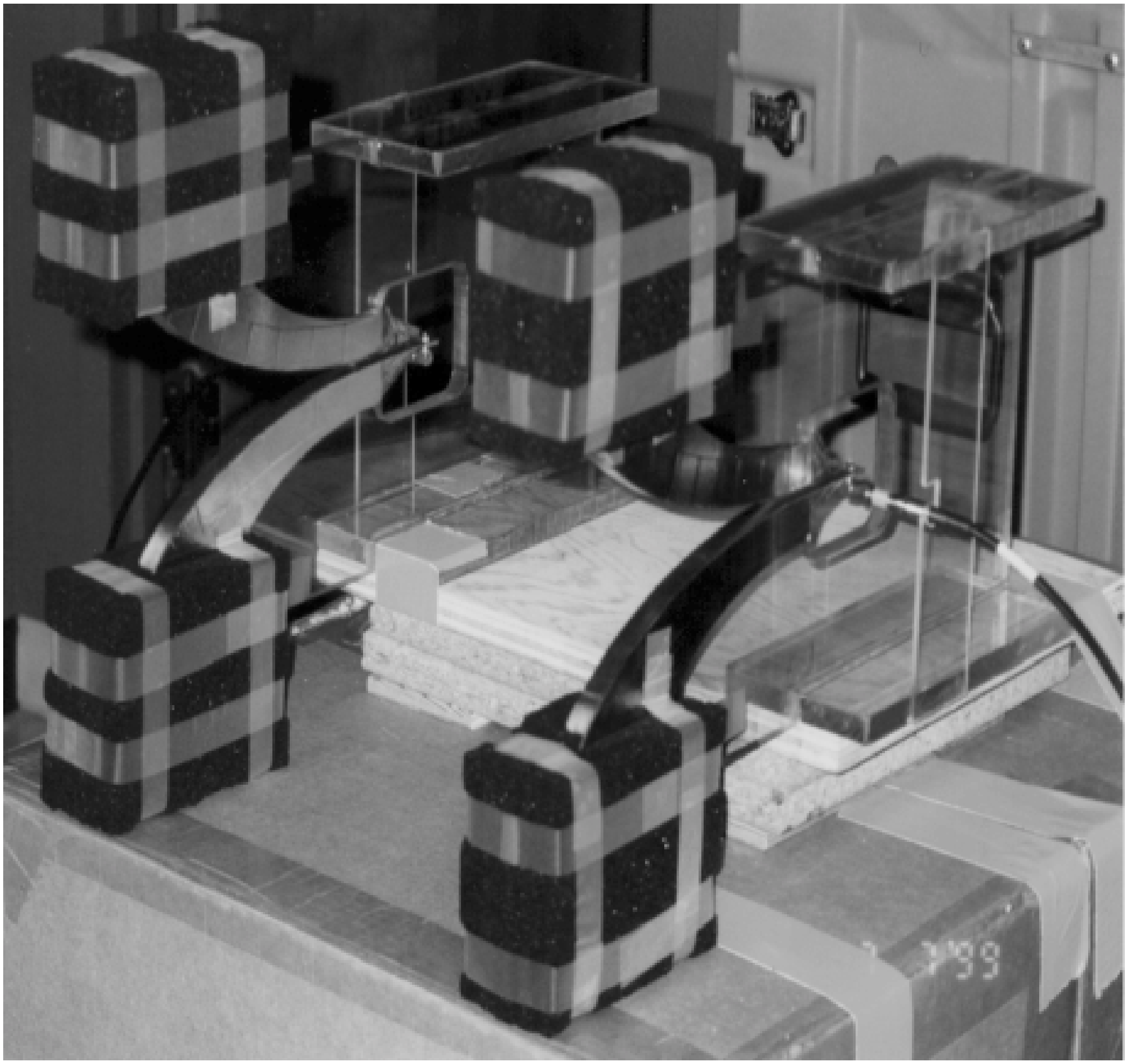

Fig. 16- Bistatic Antenna Setup, Separation = 25 cm.

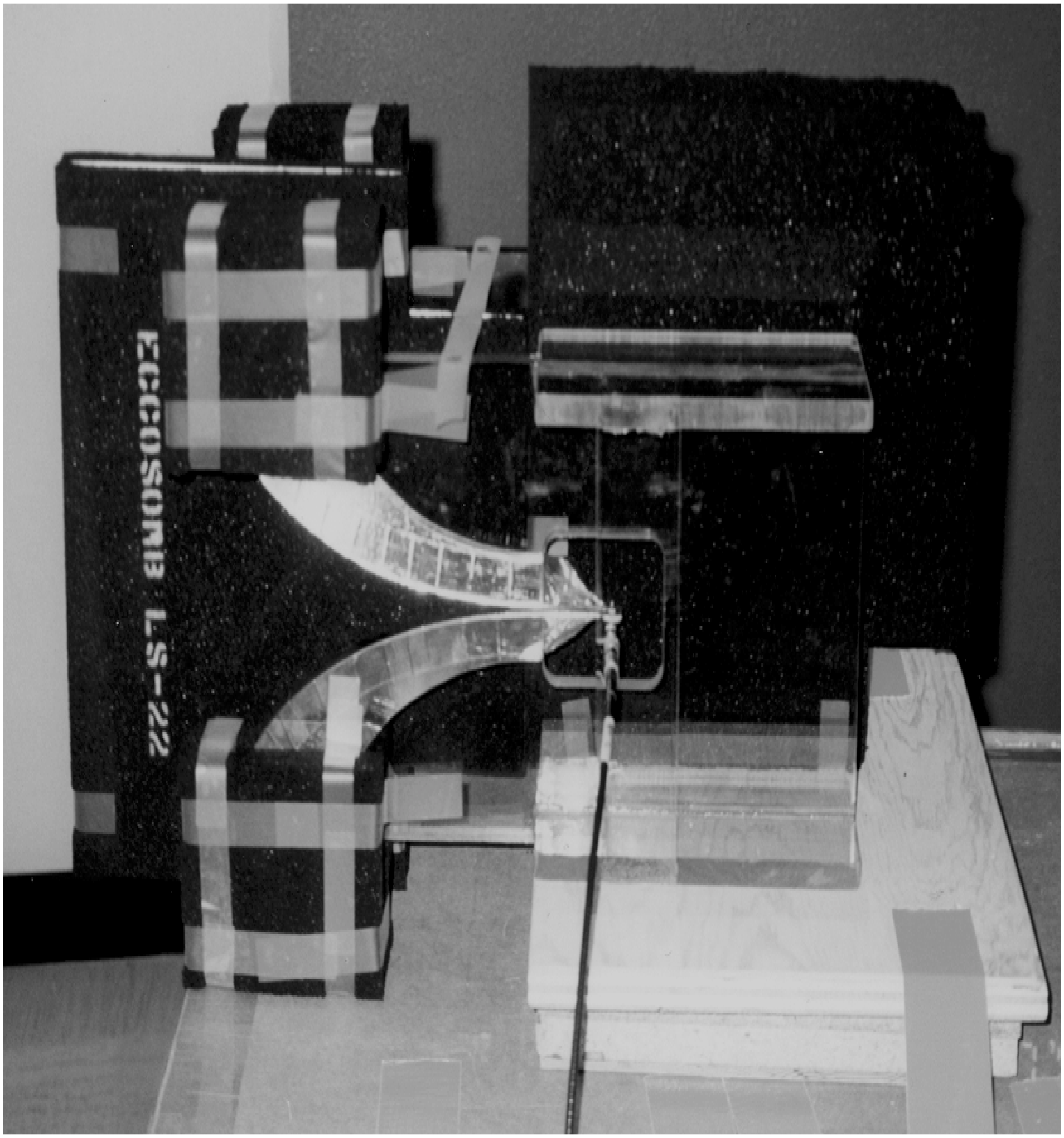

Fig. 17- Almost-Complete Shielding of Bistatic Configuration (Missing Top & Bottom Absorber Sheets).

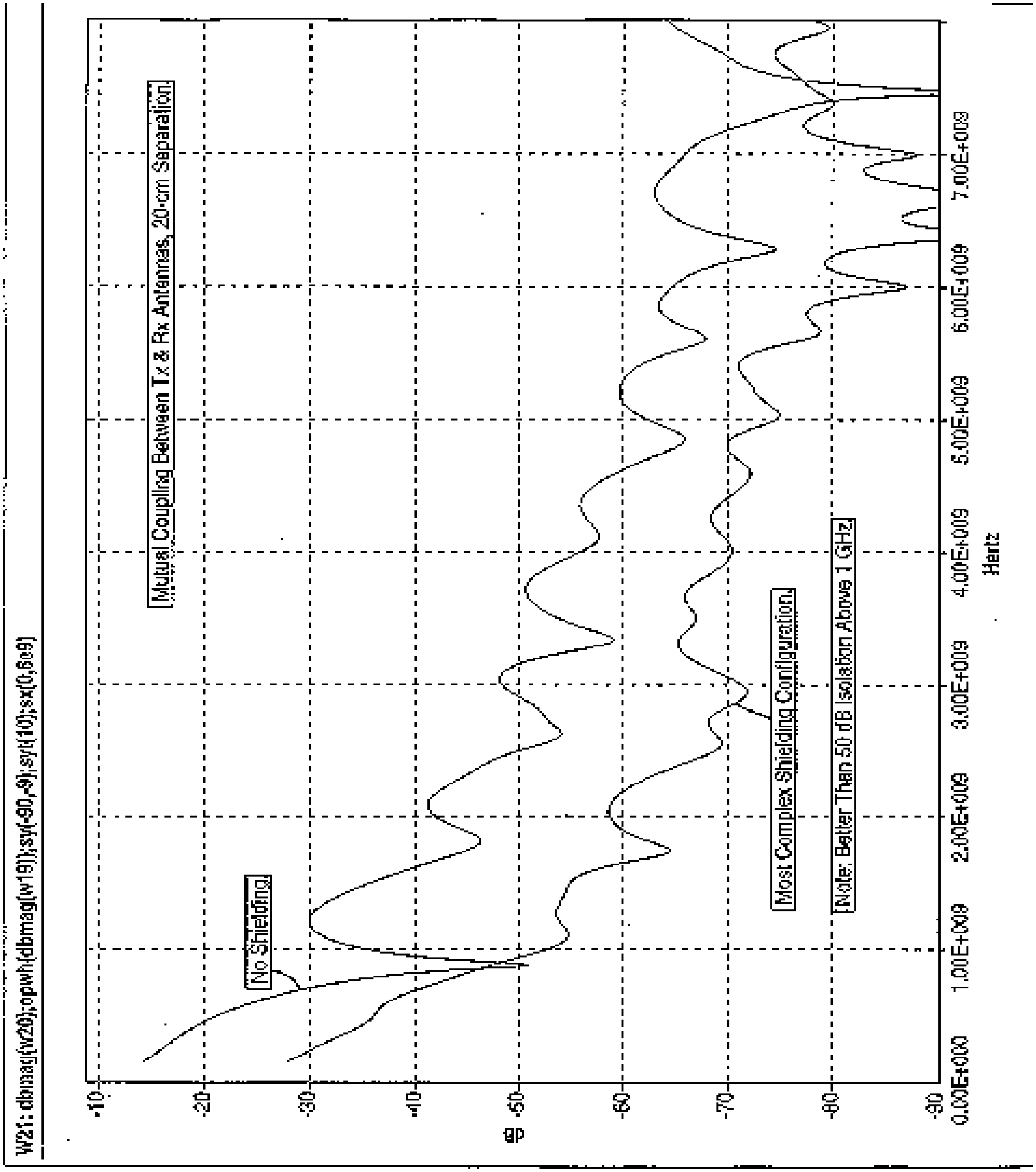

Fig. 18- Mutual Coupling Between Antennas with Best Case Isolation.

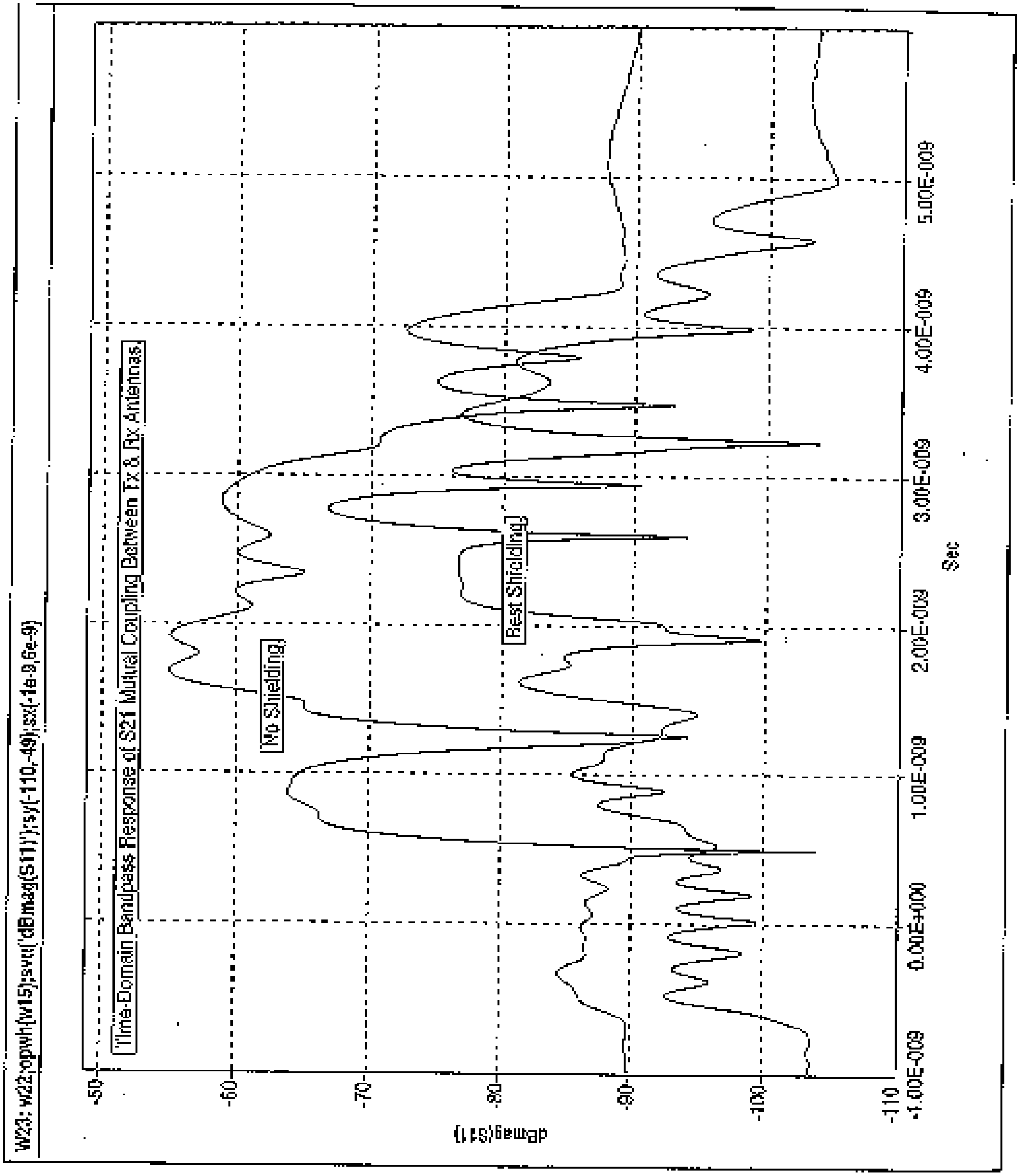

Fig. 19- Time-domain Bandpass Response of Mutual Coupling Between Antennas.

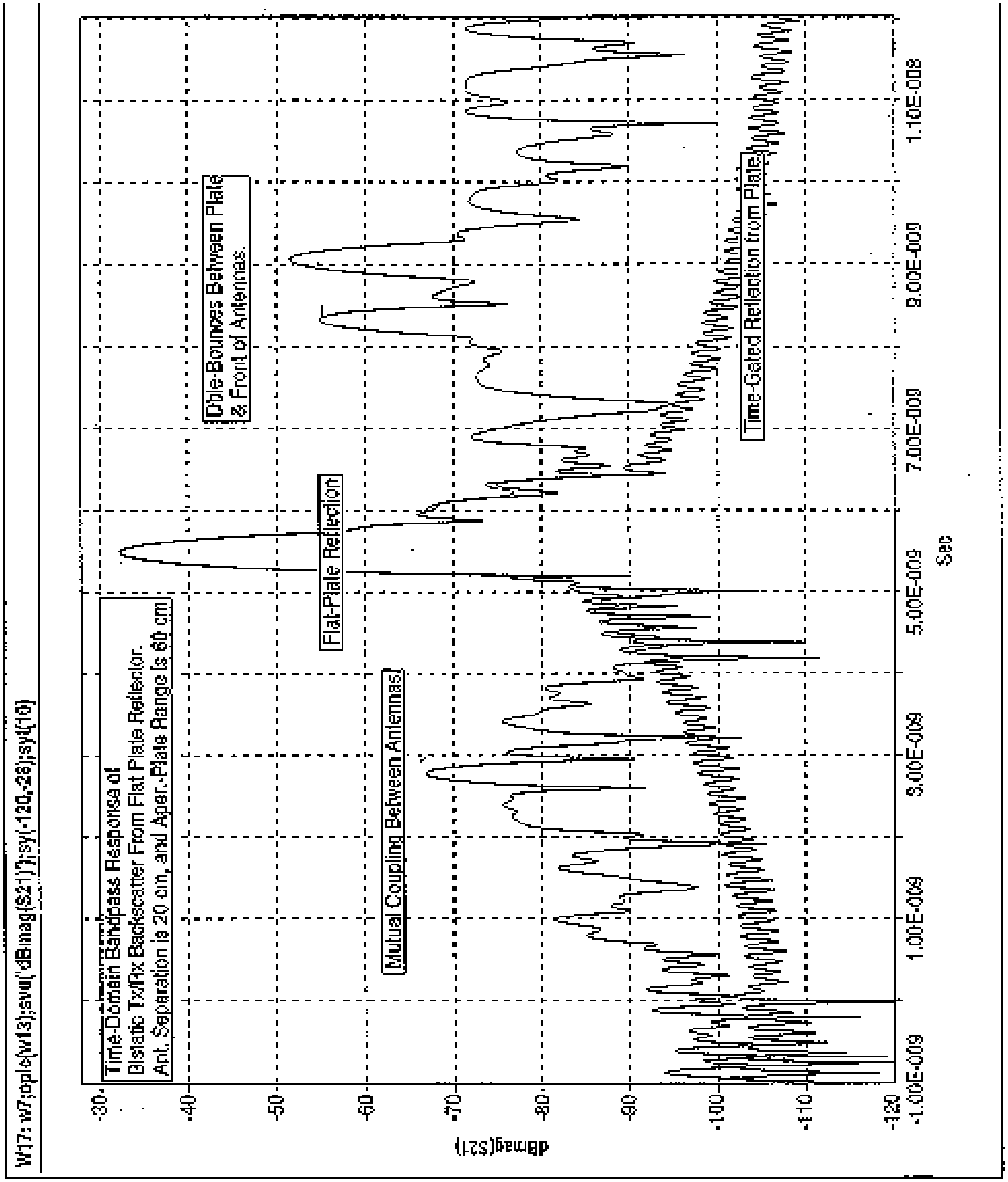

Fig. 20- Time-domain Bandpass Response of Bistatic Flat-Plate Reflection.

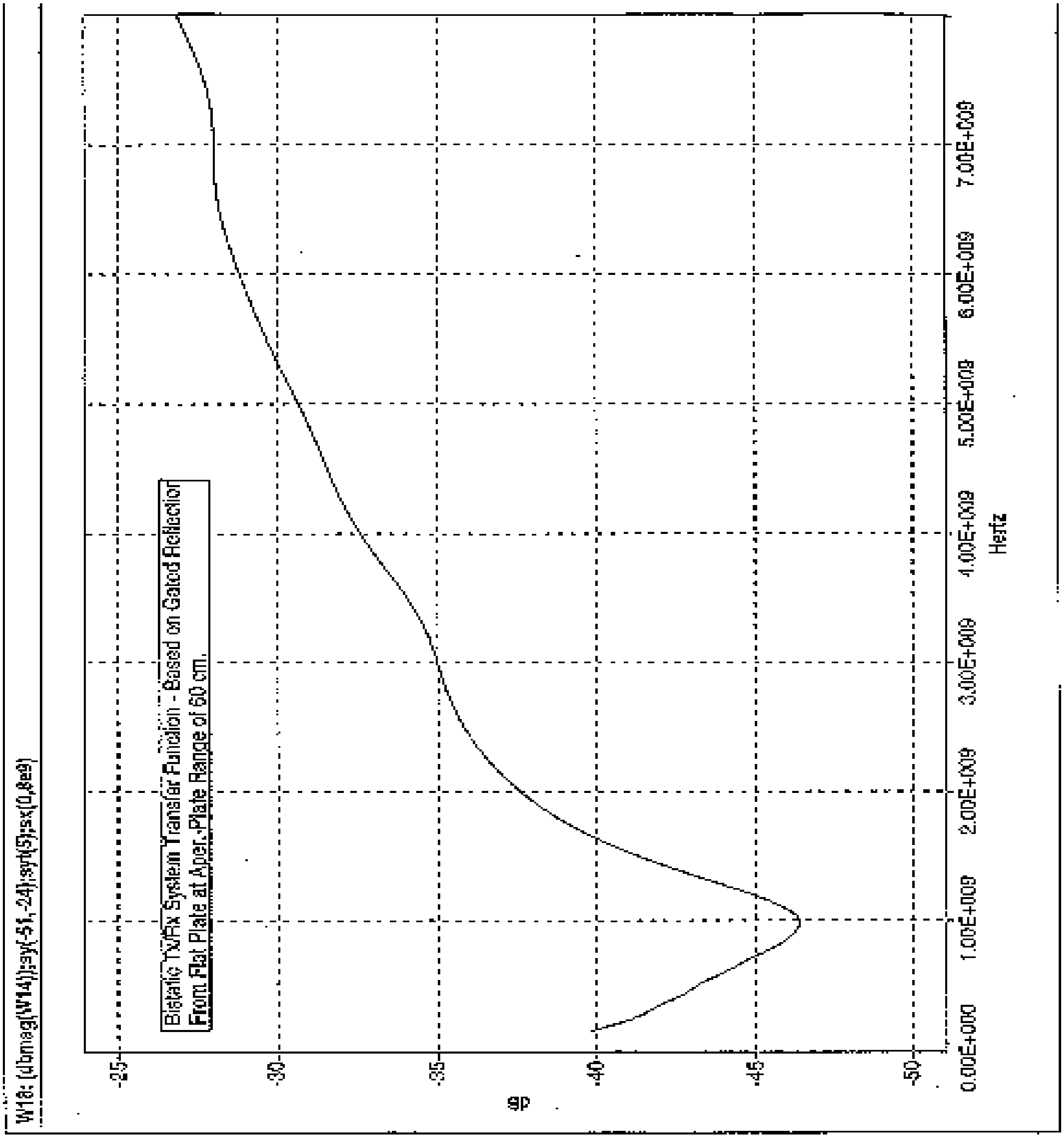

Fig. 21-Bistatic Tx/Rx Antenna Tranfer Function from Flat-Plate Reflection.

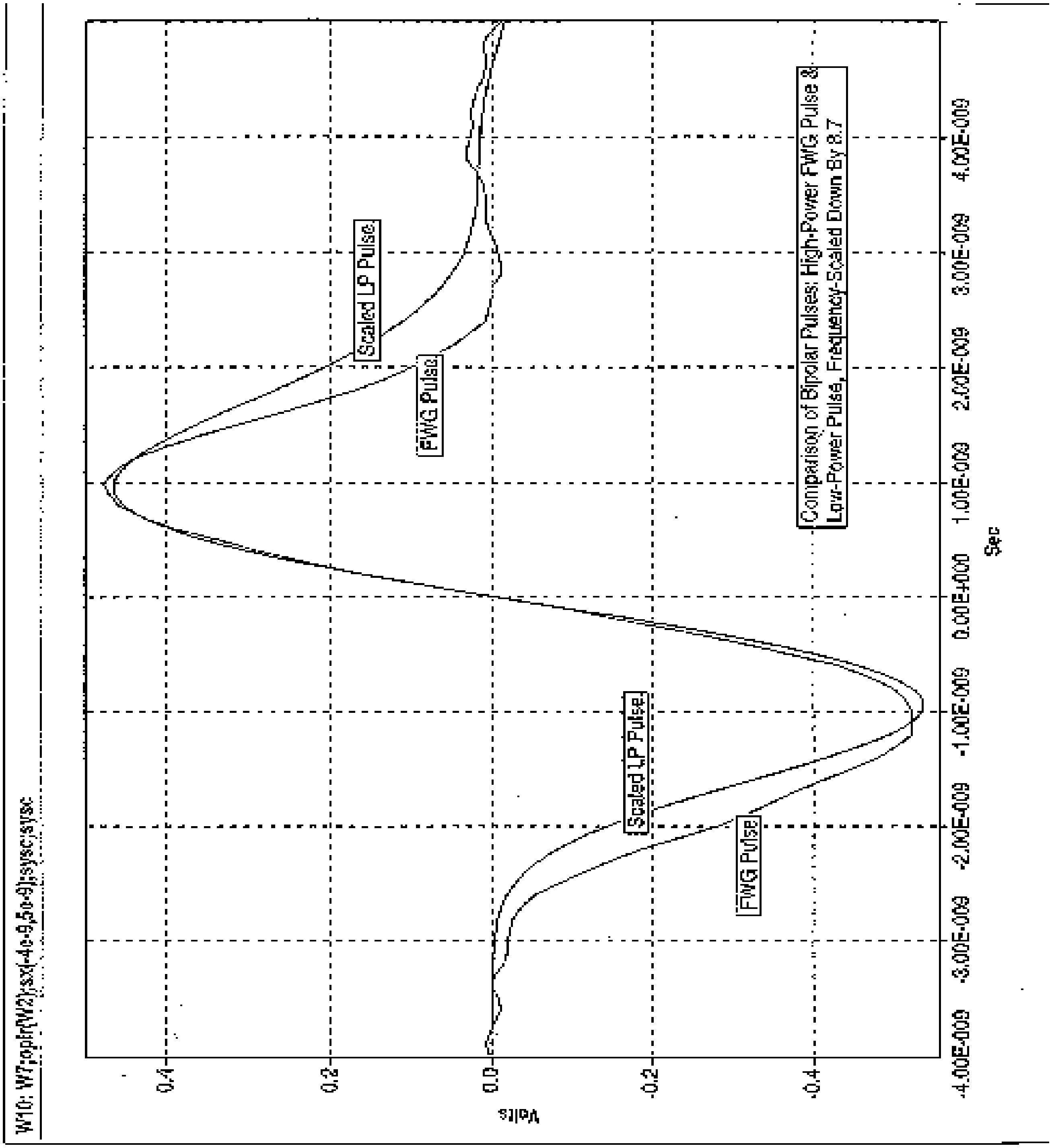

Fig. 22- Comparison of Scaled Bipolar Pulse and High-Power Pulse.

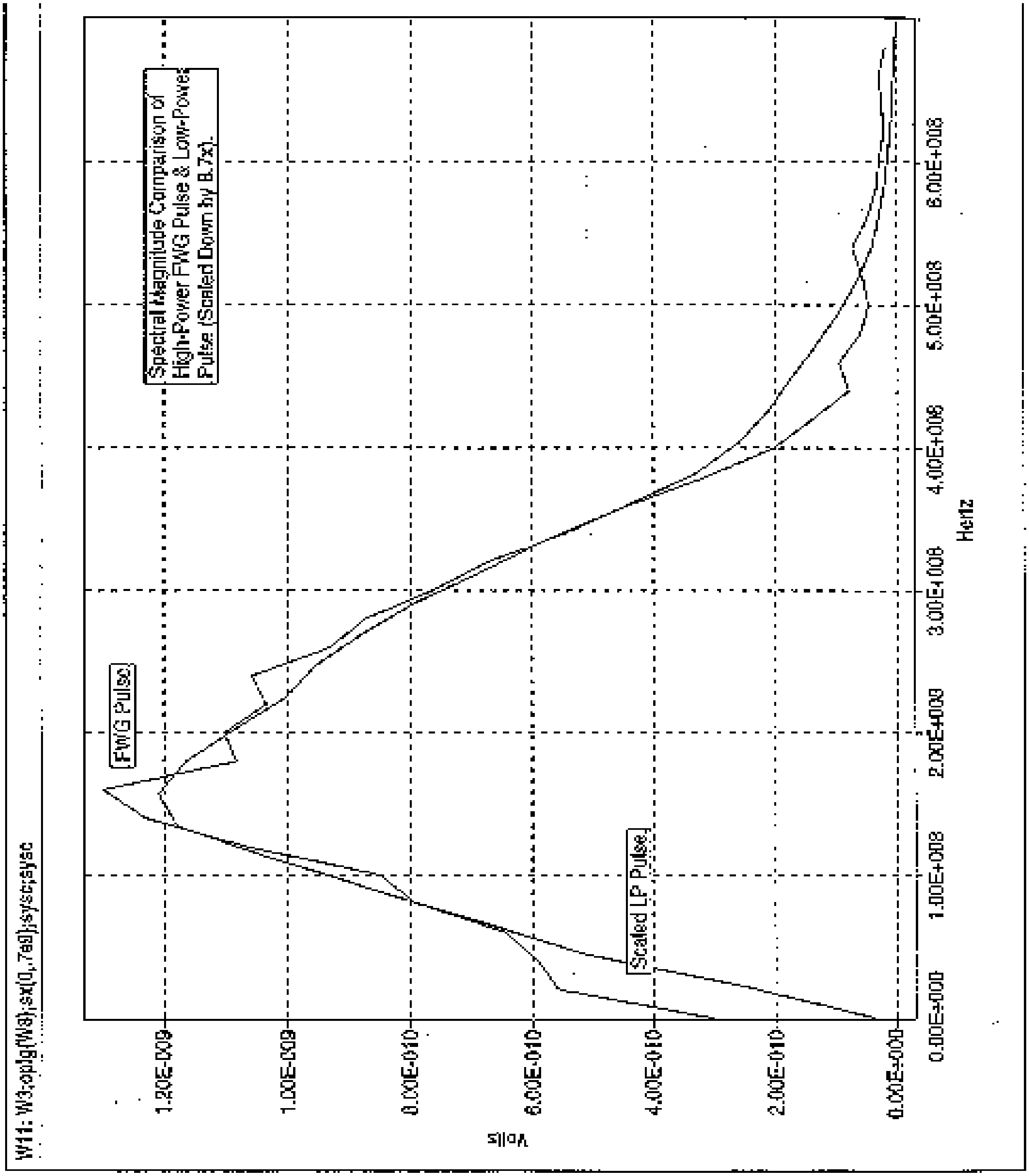

Fig. 23- Linear Magnitude Spectrum of Scaled Bipolar Pulse & FWG Pulse.

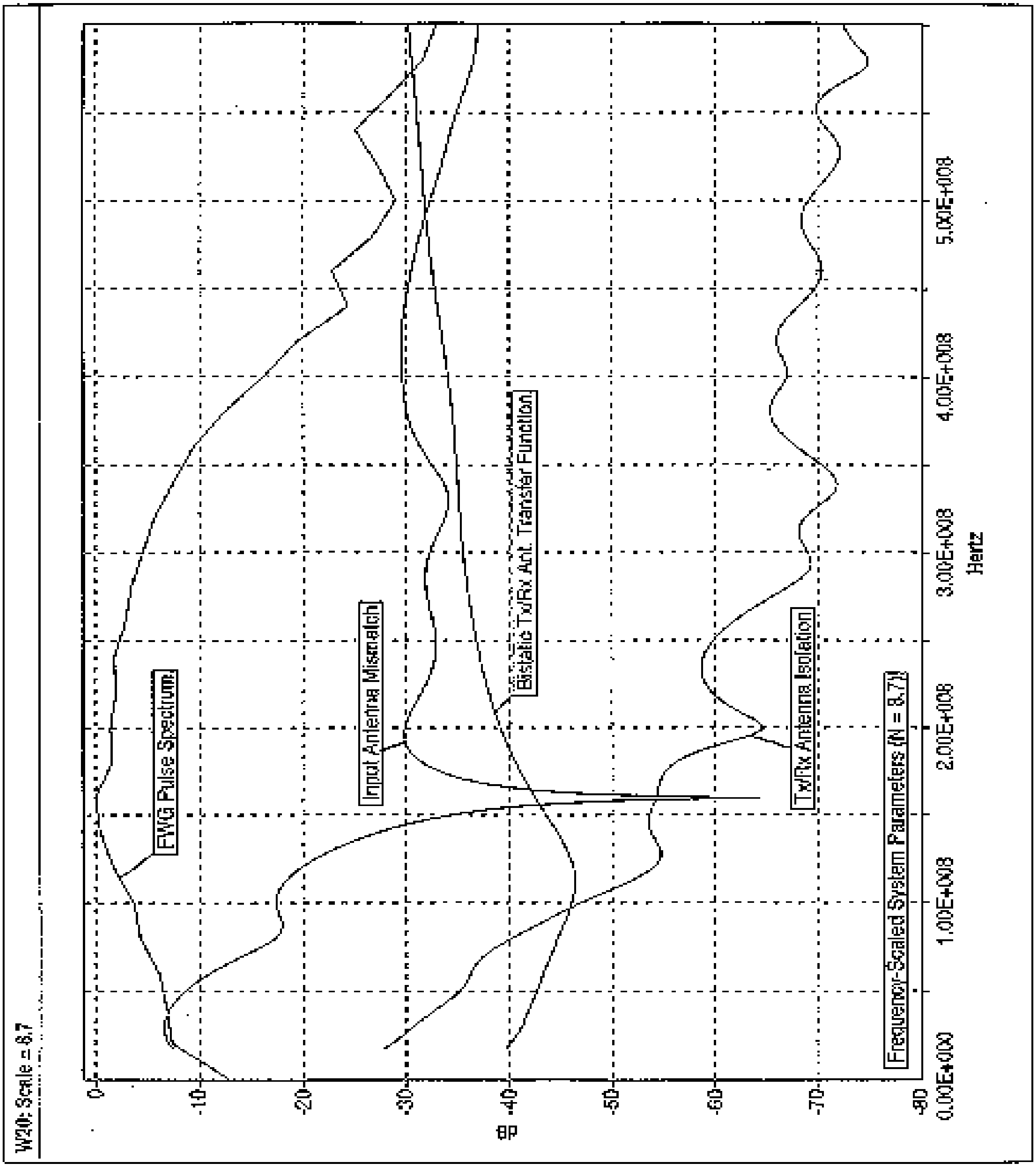

Fig. 24- System Parameters for Frequency Scaling of 8.7.

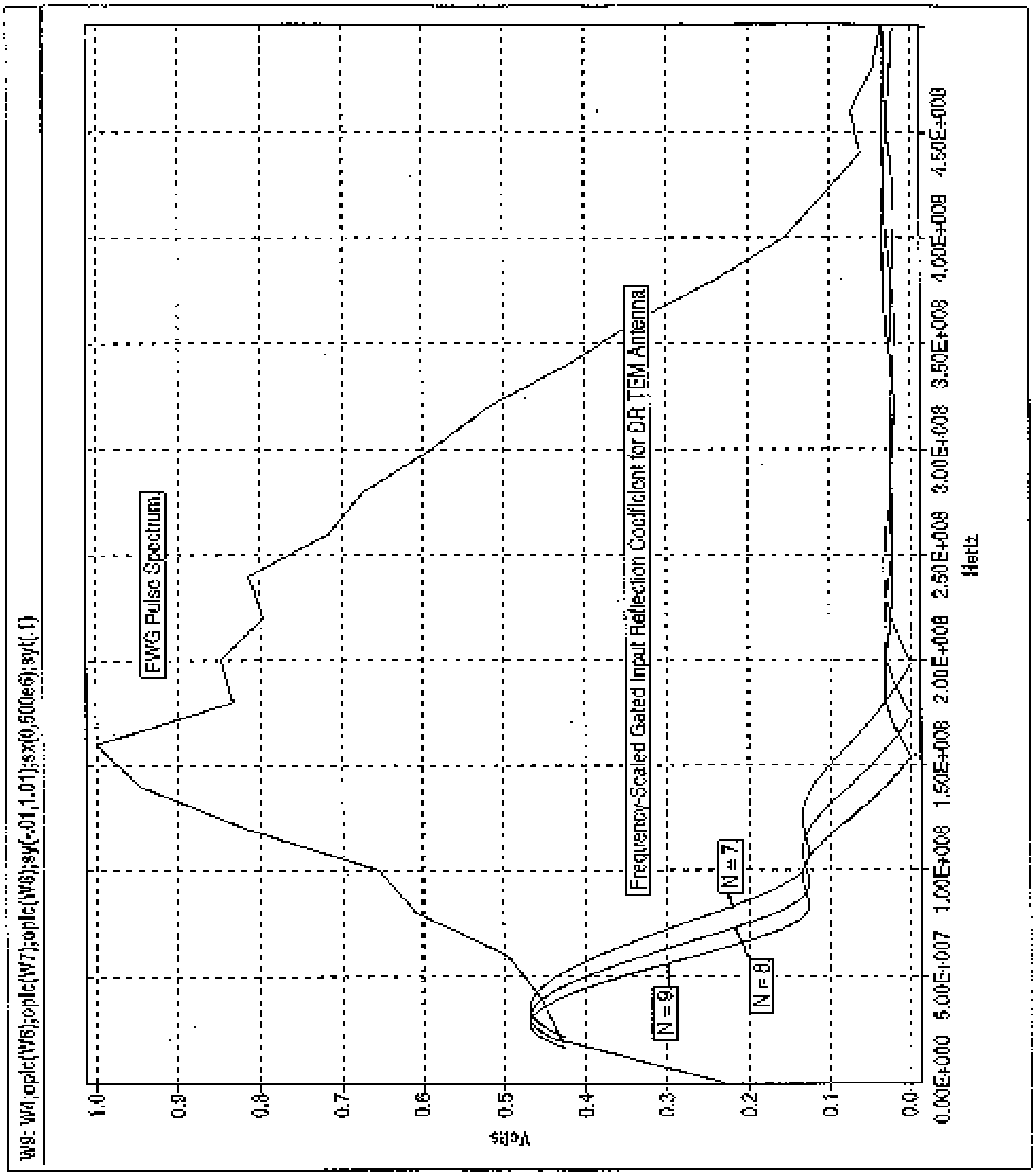

Fig. 25- Input Reflection Coefficient for Various Frequency Scaling.

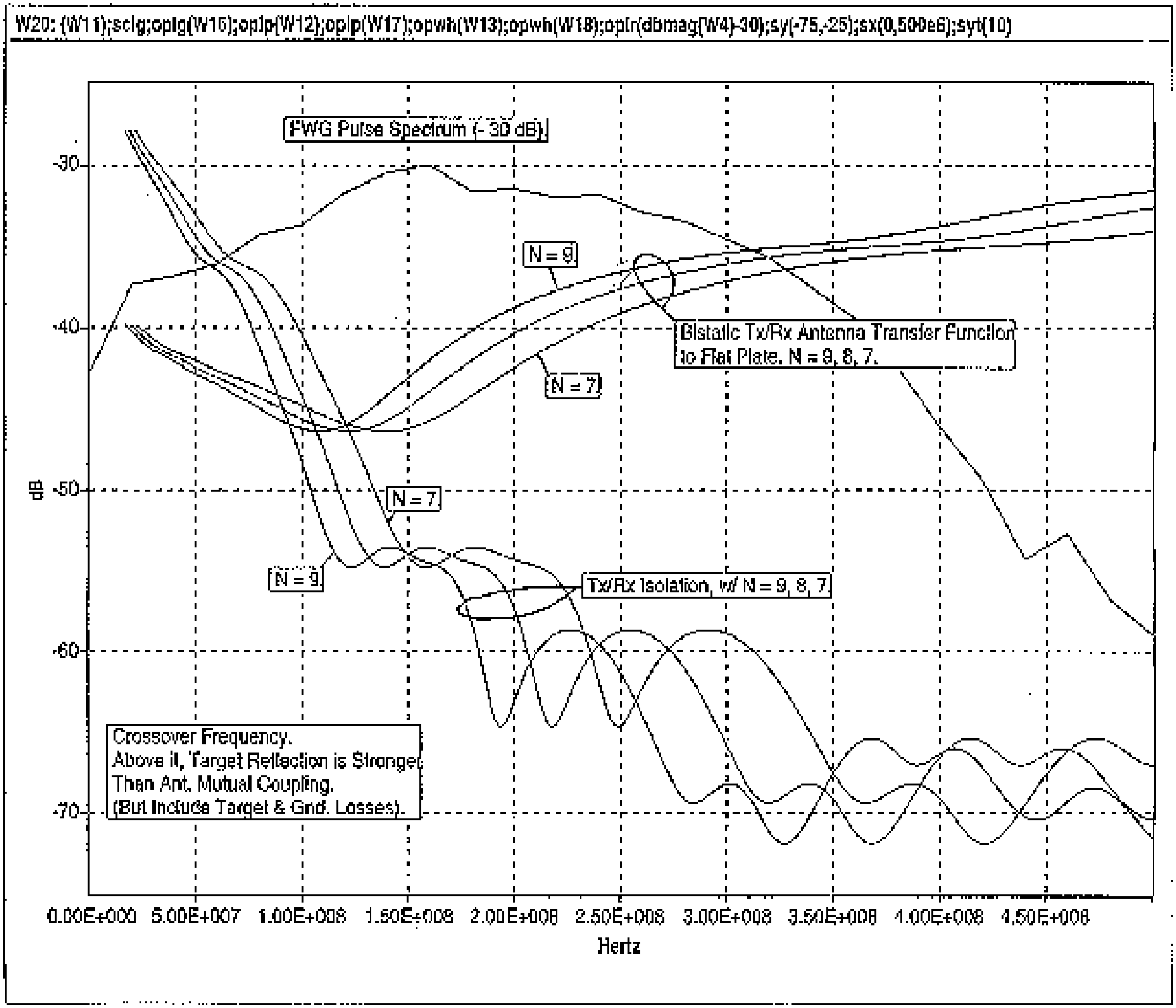

Fig. 26- Bistatic Transfer Function and Isolation for Various Frequency Scaling.

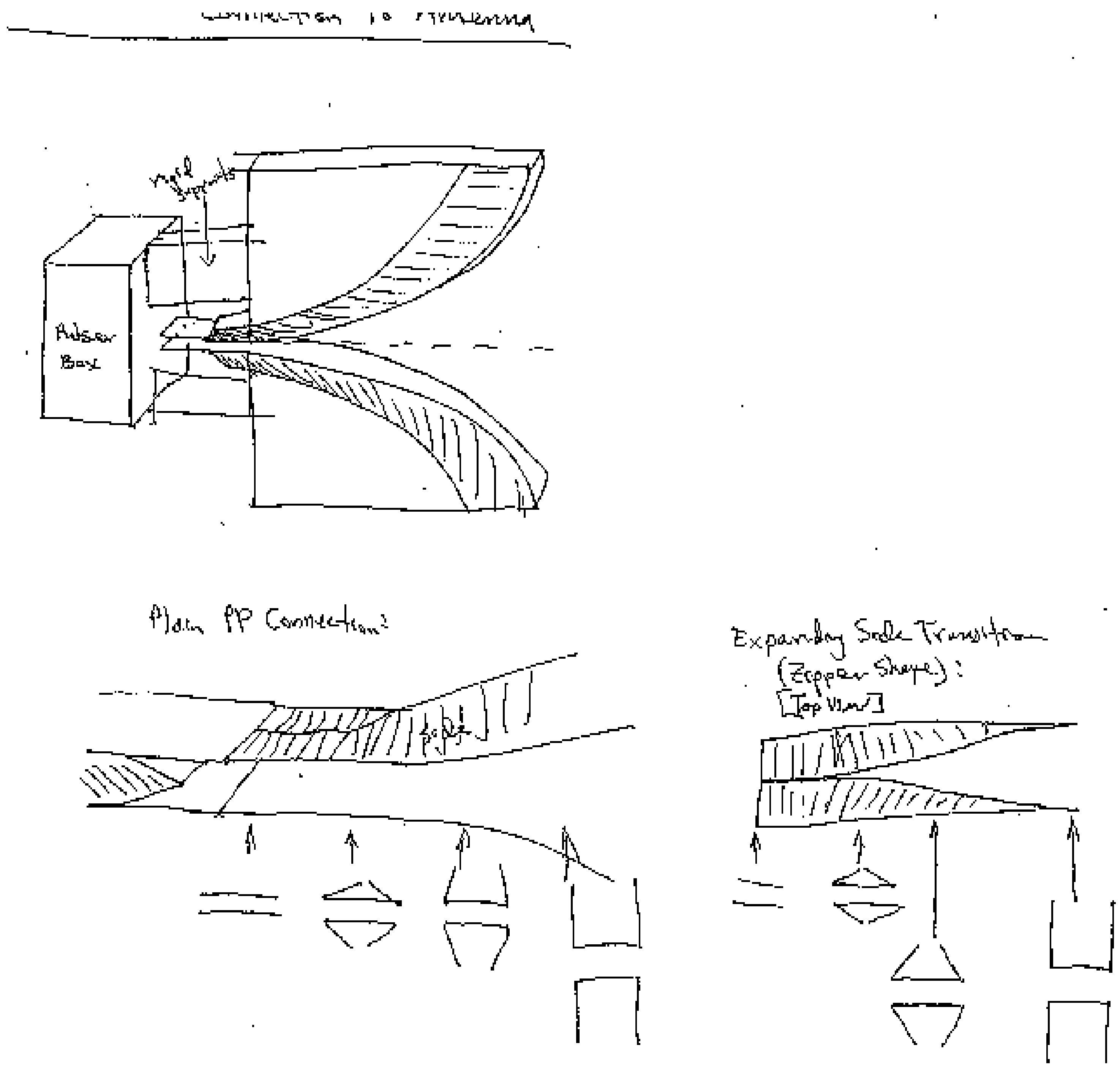

Fig. 27- Sketch of Proposed Input Transition for 100-Ω Parallel-Plate Pulser.

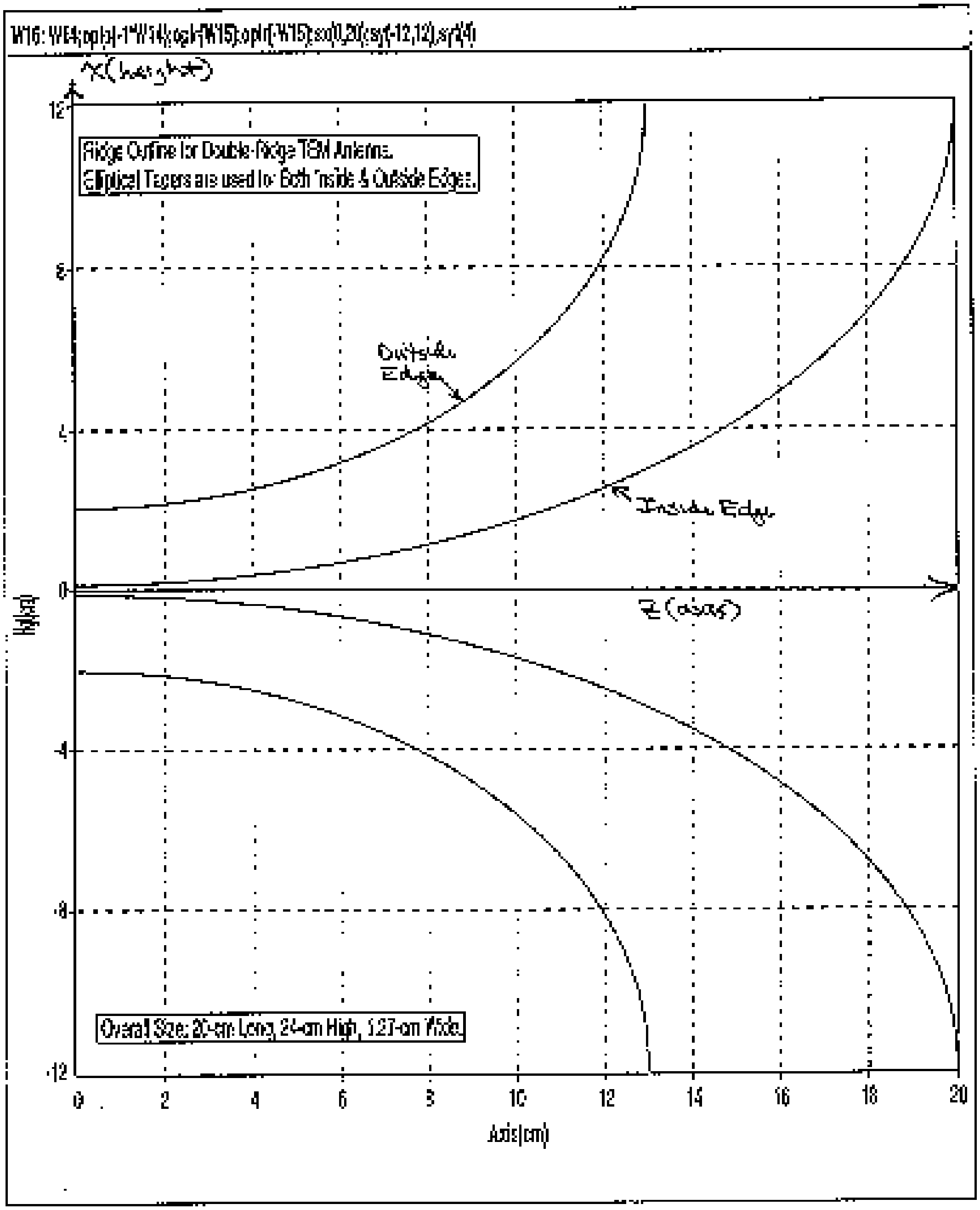

Fig. 28- Drawing of Double-Ridge Geometry for Scale-Model Antenna.

APPENDIX B
Simulations of GPR Backscatter from Buried Drums

Dr. John Aurand

June 2, 1999

Work Sponsored by Sandia National Laboratories
Contract BF-6512, Dr. Guillermo Loubriel

Introduction

This report describes numerical simulations of the electromagnetic backscatter propagation from buried 55-gal. drums, based on the modeling results of Dr. Larry Carin at Duke University. This work was performed under contract to Sandia Labs, for the LDRD 'An Electromagnetic Imaging System for Environmental Site Reconnaissance.' The purpose of the simulation work is to numerically analyze the ground-penetrating radar (GPR) problem and to quantify the viability of the proposed high-power GPR system for detecting buried drums in environmental reconnaissance applications.

The Duke modeling work yielded seven specific datasets for the electromagnetic backscatter from a buried drum (a perfectly conducting right circular cylinder with a diameter of 60 cm and a length of 90 cm), in a variety of orientations. These configurations included a vertically oriented drum with the top at a depth of 1 m, 2 m, and 3 m, as well as a horizontally oriented drum with the top edge at a depth of 0.7 m and 2.7 m (the axis of the drum was at depths of 1 m and 3 m). In addition, modeling was done of the horizontal drum with both parallel polarization and perpendicular polarization (i.e., the horizontal drum axis was parallel to the incident wave electric-field vector or the drum axis was perpendicular to the incident wave polarization, respectively). In all cases, the excitation plane wave is normally incident on the flat earth surface, and the scattered wave off of the buried target is computed as it emerges from the ground and back into air.

After these modeling data were obtained from Duke, we extended the frequency-domain datasets to higher frequencies, in a form useful for computing the time-domain response with inverse FFTs. We also developed a simulation methodology in the Dadisp software package for performing complete simulations of GPR system behavior (based on the Duke results).

Theory

For transient or pulsed time-domain excitation, the incident plane wave impinging on the ground is $E_i(t)$, with a Fourier spectrum $E_i(f)$. This wave partially reflects at the air-ground interface and partially transmits into the earth. The wave transmitted into the earth then propagates down to the buried target (a right circular PEC cylinder with a diameter of 60 cm and a length of 90 cm). The wave induces surface currents on the target, which then reradiate and the resulting scattered wave heads back toward the earth surface. This wave partially reflects back down at the air interface and partially transmits out into the air. The overall wave returning to the GPR system above the earth will be denoted as $E_r(t)$, and in time sequence it consists of the initially-reflected surface bounce $E_{r1}(t)$, and then some time later, the emerging wave that had reflected off of the buried target, $E_{r2}(t)$:

$$E_r(t) = E_{r1}(t) + E_{r2}(t).$$

Note that other waves will emerge later in time due to multiple reflections between the buried target and the earth surface, but because of the attenuating properties of the soil, these components will be much lower in amplitude than the single-pass waves defined above.

The ‘surface bounce’ wave, $E_{r1}(t)$, which reflects off the ground, has a spectrum $E_{r1}(f)$, which is determined by the surface reflection coefficient, $\Gamma_1(f)$:

$$E_{r1}(f) = \Gamma_1(f)\ E_i(f).$$

For normal incidence (where the angle of incidence is 90°), there are no angles involved and the surface reflection coefficient is simply given by

$$\Gamma_1(f) = \frac{1-\sqrt{\varepsilon_{re}(f)}}{1+\sqrt{\varepsilon_{re}(f)}},$$

with the soil having a complex effective dielectric constant of

$$\varepsilon_{re}(f) = \varepsilon_r'(f) - j\ \varepsilon_r''(f) = \varepsilon_r(f)\ \left[1 - j\ p_e(f)\right].$$

Note that $\varepsilon_r(f)$ is the dielectric constant or relative permittivity (ε_r'), and $p_e(f)$ is the effective loss tangent

$$p_e(f) = \frac{\varepsilon_r''}{\varepsilon_r'} = \frac{\sigma}{\varepsilon_r' \varepsilon_0 \omega},$$

and $\sigma(f)$ is the earth conductivity.

The real and imaginary parts of the complex dielectric constant utilized in the Duke modeling work were obtained from Fig. 7 of Hipp, for 1.2 g/cc Puerto Rico clay loam with 10% moisture by dry weight *[Jackie E. Hipp, ‘Soil Electromagnetic Parameters as Functions of Frequency, Soil Density, and Soil Moisture,’ Proc. of IEEE, v. 62, n. 1, Jan. 1974, pp. 98-103]*. This represents moderately lossy soil properties for the electromagnetic wave propagation. The dielectric constant is shown in Fig. 1 below.

Now the second reflected wave component, $E_{r2}(t)$, is the wave which propagated down to the drum, scattered off the drum, and propagated back to the surface and out into air. In terms of modeling the single-pass propagation down to the drum and back out, the spectrum of $E_{r2}(t)$ may be formed as a cascaded linear-system combination of the following factors: the transmission coefficient into the earth, the exponential propagation down to the target, the target scattering function, exponential propagation back up to the surface, and the transmission coefficient out into air. These factors are combined by simple multiplication in the frequency domain, and can be used to define an overall scattering transfer function for the buried drum. Let $S(f)$ represent the overall buried-drum scattering transfer function – that is:

$$S(f) = \frac{E_{r2}(f)}{E_i(f)}.$$

This is the spectral ratio of the emerging wave from the ground (scattered from the drum) and the incident plane wave.

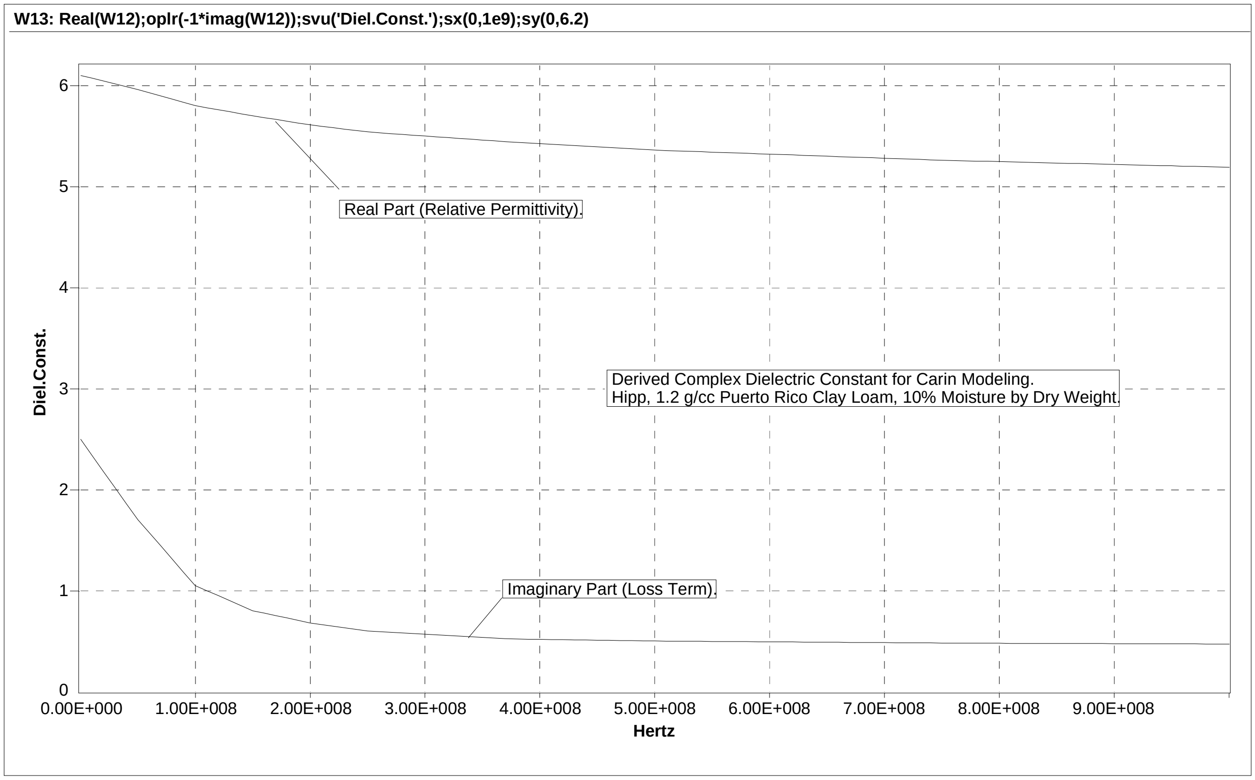

Fig. 1*- Components of soil dielectric constant used in modeling work.*

For normal incidence, the transmission coefficient from the air into the earth is simply

$$T_1(f) = 1 + \Gamma_1(f),$$

whereas the transmission coefficient from the earth back into the air is the complement:

$$T_1'(f) = 1 - \Gamma_1(f).$$

The exponential propagation from the earth surface down to the top specular surface of the buried target at a depth *d* is $e^{-\gamma d}$, where the complex propagation constant is

$$\gamma(f) = \frac{j\omega}{c}\sqrt{\varepsilon_{re}(f)} = \frac{j2\pi f}{c}\sqrt{\varepsilon_r'(f) - j\,\varepsilon_r''(f)}.$$

The real part of $\gamma(f)$ is the attenuation constant, and the imaginary part is the phase constant.

And the target scattering function may be modeled as a wave reflection coefficient, $\Gamma_2(f)$, which would include all the reradiation due to the induced surface currents on the buried target. If the target were a very large, horizontal, flat metal plate, then $\Gamma_2(f) = -1$. That is, the flat plate would completely reflect the incident wave propagating in the ground, and would reverse the polarity of the electric field vector (this is just like a short-circuit load on a transmission line). But because the target of interest is a drum, the scattering will be much different. For the finite drum, several reradiated wave components will be generated due to the complexity of the induced surface currents running around the body of the drum. And because the soil surrounding the drum is lossy, these induced currents will be dampened out rather quickly compared to the case of a drum in free space. Note too that this target reflection coefficient is defined for the waves inside the earth – it is fundamentally different than the scattering function for a drum in free space, or the associated concept of radar cross section.

Finally, using the factors defined above, we form the cascaded single-pass model for the buried-drum transfer function as

$$S(f)=\frac{E_{r2}(f)}{E_i(f)}=T_1(f)\,e^{-\gamma d}\,\Gamma_2\,e^{-\gamma d}\,T_1'(f).$$

And after substitution,

$$S(f)=\left[1-\Gamma_1^2\right]e^{-2\gamma d}\,\Gamma_2(f).$$

Knowing the complex dielectric constant of the soil, $\varepsilon_{re}(f)$, both $\Gamma_1(f)$ and $\gamma(f)$ may be computed directly. This leaves the only unknown in the problem to be the buried-drum reflection coefficient, $\Gamma_2(f)$. This is the primary value of the Duke modeling work – to determine the scattering characteristics of the buried drum.

The Duke modeling work was done with a frequency-domain moment method code, in which the buried-drum transfer function, $S(f)$, was computed for sinusoidal excitation (the time-harmonic basis function is $e^{j\omega t}$, where $\omega=2\pi f$). This was done for 100 discrete frequencies, DC to 990 MHz, in 10-MHz increments. This scattering transfer function did not include the initial surface bounce, $E_{r1}(t)$, but it did include all the multiple wave reflections between the earth surface and the buried drum. And it assumed that the incident wave was planar. In actuality, the incident wave will be spherically expanding downward from the transmitter antenna positioned above the earth at a height *h*. Note too that the emerging wave, $E_r(t)$, will also spherically expand into the air, so that at *h*, the electric field will be $E_r(t)/h$.

If simulation information is only required in the frequency domain, then these particular datasets from Duke would have been sufficient to work with. Unfortunately, we also desire the time-domain characterization of this GPR propagation problem, both for understanding the propagation phenomenology, and more importantly, for comparing with future actual high-power GPR experiments, in which the primary data are direct time-domain waveforms. It thus becomes necessary to employ digital signal processing, and specifically, fast Fourier transforms (FFTs) to convert from the sampled time domain to the discrete frequency domain.

For a time-domain record of *N* samples with a sample interval of Δt, the equivalent sampling rate is $f_s = 1/\Delta t$. And the standard FFT of this time record will yield a complex record with both positive frequency content and phase-conjugated negative frequency content. The FFT record has a frequency interval of Δf, strictly determined by

$$\Delta f=\frac{1}{N\Delta t}.$$

There is a DC ($f=0$) value, then $N/2$ positive-frequency values (up to the folding frequency, which is $f_s/2$), then the phase-reversed 'mirror image' negative-frequency values.

The Duke frequency-domain datasets have $\Delta f=10$ MHz, and the Sandia experimental instruments have a sampling interval of $\Delta t=100$ ps. Thus, if we choose $N=1024$ as the record size, the numerical sampling and experimental sampling requirements will both be met. That is, for the numerical simulations we choose $\Delta f=10$ MHz and $N=1024$ (a power of 2 for FFTs), so that $\Delta t=\frac{1}{N\Delta f}=97.65625$ ps. And for the experimental measurements, $\Delta t=100$ ps and $N=500$. Then it will be easy to convert the Duke datasets into FFT frequency-domain records, and it will be relatively straightforward to compare the numerical and experimental waveforms. Note that the other sampling requirement is that the sampling rate be fast enough (Δt be short enough) to contain the dominant frequency-domain content in the corresponding FFT spectrum, or else there will be severe aliasing errors in both domains. This is based on the Nyquist sampling theorem. In addition, for waveform recorders, the analog input bandwidth must obviously be wide enough for accurate measurements of the transient signals of interest. In this case, measuring a pulsed VHF signal with center frequency of about 250 MHz, the recorder bandwidth should be at least 1 GHz or so.

As a result of the parameters chosen above, the Duke datasets had to be extended or extrapolated above 990 MHz. With $\Delta f = 10\ \mathrm{MHz}$ and $N = 1024$, the folding frequency is 5.12 GHz, and the positive-frequency portion of the FFT record is DC to 5.12 GHz. So what frequency-domain values should be used from 1.00 GHz to 5.12 GHz? Fig. 2 shows the original Duke $S(f)$ dataset for a vertical drum 1 m deep, and the corresponding complete FFT form that was subsequently developed for further processing in Dadisp.

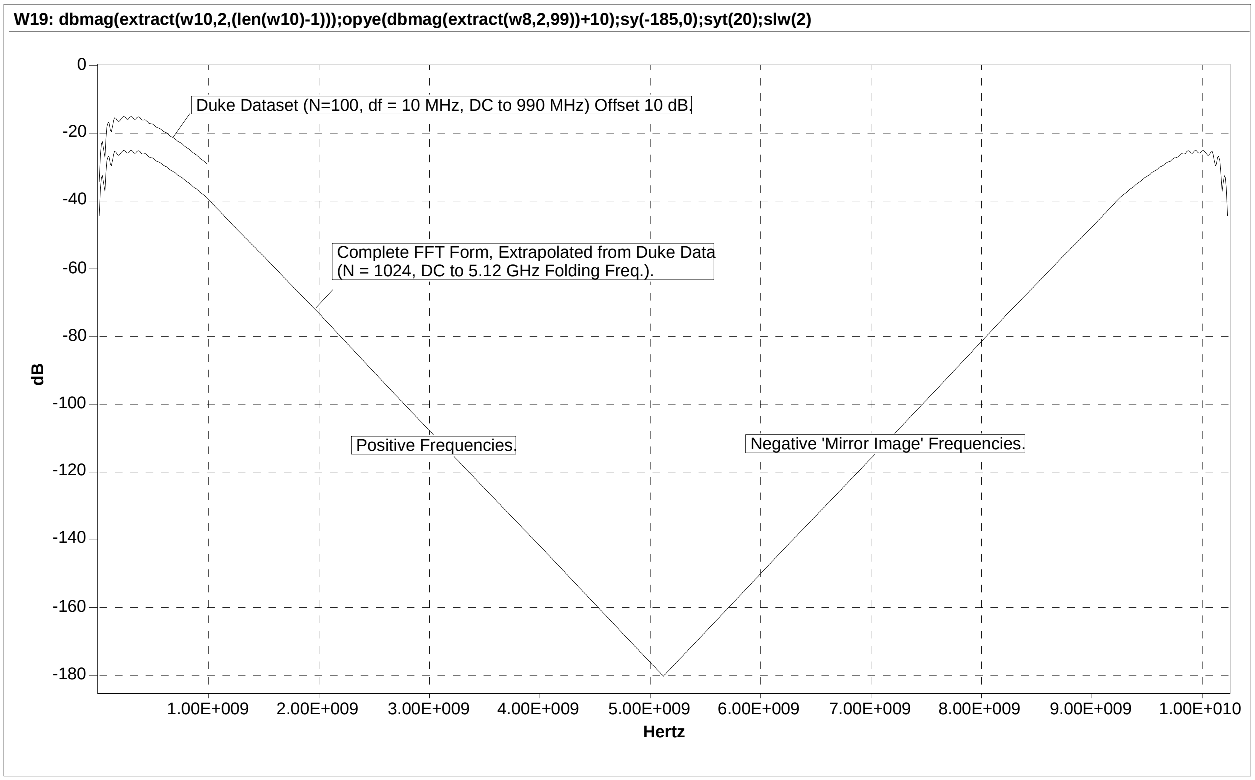

***Fig. 2**- Decibel comparison of S(f) transfer function from Duke and complete FFT form for further processing. Data is for vertical drum 1 m deep.*

Several methods were considered for extrapolating the Duke data (0 to 0.99 GHz) to the remaining higher-frequency range necessary for further signal processing (1.00 to 5.12 GHz). The most straightforward and accurate method was to utilize the theoretical single-pass transfer function for a buried flat plate:

$$S_{fp}(f) = \left[1-\Gamma_1^2\right] e^{-2\gamma d}\ \Gamma_2(f),$$

where the reflection coefficient of the flat plate is $\Gamma_2(f) = -1$. So $S_{fp}(f)$ was computed as

$$S_{fp}(f) = \left[1-\Gamma_1^2(f)\right] e^{-2\gamma(f)d}\ (-1).$$

The complete FFT-form approximation of the buried-drum transfer function, $S(f)$, was then given by the combination of the Duke portion, $S_0(f)$, for $f = 0 \text{ to } 0.99 \text{ GHz}$, and the flat-plate portion, $S_{fp}(f)$, for $f = 1.00 \text{ to } 5.12 \text{ GHz}$. The amplitude response was made piecewise continuous by scaling the flat-plate portion by the magnitude ratio of the two functions at the breakpoint, 990 MHz:

$$S(f) = \begin{cases} S_0(f), & \text{for } f = 0 - 0.99 \text{ GHz} \\ S_{fp}(f)\dfrac{\left|S_0(0.99 \text{ GHz})\right|}{\left|S_{fp}(0.99 \text{ GHz})\right|}, & \text{for } f = 1.00 - 5.12 \text{ GHz}. \end{cases}$$

Note that the phase response of each portion was left unmodified. This introduces an error in the resulting computations, but it is not as significant as the error due to the approximation of an infinite flat plate as the buried scatterer rather than the drum. Fortunately, the amplitude response of the true data (from the Duke modeling), $S_0(f)$, is falling off rapidly as this 990-MHz breakpoint is introduced, so the resulting erroneous features contained in the inverse-FFT time-domain responses are relatively small. It should be noted that these errors are present in the processing, and indicate that for FFT processing for this particular GPR problem, the upper end of 990 MHz for the Duke modeling work is barely high enough. The simulation results in time would have been much cleaner if the Duke moment-method work had been done up to about 2 GHz – so that the incorrect features resulting from these 'breakpoint' or extrapolation errors would have been further reduced. In Fig. 2 above, the slope (in dB/GHz) is slightly different for the two portions of the transfer function, a direct indication that the flat-plate target assumption is indeed just an approximation to the actual buried drum.

Vertically Oriented Drums

The above processing was performed for the three buried-drum transfer function datasets provided by Duke for the vertically oriented drum configuration. The top of the drum was either 1 m, 2 m, or 3 m deep. This was done in the 'ws3_VertDrums' worksheet of Dadisp. The Duke portion, $S_0(f)$, was loaded into the worksheet, then the flat-plate portion, $S_{fp}(f)$, was computed, and then they were combined to form the complete FFT version of $S(f)$. These complete buried-drum transfer functions were saved in a Dadisp dataset, then brought back into the worksheet for comparison and computation of the impulse response with the inverse FFT.

Fig. 3 shows these three backscatter transfer functions. Note the increasing roundtrip attenuation with drum depth as expected for the wave propagating through lossy soil. In Fourier analysis, the presence of frequency-domain ripple typically indicates some sort of time-domain ringing or beating. Comparing the three traces, above 200 MHz the ripple reduces as depth increases. This is probably showing the effect of reduced multipath between the earth surface and the buried drum top as depth increases. On the other hand, below 200 MHz the ripple is relatively independent of depth, probably indicating the self resonances of the drum as a finite scattering object.

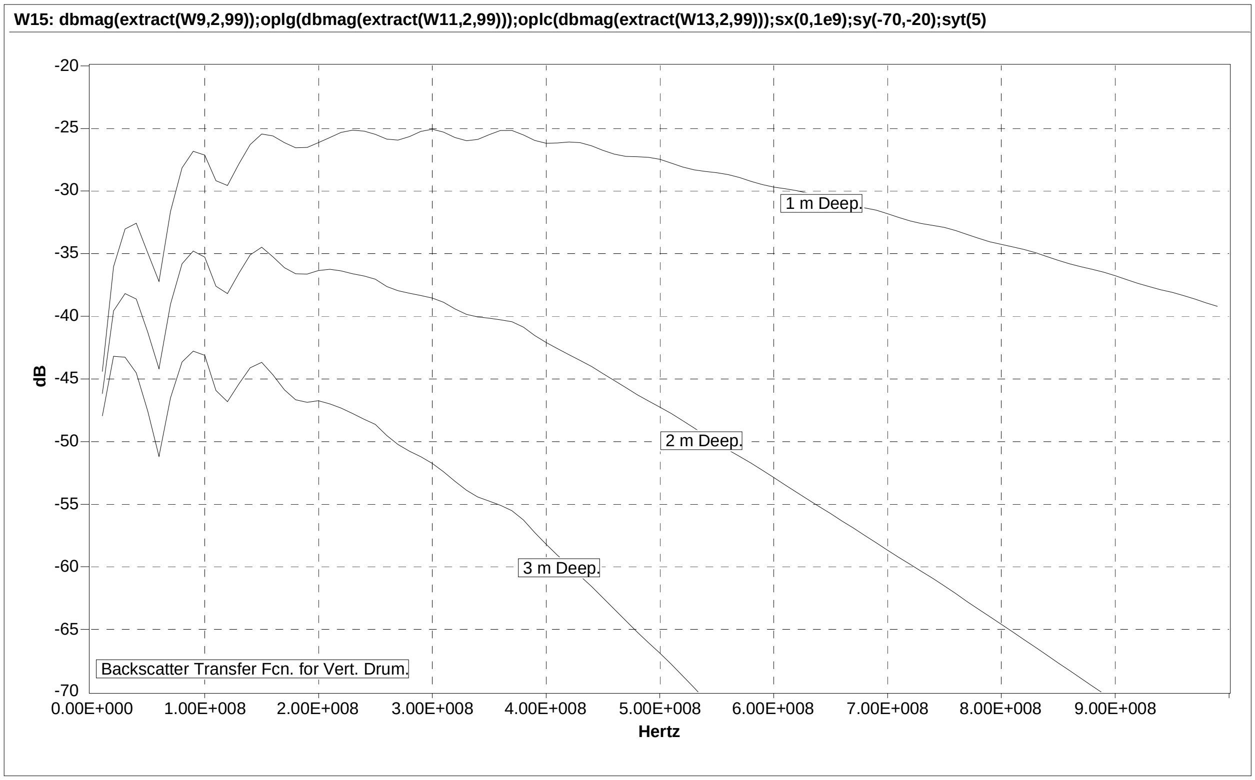

Fig. 3*- Decibel plot of S(f) transfer function for vertical drum at depths of 1 m, 2 m, and 3 m.*

The impulse response in time is computed with the inverse FFT; the theoretical impulse response represents the time response of the system under test (this backscatter propagation scenario) to an ideal infinitely fast impulse with an infinite bandwidth. Later on, we will examine the response to realistic GPR system pulses of finite bandwidth. Fig. 4 provides the actual impulse response for the three drum depths. Note that both amplitude attenuation and phase dispersion affect the transient response with depth – there is both peak amplitude reduction and pulsewidth spreading in time. At this level of the analysis, it is not easy to separate the time-domain effects of attenuation and dispersion – but they are both present here. Note too that the primary impulse response is negative – indicating the negative scattering off of the conducting drum.

One interesting item to note is that as depth increases, the peak frequency of the transfer function shifts lower, and because the dielectric constant increases with lower frequency (for the given soil type – see Fig. 1), the roundtrip propagation time of the impulse peak increases as well. For a dielectric constant ε_r which is relatively constant over the frequency range of a given pulse spectrum, the roundtrip time through the soil is simply

$$T = \frac{2d}{c}\sqrt{\varepsilon_r}\,.$$

This equation can be solved for the dielectric constant, given the depth and roundtrip travel time:

$$\varepsilon_r = \left(\frac{cT}{2d}\right)^2.$$

Or it can be used to compute the depth of a buried target from a measurement of the propagation time:

$$d = \frac{cT}{2\sqrt{\varepsilon_r}}.$$

Now for this particular soil type, we can see the effect of the downshifted transfer function peak versus depth. For the 1-m deep drum, the apparent dielectric constant was 4.95 – based on $d = 1\ \mathrm{m}$ and $T = 14.84\ \mathrm{ns}$ (the speed of light $c = 0.3\ \mathrm{m/ns}$). For the 2-m deep drum, the apparent permittivity was 5.22, and for the 3-m deep drum, $\varepsilon_r = 5.31$.

A secondary item to note in Fig. 4 is that the 1-m deep trace has an obvious ringing with a period of 1 ns, or a frequency of 1 GHz. This is the erroneous time-domain feature caused by the breakpoint in the extrapolated transfer function. Notice that it is not present in the deeper drum traces – consistent with greater falloff (at 990 MHz) from the peak in the transfer function. Thus, this fast ringing in time can be ignored as an unavoidable artifact of the processing – if the Duke datasets had been computed to a higher frequency, this ringing would have been reduced.

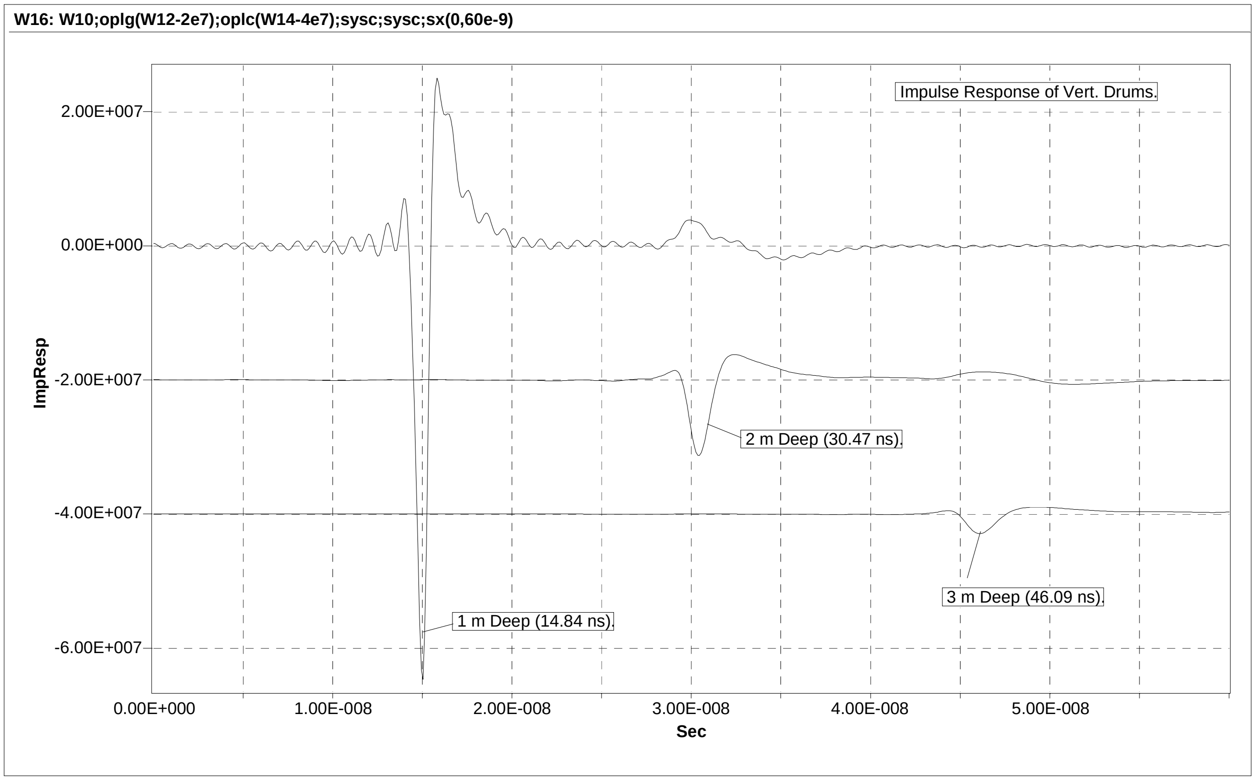

Fig. 4- ***Time-domain impulse response of vertical drum at depths of 1 m, 2 m, and 3 m.***

These impulse responses are shown with normalized peak amplitudes in Fig. 5 for easy comparison of pulse shape. The obvious conclusion to make is that as the target depth increases, the higher frequencies get attenuated more, resulting in a lowpass-filtering effect. For an effective GPR system design, this implies that for deeper targets, the system spectral content should be shifted down in frequency for a given overall system sensitivity.

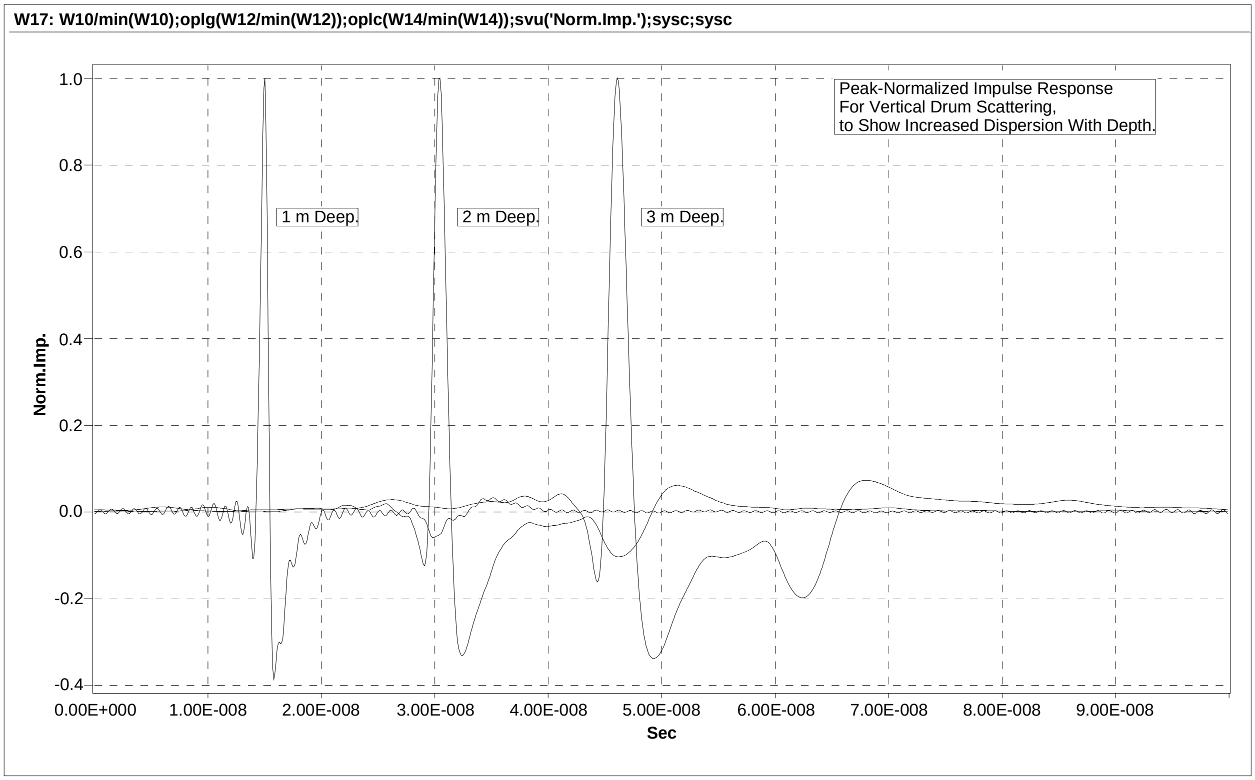

Fig. 5-*Peak-normalized time-domain impulse response of vertical drum at depths of 1 m, 2 m, and 3 m.*

Horizontally Oriented Drums

Similar processing was performed on the four Duke datasets for horizontal drums. This was done in the 'ws4_HorDrums' worksheet of Dadisp. These datasets included two polarizations for a drum buried at a top-edge depth of 70 cm, and two polarizations at a top-edge depth of 2.7 m (the axis of the drum was 1m or 3 m deep respectively). Additional work was required, however, because a different program was used at Duke to compute the backscatter for the horizontal drum orientations, and the time reference wasn't at the earth surface (as it was for the code used for the vertical drum modeling). After examining this time-reference issue, we could not determine what the actual reference was for the horizontal runs. Consequently, we resorted to the best approximation we could, given the data we had available – using the vertical drum runs (with correct time delays) for providing an approximate time reference for the horizontal runs. As a result, the Duke transfer function, $S_0(f)$, had to be modified to include an additional phase lag term for consistent impulse response times. The modified buried-drum transfer function from Duke was computed as:

$$S_0'(f) = S_0(f)\, e^{-j\omega\Delta T},$$

where ΔT is the additional time delay necessary for correct impulse response timing. This was determined by subtracting the (incorrect) impulse response peak time (based on the original dataset), T_0, from the estimated correct roundtrip time, $\tilde{T}_h$, for the specular bounce off the top edge of the buried horizontal drum. And $\tilde{T}_h$ was computed using the simple time formula given above (p. 7), based on the actual propagation time, T_v, for the vertical drum orientation (which were correct for all three depths). That is, for $d = 70\ \text{cm}$,

$$\tilde{T}_h(70\ \text{cm}) = T_v(100\ \text{cm})\frac{70\ \text{cm}}{100\ \text{cm}} = (14.84\ \text{ns})(0.7) = 10.388\ \text{ns}.$$

Then the additional time delay necessary to include in the phase response of $S_0'(f)$ was given by

$$\Delta T = \tilde{T}_h - T_0 = 10.388 - 3.808 = 6.580\ \text{ns}.$$

In the same way, the necessary time-delay correction for the drum buried with the top edge at $d = 2.7\ \text{m}$ was computed:

$$\begin{aligned}\Delta T = \tilde{T}_h - T_0 &= T_v(3)\tfrac{2.7}{3} - T_0\\ &= (46.094)\tfrac{2.7\ \text{m}}{3.0\ \text{m}} - 21.777 = 19.707\ \text{ns}.\end{aligned}$$

So the backscatter transfer function had the phase response modified as described, and then the steps employed in the vertical drum processing were also performed for these horizontal drum datasets. This approximate time-reference correction in the phase response should provide a timebase accuracy better than 1 ns.

The resulting complete form of the buried-drum transfer function for the horizontal drum (both polarizations) at a depth of 70 cm is shown in Fig. 6. Note that the transfer function magnitude is stronger than for the vertical 1-m case, due to being closer to the surface. Parallel polarization is for the incident field parallel to the drum axis, and perpendicular is for the orthogonal case. There is a fundamental difference between these two scattering orientations because of the different induced surface currents set up on the drum.

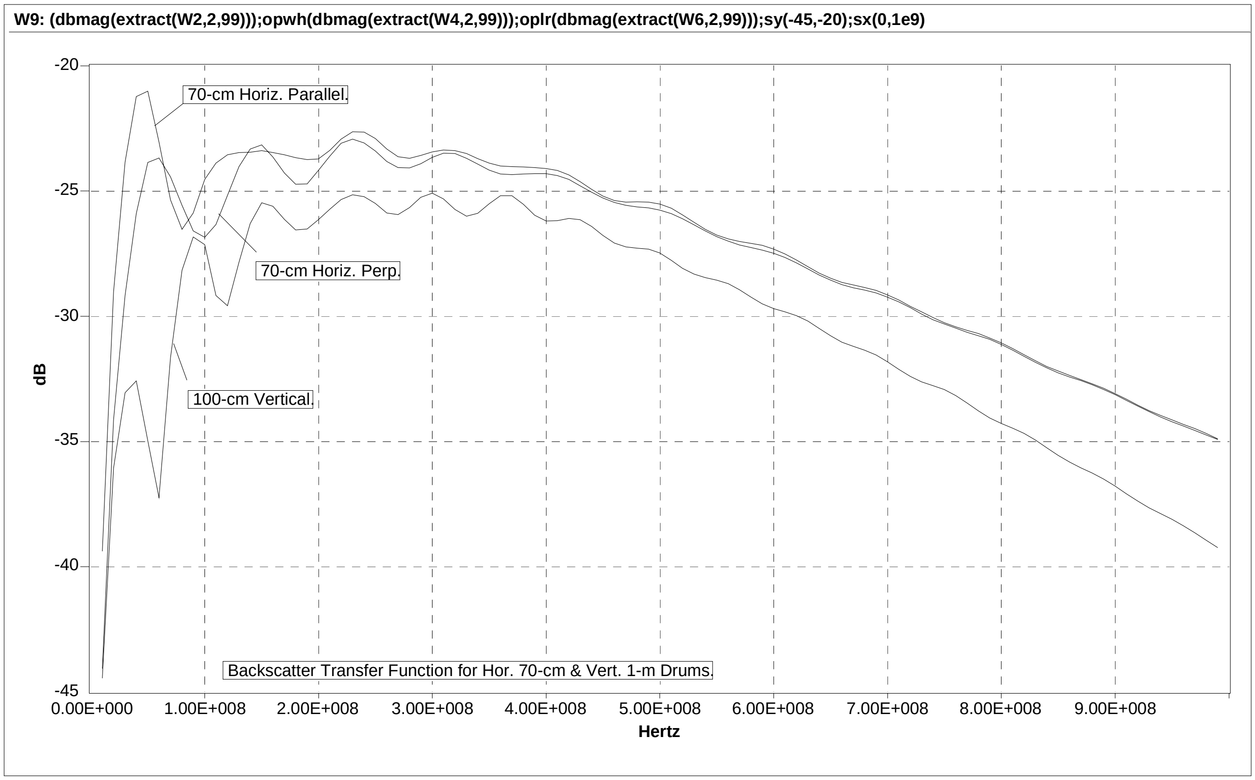

```
W9: (dbmag(extract(W2,2,99)));opwh(dbmag(extract(W4,2,99)));oplr(dbmag(extract(W6,2,99)));sy(-45,-20);sx(0,1e9)
```

Fig. 6- *Backscatter transfer function for horizontal drum (two polarizations) at a top-edge depth of 70 cm and for vertical drum at 100 cm.*

Fig. 7 is a plot of the inverse-FFT impulse response of the 70-cm horizontal drum. The two polarizations look similar, but are overshadowed by the strong secondary bounce between the earth surface and the top of the drum (there is an inflection in both waveforms at about 22 ns – twice the roundtrip time for the specular bounce). There is also the erroneous 1-GHz ringing feature present, due to the breakpoint in the extrapolation of the transfer function.

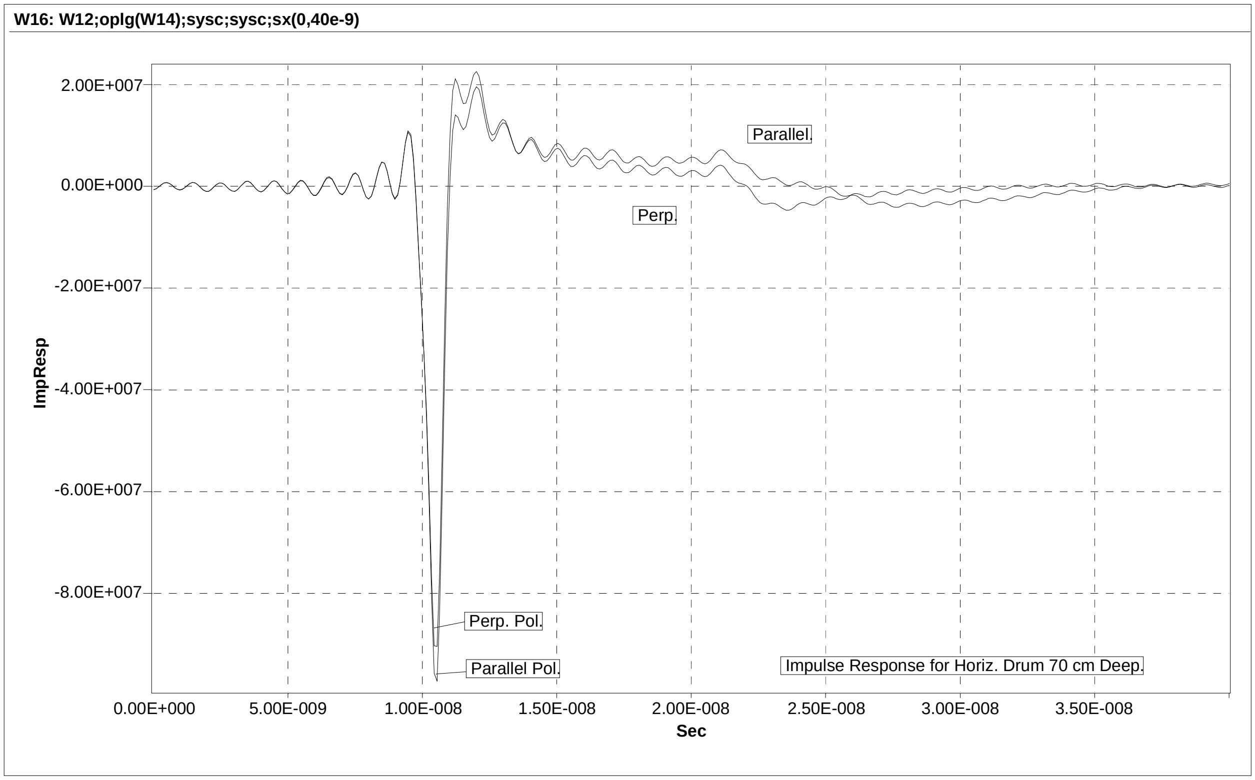

Fig. 7- *Time-domain impulse response of horizontal drum (two polarizations) at a depth of 70 cm.*

Fig. 8 gives the transfer function for the 2.7-m deep horizontal drum (and 3-m deep vertical drum for comparison). The primary passband amplitude is in between that of the vertical drum at depths of 2 m and 3 m. This is reassuring in terms of GPR system viability, because it indicates that the magnitude of the scattering from the drum is not strongly affected by the drum orientation (vertical with strong specular reflection from the flat circular end, parallel horizontal with fairly strong specular reflection from the parallel side, and perpendicular horizontal with diffracted specular reflection from the curved side). That was a primary technical issue to be addressed with this numerical modeling analysis. This finding implies that GPR system detection performance isn't affected too much by the actual orientation of the buried drum being searched for. But it should be noted that for a drum orientation that is tilted, the incident wave will be reflected off to the side, thus reducing the normal-incidence backscatter. The three drum orientations studied here, although limited to providing vertical specular backscatter, are still encouraging because they will cover a number of practical burial configurations.

And the corresponding impulse response for the 2.7-m deep horizontal drum is shown in Fig. 9. Here it is easier to see the time-domain scattering difference between the two incident polarizations. For the perpendicular case, we expect to see something like that of a sphere:

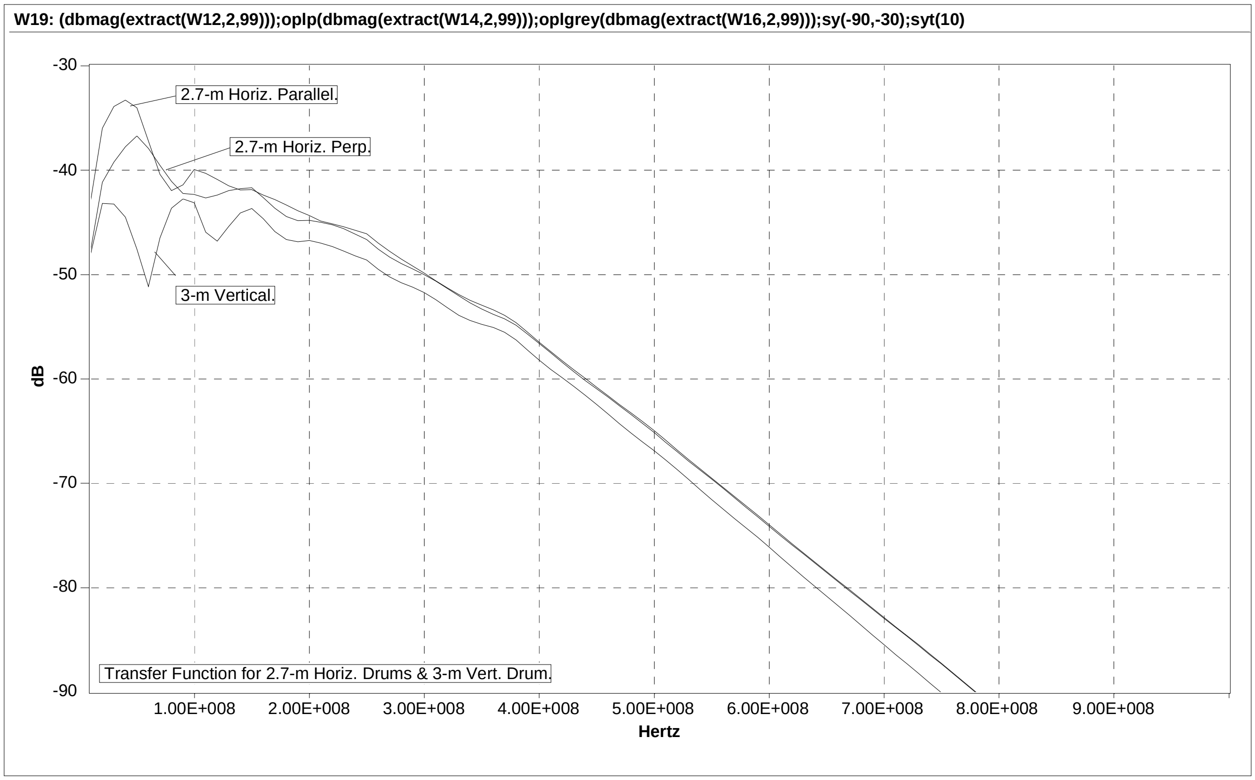

Fig. 8- *Backscatter transfer function for horizontal drum (two polarizations) at a top-edge depth of 2.7 m and for vertical drum at 3.0 m.*

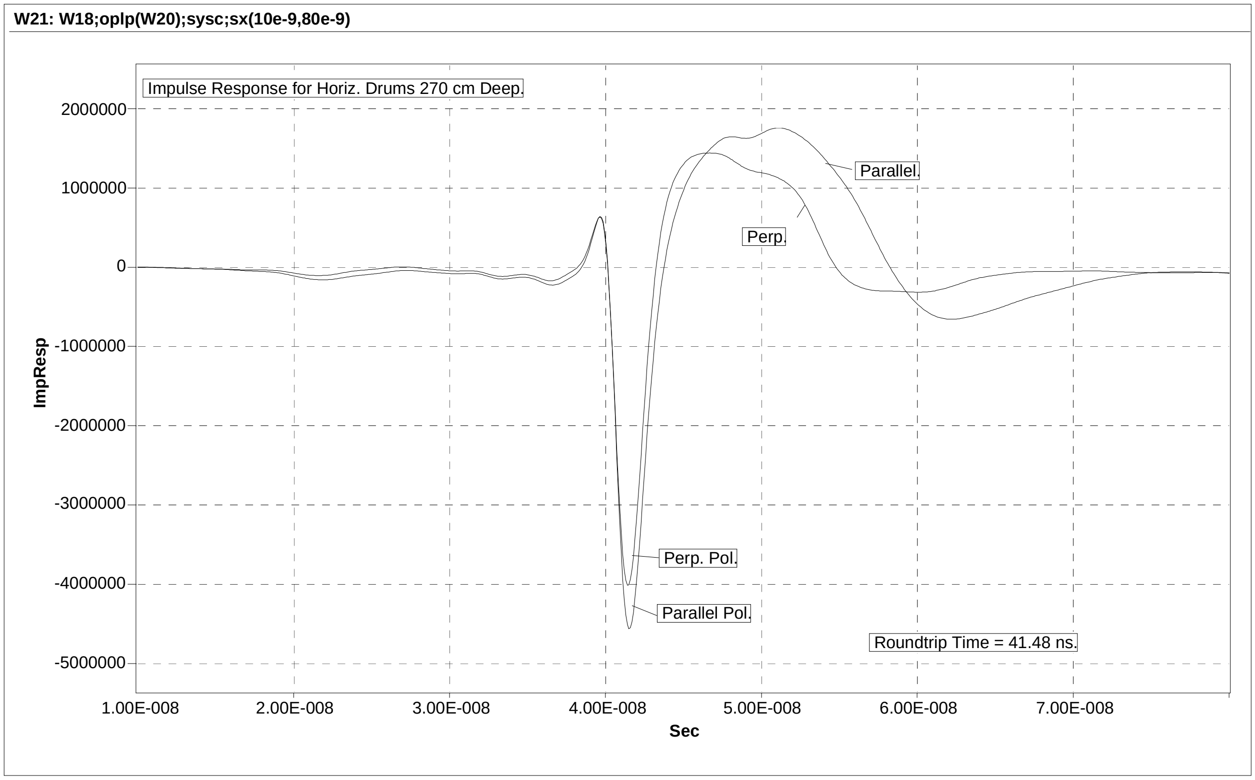

Fig. 9- *Time-domain impulse response of horizontal drum (two polarizations) at a depth of 2.7 m.*

a large specular bounce, an opposite extended reflection as the wave wraps around the drum, and then a creeping wave appear as the induced currents travel all the way around the circumference of the drum. This is indeed the situation. The parallel orientation has similar qualitative behavior, but the details are too involved to analyze here.

Finally, in Fig. 10, the impulse response for all horizontal drum orientations are shown in peak-normalized form for comparison of shape. The deeper drum yielded much cleaner transient results, due to both reduced surface-drum wave interaction and to reduced breakpoint ringing in the processing.

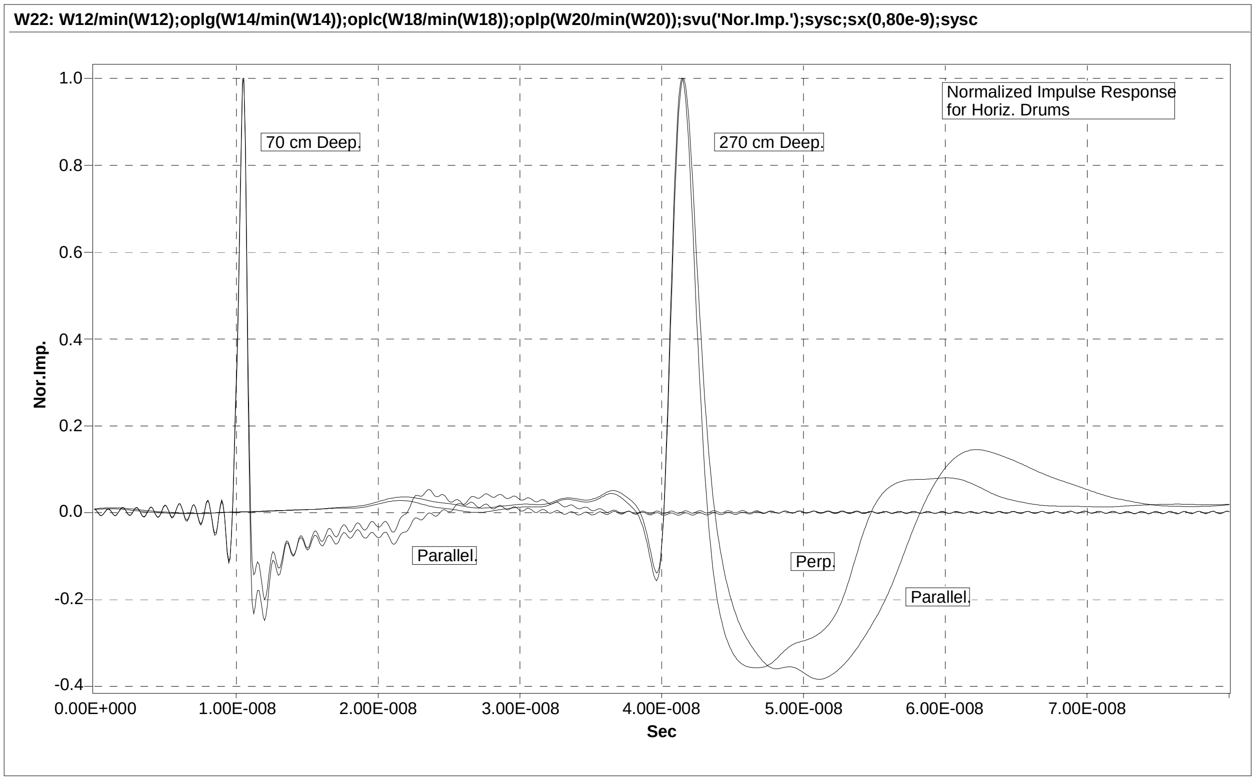

Fig. 10- *Peak-normalized impulse response of horizontal drum (both polarizations) at depths of 70 cm, and 2.7 m.*

Simulations of High-Power GPR System

Once the complete FFT form of $S(f)$, the backscatter buried-drum transfer function, was computed for each of the Duke drum configurations, this transfer function could then be used for simulations of a proposed high-power GPR system. That is, let $E_t(t)$ be the transmitted or radiated E-field wave from a transmitter. If it is at height *h* above the ground, then the wave impinging on the ground is

$$E_i(t) = \frac{E_t(t)}{h}.$$

Then this is taken as the incident wave for the numerical modeling work that was done by Duke, and the result is the wave that scattered off the buried drum and emerges from the ground, $E_{r2}(t)$, with spectrum given by

$$E_{r2}(f) = S(f)\, E_i(f) = S(f)\, \frac{E_t(f)}{h}.$$

And if the GPR system receive antenna is at the same height *h*, then the wave incident on the receive antenna is

$$E_{rx2}(f) = \frac{E_{r2}(f)}{h} = S(f)\, \frac{E_t(f)}{h^2}.$$

Note that the units are straightforward – the electric field is in V/m and distances are in m. The only clarification to this is that the radiated field from the transmitter, $E_t(t)$, is range normalized to 1 m (i.e., in units of V).

The other primary wave to be received by the GPR system is the initial ground reflection or surface bounce, $E_{r1}(t)$; this is easily computed as described in the Theory section. The resulting wave picked up by the receive antenna is given by

$$E_{rx1}(f) = \frac{E_{r1}(f)}{h} = \Gamma_1(f)\, \frac{E_t(f)}{h^2}.$$

Thus, with an estimate of the transmitted field, $E_t(t)$, the complete propagation problem can now be simulated.

Fig. 11 shows two waveforms for such a purpose. The noisy one is based on experimental pulser work at Sandia, and the smooth one is a fitted theoretical pulse. The output voltage pulse from design #3 of the frozen wave generator (built by Gary Denison) was measured on 4/19/99. The noisy waveform in Fig. 11 is the time derivative of this pulser output pulse, and represents what we expect the radiated field pulse to be from a flared TEM horn transmit antenna. This expectation is based on extensive measurements which were made last Fall by Gary with the Ross pulser and 'Spruce Goose' TEM horn antenna. That work indicated that the radiated field is approximately a time derivative of the pulse driving the antenna, for this VHF frequency band of interest. The noisy waveform in Fig. 11 had its peak amplitude scaled to an actual high-power shot with the Ross/Spruce Goose transmitter, for a realistic estimate of the radiated field from the frozen wave generator and a similar TEM horn antenna. Note that the vertical scaling is in V; this is $E_t(t)$ based on experimental work.

The other waveform in Fig. 11 is a theoretical Rayleigh pulse for cleaner simulations. The order and peak frequency were adjusted for best fit in both the time domain and the frequency domain. Here, the order was 6 and the peak frequency was 240 MHz. Fig. 12 shows the corresponding spectrum of each of these waveforms. It should be noted that this frequency range was decided upon for the design of the frozen wave generator, based on the vertical drum simulations described herein. These plots were generated in the 'ws0_FWG_Pulse' worksheet of Dadisp.

The spectrum of the Rayleigh pulse in Fig. 12 is then used as $E_i(f)$ in these simulations, and the resulting buried-drum wave, $E_{r2}(t)$, and the surface-bounce wave, $E_{r1}(t)$, were computed for all seven Duke drum configurations. It should be noted that the $1/h^2$ term in the equations for $E_{rx1}(t)$ and $E_{rx2}(t)$ has not been included here. Neither has the effect of the receive

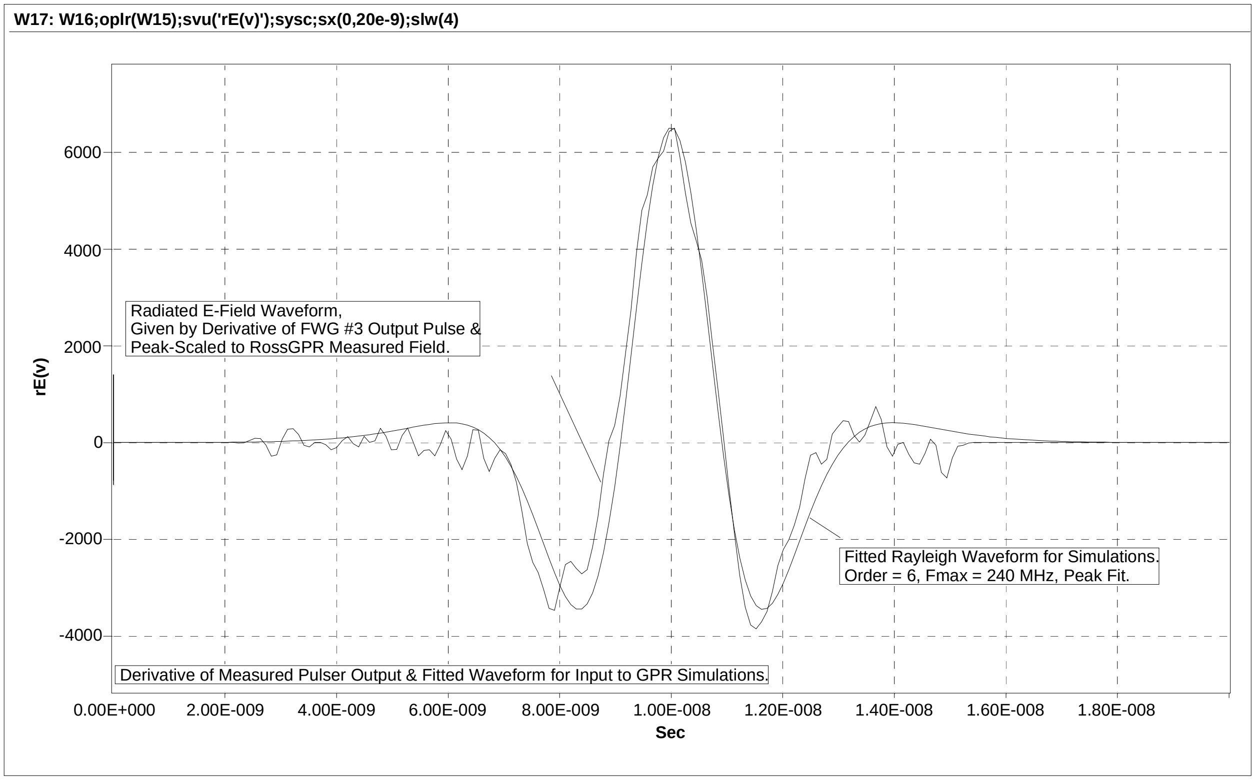

Fig. 11- *Estimated radiated E-field waveform from a high-power GPR transmitter and the fitted theoretical waveform for use in simulations.*

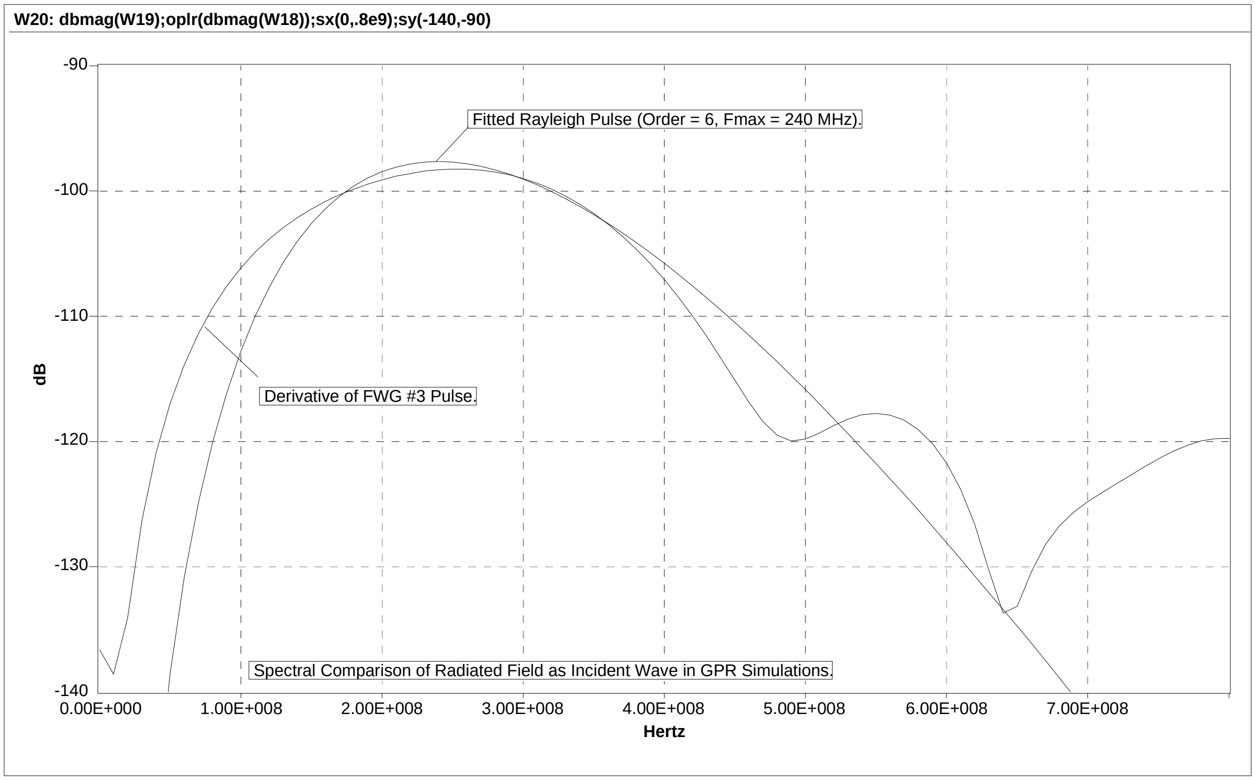

Fig. 12- *Frequency content of radiated high-power E-field and the theoretical waveform used in simulations.*

antenna response – this means that the actual received voltage in the GPR receiver cannot be computed without more information.

In worksheet ‘ws6_ShallowSims’, the Rayleigh pulse above is used to compute the backscatter from the horizontal drum (both polarizations) at 70-cm depth and the vertical drum at 1-m depth. In these simulations the peak amplitude of the incident pulse is unity (+1 V/m) for easy scaling of the results. Fig. 13 contains the resulting time-domain waveforms for the buried-drum pulse from the three shallow drum configurations. Note first that the reflected wave is negative – this indicates that the buried drum is metallic (yielding a negative scattering characteristic). Note too that the primary portion of the waveforms are very similar – showing that for the particular incident spectrum used in the simulations, there is little difference in the backscatter transfer function. This primary portion (the first and large triplet) is the specular reflection from the top portion of the drum; there is a secondary portion which is much smaller in amplitude and is composed of not only the remainder of the scattered drum ringdown but also a double bounce between the drum and the earth surface. The peak amplitude, E_{pk}, is given in the plot alongside each waveform. For easy comparison, the equivalent decibel loss is computed as

$$20\log_{10}\left|E_{pk}\right| \text{ dB.}$$

Fig. 14 shows the total reflected wave, $E_r(t) = E_{r1}(t) + E_{r2}(t)$, which includes not only the buried-drum bounce of Fig. 13 but also the initial surface bounce. Note that the surface bounce pulse has a negative peak amplitude of 0.4061, indicating that for the dielectric constant used here, the wave reflected off the ground is flipped over (just like the drum reflection), and at 40.6% amplitude of the incident wave impinging on the ground. This is –7.8 dB relative to the incident wave – much larger than the reflection off the buried drum, and it shows how important the receiver processing scheme will be. That is, successful detection of buried drums depends upon being able to find the low-level buried-drum pulse some time after the large-level ground bounce. Fig. 14 also shows the roundtrip time delay between the surface bounce and the buried-drum bounce. Some form of time-gating the receiver may be used – and may be required for finding the deeper drums (where $E_{r2}(t)$ is so much smaller than $E_{r1}(t)$). There is the separate issue of time-gating to prevent the radiated wave from the transmitter coupling into the receiver and overloading it (even before the wave hits the ground below the antennas).

Then in the ‘ws7_DeepSims’ worksheet of Dadisp, the deeply buried drum configurations were simulated. Fig. 15 shows the buried-drum response, $E_{r2}(t)$, for the vertical drum 2 m and 3 m deep and the horizontal drum (both polarizations) 2.7 m deep. Note that the peak time is consistent with their depth. Note as well the dropping amplitude with increasing depth. Here too, the waveforms are very similar, with little distinction between vertical and horizontal drum orientation. This implies that with this limited-bandwidth GPR system excitation, we can’t easily tell the difference between the two orientations. If the GPR system were designed with much more bandwidth, then the scattered wave would contain more spectral information and correspondingly more time-domain detail. Unfortunately, this higher-frequency content would be severely attenuated for the depths examined here, with little improvement in overall transient target information.

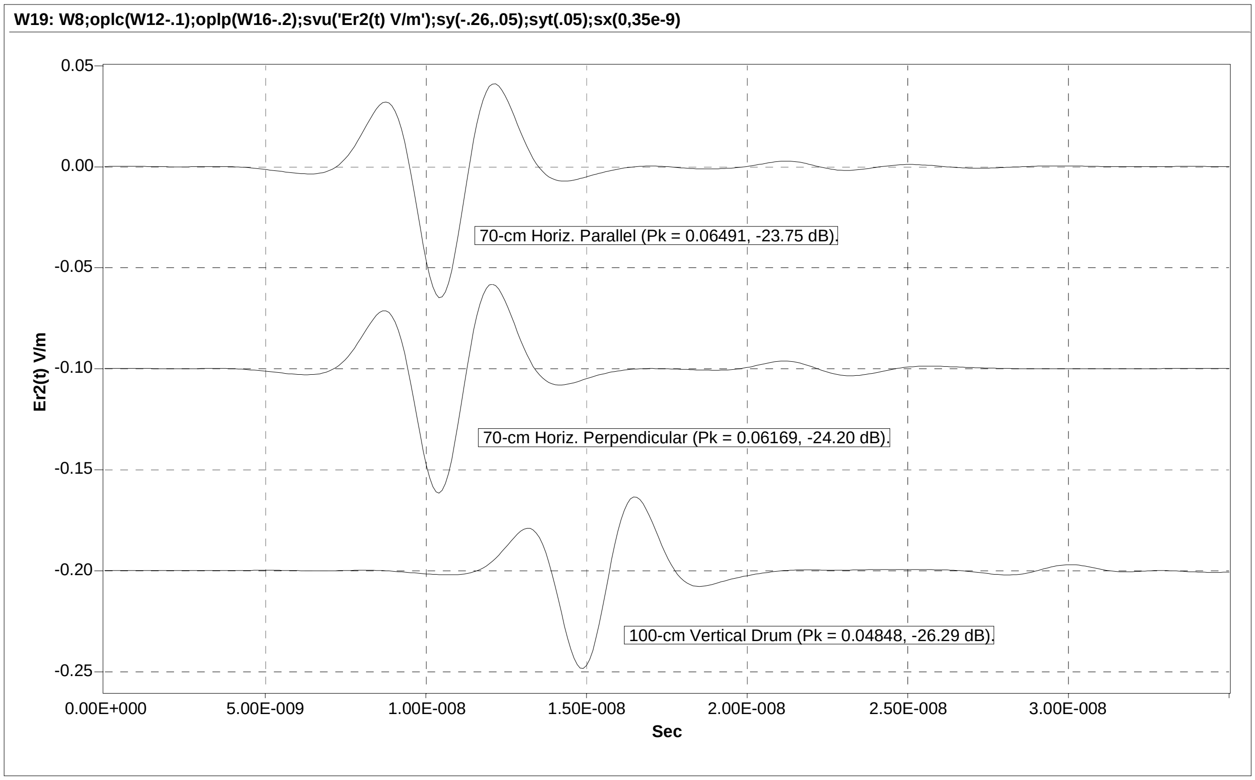

Fig. 13- *Simulated Er2(t) buried-drum pulse emerging from earth for high-power GPR transmitter (relative to 1-V/m incident peak amplitude) and shallow drum configurations.*

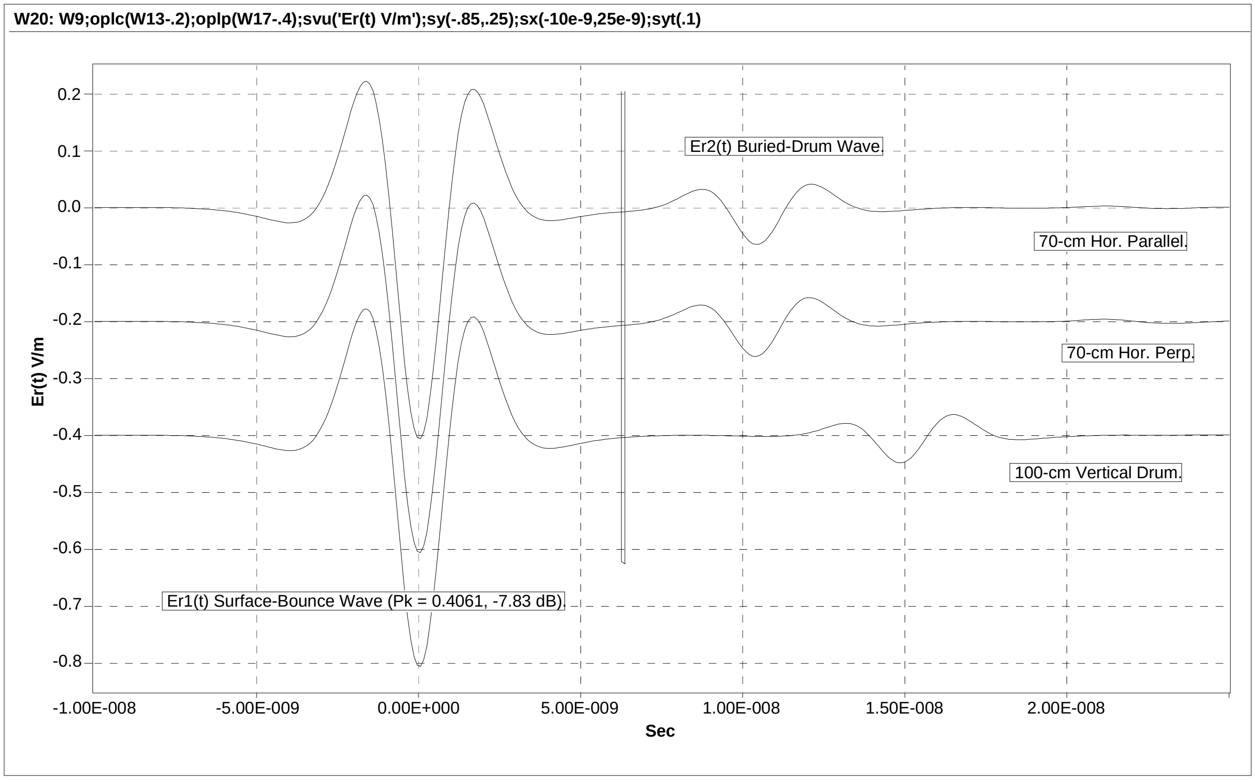

Fig. 14- *Simulated Er(t) wave emerging from earth for high-power GPR transmitter and shallow drum configurations. Includes both ground bounce and buried-drum bounce.*

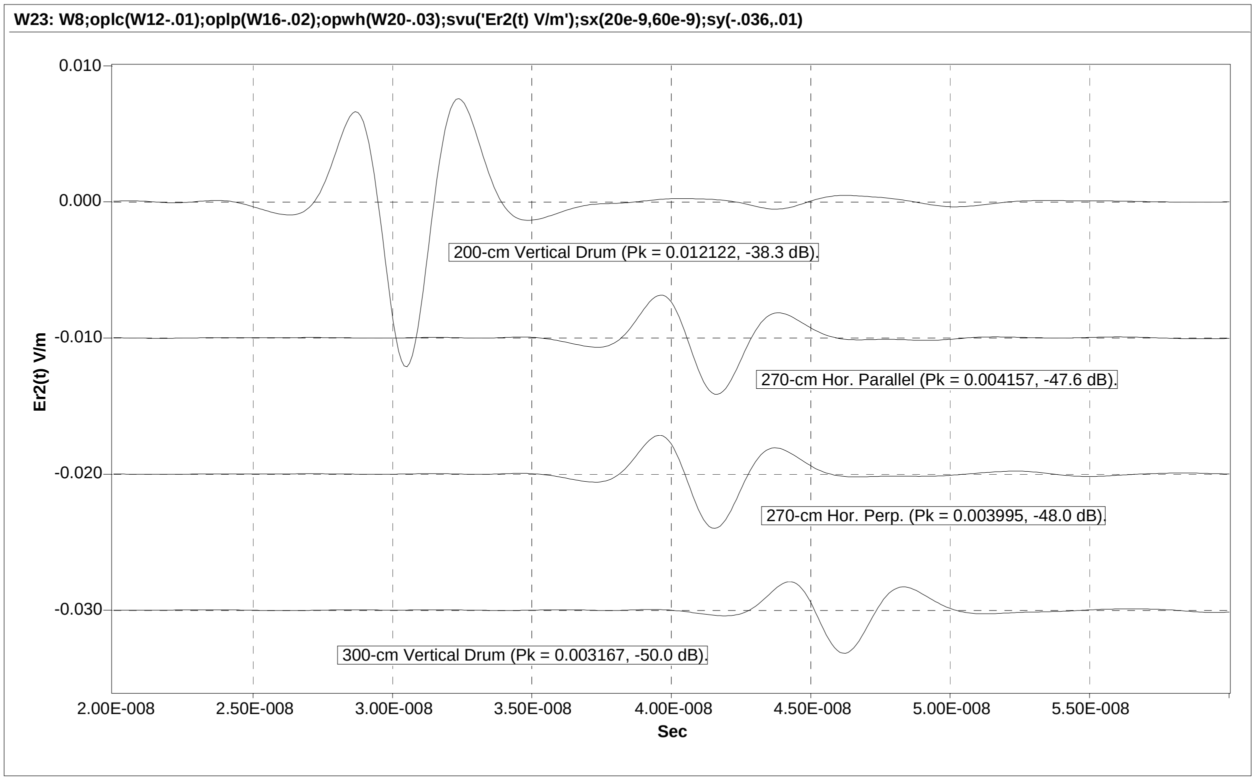

Fig. 15- *Simulated Er2(t) buried-drum wave emerging from earth for high-power GPR transmitter and deep drum configurations.*

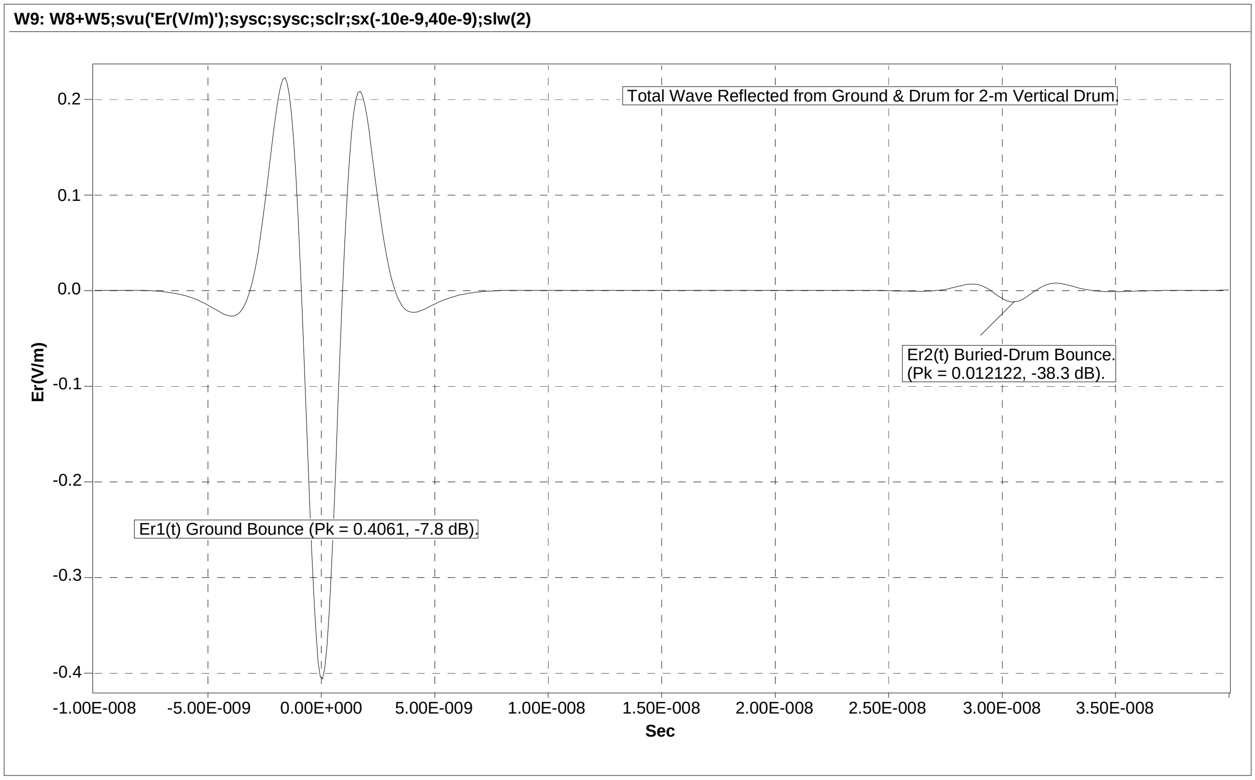

Fig. 16- *Simulated Er(t) wave emerging from earth for high-power GPR transmitter and 2-m deep vertical drum. Includes both ground bounce and buried-drum bounce.*

Fig. 16 gives the overall received/reflected wave, $E_r(t)$, for just the 2-m deep vertical drum case. This can be compared with the waveforms shown in Fig. 14 for the shallow cases. In Fig. 16, the ground bounce, $E_{r1}(t)$, is the same as for all the configurations. The buried-drum response, $E_{r2}(t)$, is much lower due to the increased depth. The overall wave for the other deep cases are not given here because $E_{r2}(t)$ is too small to see on the same scale as the ground bounce.

An alternative way of plotting the time-domain waveform with more dynamic range is to plot the decibel version:

$$E_r(t)_{dB} = 20\log_{10}\left|E_r(t)\right|.$$

This was done in Fig. 17; it has the decibel time-domain waveforms for the deeply buried drum cases. In all four cases, the surface bounce is the same (they overlay exactly, at time zero). But on this decibel scale, the relatively small buried-drum pulses are easily seen.

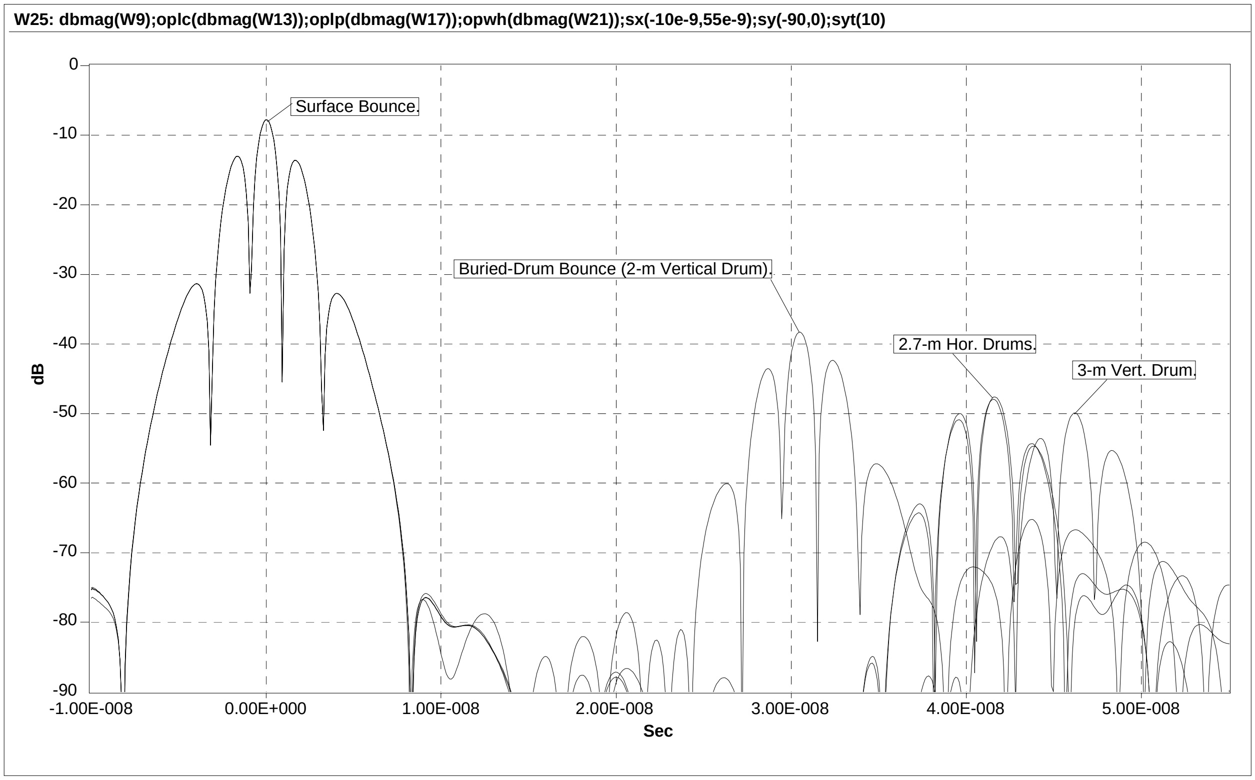

Fig. 17- *Decibel plots of simulated Er(t) wave emerging from earth for high-power GPR transmitter and deep drum configurations. Includes both ground bounce and buried-drum bounce.*

As a summary of the simulations, the roundtrip time, negative peak amplitude (relative to +1 V/m incident), and peak amplitude in dB are tabulated below. And the apparent dielectric constant, computed with

$$\varepsilon_r = \left(\frac{cT}{2d}\right)^2,$$

for the three vertical drums, is 4.99, 5.24, and 5.35 for depths of 1, 2, and 3 m. Remember that this is for the given incident field spectrum – it would be different for higher frequencies because of the assumed Hipp soil type. Now, if the soil in the actual high-power GPR experiments has a moisture content and dielectric constant different than this, the formulas included herein may be used to corroborate roundtrip times and dielectric constant with known drum depth.

Drum Configuration **and Depth**	**Roundtrip** Time (ns)	Peak Amplitude (%)	**Peak** Amplitude (dB)
70-cm Horizontal Parallel	10.41	6.49	-23.8
70-cm Horizontal Perpendicular	10.41	6.17	-24.2
100-cm Vertical	14.90	4.85	-26.3
200-cm Vertical	30.53	1.21	-38.3
270-cm Horizontal Parallel	41.66	0.416	-47.6
270-cm Horizontal Perpendicular	41.56	0.400	-48.0
300-cm Vertical	46.25	0.317	-50.0

In terms of using these simulations to quantify the viability of the proposed GPR system, the most important consideration is the system sensivitity (or system loss). For a given high-power transmitter and time-gated receiver, what are the smallest signals which can be measured with an acceptable signal-to-noise ratio? The parameter of interest in these simulations is the magnitude of the buried-drum transfer function, $|S(f)|$, for the general problem. But in particular, with the incident pulse which we used in the simulations, the corresponding parameter is either the magnitude of the buried-drum pulse spectrum, $|E_{r2}(f)|_{dB}$, or in time, the peak amplitude of $E_{r2}(t)$. This single-valued time-domain parameter is valid to use for system calculations only because the pulse spectra (and transient pulse shapes) are so similar for the different drum configurations.

For the worst case simulated, the highest attenuation is the scattering from the 3-m deep vertical drum, with 50 dB of pulse attenuation. This should be straightforward to measure in a practical GPR system. If the envisioned worst-case target scenario yielded a system loss of over 80 dB, then the resulting system would be more difficult to design and implement. A system loss of 100 dB is a typical limit for all kinds of radar systems (either direct time-domain or swept frequency). So if the soil encountered has comparable loss to the soil type used here, then the actual GPR system should be straightforward to design and implement. But if the soil is much wetter, with much higher attenuation, then a drum at 3-m depth may not be detectable. One of the practical system issues will be the exact way that receiver time-gating is implemented, and the resulting isolation it provides between the radiated high-power wave and the receiver output.

We have also determined that for the type of specific incident waveform used in these simulations, the waveshape of the pulse scattered off the buried drum will be relatively insensitive to drum orientation – and thus easier to detect with the GPR system. The primary concern will be the detection of the specular bounce pulse off of the buried drum, at some time after the ground bounce pulse.

DISTRIBUTION

EXTERNAL DISTRIBUTION

5 ITT Industries
AES Division
Attn: J. F. Aurand
6400 Uptown Blvd, NE
Suite 300E
Albuquerque, NM 87110

1 Duke University
Dept. of Electrical and Computer Engineering
Attn: L. Carin
Box 90291
Durham, NC 27708-0921

INTERNAL DISTRIBUTION

1	MS 0839	M. S. Derzon, 16000
1	MS 1153	D. Brown, 15333
1	MS 1153	M. T. Buttram, 15301
5	MS 1153	G. J. Denison, 15333
1	MS 1153	W. Helgeson, 15333
5	MS 1153	G. M. Loubriel, 15333
1	MS 1153	M. W. O’Malley, 15333
1	MS 1153	L. F. Rinehart, 15333
1	MS 1153	F. J Zutavern, 15333
1	MS 1165	W. Guyton, 15300
1	MS 0188	LDRD Office, 4001
1	MS 0612	Review and Approval Desk, 9612 For DOE/OSTI
2	MS 0899	Technical Library, 9616
1	MS 9018	Central Technical Files, 8945-1